

**STUDY OF TURBULENT MIXING IN A POST DETONATION
ENVIRONMENT USING SCHLIEREN AND IMAGING
SPECTROSCOPY**

by

JAMES SCOTT ANDERSON

Submitted in Partial Fulfillment
of the Requirements for the Degree of
Master of Science in Mechanical Engineering
with Specialty in Explosives Engineering

New Mexico Institute of Mining and Technology
Socorro, New Mexico
May, 2017

ABSTRACT

Experiments were performed to study turbulent mixing of iodine seeded detonation events. The schlieren imaging technique and imaging spectroscopy techniques offer two unique methods to understand a flow environment. The schlieren imaging technique provides a visualization of flow features through refractive index changes, but does not distinguish between changes in chemical composition. Imaging spectroscopy records absorption spectra to identify changes in the chemical composition in the field of view. By correlating these two techniques the fluid motion and relative concentration of iodine was tracked during a range of experiments. Tests were conducted in a 100 x 100 mm square cross section shock tunnel. Initial tests consisted of a shock wave from a 209-shotgun primer interacting with an iodine seeded helium plume. Test data includes shock velocity, plume size and relative iodine concentration. The shock wave caused a direct spatial shift of the iodine plume with turbulent mixing beginning shortly after. Testing with an RP-2 detonator, 50 mg of high explosive with a charge of 500 mg of iodine pentoxide and aluminum ($Al-I_2O_5$) thermite showed iodine mixing through out the field of view. Focusing schlieren was explored as a method to expand this testing toward field scale.

Keywords: Schlieren Imaging ; Imaging Spectroscopy; Turbulent mixing; Shock tunnel

ACKNOWLEDGMENTS

I would like to thank my adviser Dr. Michael J. Hargather for guidance and support over the last four years. The several classes including, fluids, thermodynamics, aerospace propulsion, digital image processing, fluid and thermal systems have all been wonderful opportunities to be inspired to learn high-speed fluids. The opportunities to teach through the living learning communities to preform undergraduate research and preform graduate research has been wonderful. Every different role as a New Mexico Tech Shock and Gas Dynamics Laboratory (SGDL) member has been a great learning experience.

Many faculty and staff members of New Mexico Tech (NMT) and Energetic Materials Research and Testing Center(EMRTC) were instrumental in the success of this research. Brad and Tim from Ordnance for continued support of this research from test development to testing. EMRTC staff for support of this testing, test plan creation, safety support and everything required for explosive testing. Doreen, the Mechanical Engineering secretary, for all the help during my undergrad and graduate degrees. Ryan, the Mechanical Engineering Machinist for assistance creating parts, machining complicated parts and guidance on best practices. Dr. Simpson and the NMT CLASS department for guidance writing the thesis with boot camp and other classes.

Fellow Shock and Gas Dynamics lab-mates alumni and current members are a continued source of inspiration and guidance. Joshua Smith for the foundational research and guidance developing these optical methods. Each SGDL member has been a source of different inspiration and guidance. Austin, Josh, Stewart, Jeff, Kyle, Rudy, Cara: Thank you all.

My family, parents, Barbara and Brian, brother, Sam for the constant support and assistance through out the higher education experience. My grandparents for all the support over the years. Thank you for the continued guidance love and support.

This thesis was typeset with \LaTeX ¹ by the author.

¹The \LaTeX document preparation system was developed by Leslie Lamport as a special version of Donald Knuth's \TeX program for computer typesetting. \TeX is a trademark of the American Mathematical Society. The \LaTeX macro package for the New Mexico Institute of Mining and Technology thesis format was written by John W. Shipman.

CONTENTS

LIST OF TABLES	vi
LIST OF FIGURES	vii
1. INTRODUCTION	1
1.1 Research Motivation	1
1.2 Literature Review	1
1.2.1 Richtmyer-Meshkov Instability	1
1.2.2 Schlieren Imaging Technique	2
1.2.3 Imaging Absorption Spectroscopy	2
1.2.4 Large Scale Refractive Optical Techniques	4
1.2.5 Foundational Research at New Mexico Tech	5
1.3 Objectives of the Present Research	5
2. DIAGNOSTIC METHODS	6
2.1 Tunnel for High-speed Optical Research	6
2.2 Piezoelectric Pressure Transducers.	9
2.3 Imaging Spectroscopy	9
2.3.1 Spectrometer System Design	10
2.3.2 Spectrometer Calibration	11
2.3.3 Iodine Calibration	12
2.4 Schlieren Imaging Technique	15
2.4.1 Data Analysis	15
2.5 Streak Imaging	16
3. COMMON PATH SCHLIEREN IMAGING TECHNIQUE AND ABSORPTION IMAGING SPECTROSCOPY	20
3.1 Optical System Design	20
3.1.1 Light Source Characterization	23
3.1.2 System Noise	24
3.2 Correlation of the Schlieren Imaging Technique and Absorption Imaging Spectroscopy	24

4. IODINE PLUME VALIDATION EXPERIMENTS	27
4.1 Test Methods	27
4.2 Helium Gas Plume	27
4.3 Helium-iodine gas plume	31
4.4 Data Analysis	37
5. SHOCK WAVE INTERACTION WITH IODINE PLUME EXPERIMENTS	38
5.1 209 Shotgun Primer Test Series	38
5.1.1 Background Signal Processing	39
5.1.2 Data analysis	39
5.2 Iodine Gas Shock Wave Interaction	46
5.2.1 First Injection to Shock Wave Interaction	46
5.2.2 Full Field Analysis	46
5.3 Streak Image Analysis	48
5.4 Conclusions	56
6. IODINE IDENTIFICATION WITH $AL-I_2O_5$ PRODUCT GASES IN TURBULENT POST BLAST FLOWS	58
6.1 Test Methods	58
6.2 Shock Velocity	58
6.3 RP-2 Detonator with no thermite	59
6.4 RP-2 Detonator 500 mg of thermite	60
6.4.1 Full Field Analysis	60
6.4.2 Streak Image Analysis	64
6.5 Conclusions	71
7. LARGE SCALE OPTICAL METHODS	72
7.1 System Quantification Targets	72
7.2 Traditional Lens Schlieren	73
7.3 Traditional Focusing Schlieren	73
7.4 Lens and grid Schlieren updates	75
7.4.1 Construction of Source and Cutoff Grids	75
7.4.2 LED illumination	78
7.5 Modified focusing System	78
7.6 Plenoptic Camera	81
7.7 Large Field Schlieren System	84

7.7.1	Traditional System Theory	84
7.7.2	System updated Design	84
7.7.3	System Results	87
7.8	Conclusions	87
8.	CONCLUSIONS AND FUTURE RESEARCH RECOMMENDATIONS	89
8.1	Conclusions	89
8.2	Future Research	90
8.2.1	Short Term	90
8.2.2	Long term	91
A.	OPTICAL SYSTEM DRAWINGS	92
	REFERENCES	109

LIST OF TABLES

4.1	Experimental Conditions	37
6.1	Shock velocity measurements	59
7.1	System design specifications	86
7.2	System Parameters	86

LIST OF FIGURES

1.1	Iodine absorption profile.	4
2.1	The Tunnel for High-speed Optical Research (THOR).	7
2.2	THOR technical drawing.	7
2.3	Powder containment block.	8
2.4	Internal features of THOR.	8
2.5	Typical piezoelectric pressure trace from a two gram $Al-I_2O_5$ charge initiated with a RP-2 Detonator test	9
2.6	Imaging absorption spectrometer system schematic.	11
2.7	Bench-top calibration system setup.	11
2.8	Spectrometer calibration	12
2.9	Results from iodine cell calibration.	14
2.10	Schlieren imaging technique optical system schematic	15
2.11	Schlieren image examples.	16
2.12	Schlieren calibration	17
2.13	Shock wave velocity measurement example	18
2.14	Streak image example.	19
3.1	Completed test setup	21
3.2	Diagnostic setup schematic	21
3.3	Transmitting optics	22
3.4	Receiving optics	23
3.5	Spectroscopy efficiencies	24
3.6	Average arc lamp flicker over time.	25
3.7	Correlation process for schlieren imaging technique and imaging spectroscopy.	26
4.1	Setup for gas plume measurements	28
4.2	Helium gas plume response shown with two wavelength regions	29
4.3	Helium gas plume response shown with three spatial regions	30

4.4	Start of helium-iodine gas plume in the test chamber shown with two wavelength regions.	32
4.5	Start of helium-iodine gas plume in the test chamber shown with three spatial regions.	32
4.6	Helium-iodine gas plume in the test chamber shown with two wavelength regions.	33
4.7	Helium-iodine gas plume in the test chamber shown with three spatial regions.	33
4.8	Reduced iodine gas concentration in the plume in the test chamber shown with two wavelength regions.	34
4.9	Reduced iodine gas concentration in the plume shown with three spatial regions.	34
4.10	Relative concentration of iodine gas in the test chamber at 24.3 ms .	35
4.11	Relative concentration of iodine gas in the test chamber at 33.3 ms	35
4.12	Relative concentration of iodine gas in the test chamber at 33.3ms .	36
4.13	Higher concentration of iodine gas at 20 ms	36
5.1	209 primer localized refracted spectrometer signal	40
5.2	RP-2 detonator localized refracted spectrometer signal	41
5.3	Baseline shift of the spectral response with regards to spatial.	42
5.4	Localized refracted effects.	43
5.5	Refractive spectral noise	45
5.6	Relative concentration streak image for test 3	47
5.7	Shock wave and plume interaction frame 1	49
5.8	Shock wave and plume interaction frame 2	50
5.9	Shock wave and plume interaction frame 3	51
5.10	Shock wave and plume interaction frame 4	52
5.11	Shock wave and plume interaction frame 5	53
5.12	Shock wave and plume interaction frame 6	54
5.13	Streak images for test one	55
5.14	Relative concentration streak image for test 2	56
6.1	$Al-I_2O_5$ thermite powder used for testing.	59
6.2	Top) Schlieren imaging technique streak image. Middle) Spectral background signal. Bottom) Spectral background signal after the baseline shift.	61

6.3	Wave diagram detailing the theoretical shock wave interactions in the shock tunnel	62
6.4	Shock wave in test two	63
6.5	Start of iodine gas in test one	63
6.6	Test chamber filled with iodine.	64
6.7	Streak images of the relative concentration of iodine during test two	66
6.8	Streak images of the relative concentration of iodine during test three	67
6.9	Streak images of the relative concentration of iodine during test four	68
6.10	Vertical row from both schlieren imaging technique and absorption imaging spectroscopy streak images plotted at two distances from test two.	69
6.11	Vertical row from both schlieren imaging technique and absorption imaging spectroscopy streak images plotted at two distances from test three.	70
7.1	Depth of Focus targets	73
7.2	Traditional lens schlieren system with 80 mm field of view with a depth of focus greater than 80 mm.	74
7.3	Traditional inline focusing schlieren system.	74
7.4	Grid Measurements.	77
7.5	A) Test region from transmitting optics, B) Receiving optics, C) Test region from receiving optics, D) Source grid and light panel	79
7.6	A) Crossed helium jets separated by 20 mm axially, B) A single helium jet, C) Staircase target with bubble and candle, D) Glass ruler with bubble and candle	80
7.7	Plenoptic focusing schlieren results	82
7.8	A) Nikon focused around -40 mm, C) Nikon focused around +5 mm, D) Nikon focused around +40 mm	83
7.9	Traditional large field focusing schlieren system	84
7.10	Modified large field focusing schlieren system	85
7.11	Panoramic view of the NMIMT large scale focusing system	86
7.12	Single helium jet moved from -150 mm behind the focal plane to 150 mm in front of the focal plane.	87
7.13	A) Crossed helium jets separated by 50 mm on the optical axis, B) Crossed helium jets separated by 300 mm on the optical axis	88

This thesis is accepted on behalf of the faculty of the Institute by the following committee:

Michael J. Hargather

Advisor

Nikolai Kalugin

Tie Wei

I release this document to the New Mexico Institute of Mining and Technology.

JAMES SCOTT ANDERSON

Date

CHAPTER 1

INTRODUCTION

1.1 Research Motivation

The explosive post detonation environment is rich with turbulent mixing, fluid flows, and debris interactions. This environment has not been fully characterized and there are several applications that require better understanding of shock induced turbulent mixing. The primary application examined in this text is the dispersal of chemicals within the post detonation environment. This research will develop methods to understand these high speed dynamic events including the mixing that happens after the detonation event. The schlieren imaging technique and imaging absorption spectroscopy will share a common optical axis to investigate locations where iodine, contained within the explosive, is observed mixing with the ambient air. The limitations of these optical techniques will be explored. A method to expand this testing to larger open air testing is desired. Focusing schlieren offers a high fidelity method of visualizing fluid motion through changes in refractive index changes. The primary application of this research requires a large scale event characterization.

1.2 Literature Review

1.2.1 Richtmyer-Meshkov Instability

Turbulent mixing involving shock wave interactions is classically defined as a Richtmyer-Meshkov Instability (RMI) problem. RMI occurs at the interface between two fluids when a shock wave interacts with the interface [1]. This instability is present in rectangular cross section shock tubes [2, 3]. The instability has been analyzed by many [4, 5, 6, 7]. The instability arises when a shock wave crosses the boundary between two fluids. Following the initial shock wave a perturbed shock wave is transmitted into the second fluid. A reflected shock can be sent back into the original fluid. This interaction creates opposing vorticity at the boundaries. This leads to unstable vorticity with in the fluids[1]. For the present work the shock wave produced by the detonation event propagates directly into the air, inducing some potential vorticity at the explosive edge, but the problem

is not the same as the classical RMI problem with a fluid-fluid interface. The present work therefore is not compared to the previous RMI literature.

1.2.2 Schlieren Imaging Technique

A method is required to measure the fluid properties within the post blast environment. The schlieren imaging technique provides insight into the fluid flow of the event by measurements of the first spatial derivative of the refractive index[8]. The refractive index of a fluid will change with density, temperature, pressure, and chemical species [9]. From these data sets the location and relative change of the fluid media properties in the test section will be observed.

The schlieren imaging technique has been used for fluid studies since the 1600s [8]. In more recent times the schlieren method has been used to observe shock-waves and fluid phenomena in explosive events [10, 11]. Several review papers of this technique have been written, Houas in 1999 [12], Settles in 2001 [8], Kleine in 2010 [9], and Settles and Hargather in 2017 [13].

An explosively driven shock tube, referred to as the “Tunnel for High-speed Optical Research” (THOR) was utilized for this research. A shock tube is a simple duct with open or closed ends, composed of two sections, the driver and the driven section [14]. Shock tubes have been driven with rattle or shotgun primers [15], high pressure gases [2], or explosive charges[16]. In the early years of shock tube research, the schlieren imaging technique was recognized as a important diagnostic tool, however the technology was limited and images were of poor quality[14]. The 1999 paper by Houas covers modern optical techniques in relation to shock tunnel work [12]. The recent advances in digital high speed photography and computing power allowed high quality images to be captured. Unwanted background distortions can be removed through post processing the images [17].

1.2.3 Imaging Absorption Spectroscopy

A second method is required to determine changes in chemical composition of the test section. Spectroscopy determines chemical species through observations of light intensity. A spectrometer measures the transmitted or absorbed amount of light for each wavelength. Spectrometers consist of a series of mirrors and a diffraction grating which splits light into wavelength components. Traditionally, spectrometers have been complicated optical devices that require long scanning times [18]. The grating element is rotated through the desired wave lengths and the sensor captures one point of data [19]. In 1985, Goetz introduced

the concept of “imaging spectroscopy,” a technique that uses a charge-coupled devices (CCD) sensor as a spectrometer detector[18]. This technique removed the need to “scan” through the wavelengths because the CCD detector is a multiple line instrument. The need for a compact fast scanning satellite based spectrometer for remote ground sensing drove the development of this technique. Since this invention, many steps have been taken to enhance the performance and use of imaging spectroscopy[20]. Imaging spectrometers create a data cube of: wavelength, spatial location, and intensity. Depending on the capability of the detector a time history can be captured.

Several methods to decrease the integration time have been pursued. For high-speed spectroscopy, pulsed laser spectroscopy has been used, resulting in a single spectrum with a short integration time [21, 22]. Limited temporal resolution is possible with this method. Glumac used a single trace repeated over several tests to resolve an explosive event temporally [22]. Koch used a high speed InGaAs array to capture emission spectra at 46,992 spectra/s with an integration time of 13.9 ms [23].

The first complementary metal-oxide semiconductor (CMOS) high-speed cameras were invented by Vision Research in the late 1990s. Traditionally the charge-coupled devices (CCD) have been used as detectors for spectrometers [21]. Many high-speed and streak cameras are limited to the region from 200 to 800 nm [23]. The CMOS sensor found in the Photron camera line has no known spectroscopy uses found in the open literature. The CMOS sensor allows for faster integration time and more versatility of pixel resolution at the cost of a limited wavelength band.

Iodine is a well studied chemical with theoretical and experimental absorption profiles. Tellinghuisen in 1973 worked to clarify and correct several inconsistency between the theoretical and experimental profiles [24]. Figure 1.1 is the I_2 absorption spectrum corresponding to the $B \leftarrow X$ electronic transition as described Tellinghuisen in 1973. The absorption profile was furthered enhanced by Saiz-Lopez in 2004 with modern techniques [25]. Figure 1.1 is the I_2 absorption spectrum described Saiz-Lopez in 2004. This experiment was performed on pure I_2 at standard temperature [24]. Tellinghuisen also describes several other experiments done varying pressure, path length, temperature and gas mixtures of iodine species. The effects of these changes is not well known and several theories exist [24].

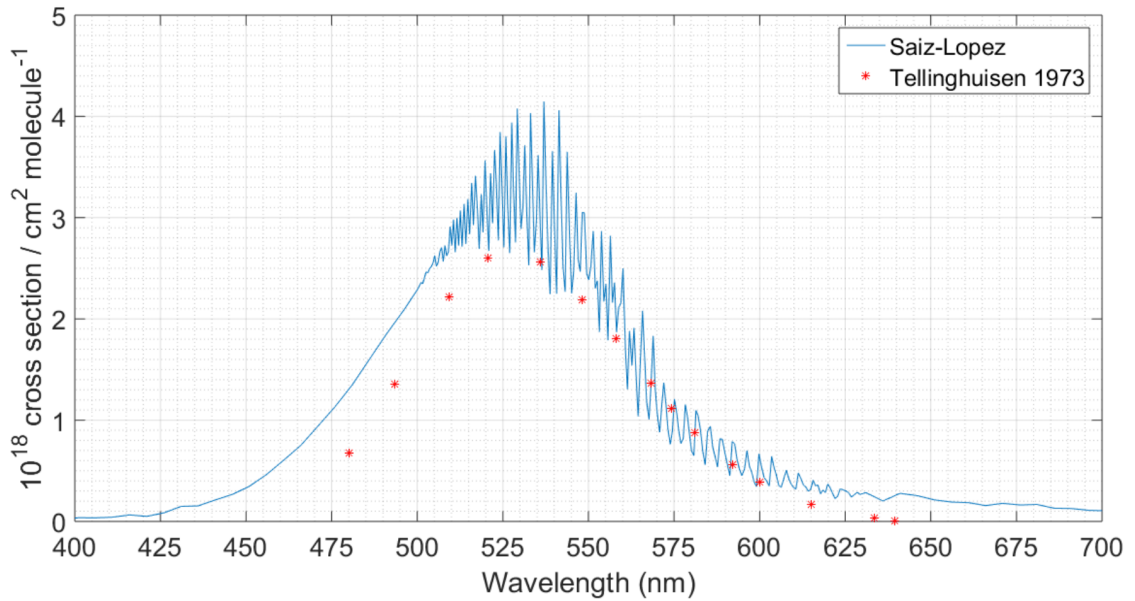


Figure 1.1: Digital reproduction of Tellinghuisen’s 1973 iodine profile [24]. Digital reproduction of Saiz-Lopez’s 2004 iodine profile [25]. Profiles have been normalized for comparison.

1.2.4 Large Scale Refractive Optical Techniques

Currently, there are three refractive imaging techniques used to image large-scale events: focusing schlieren, shadowgraph, and background oriented schlieren (BOS). BOS is the least complicated for field setup requiring only a camera and a random pattern background, which can be a natural background [26]. Imaging small disturbances, however, is difficult with BOS. Shadowgraph is a moderately complicated setup with a retro-reflective screen, light source and a camera, but provides no quantitative information about the density fields[27]. This technique is best suited for flows that create strong refractive index shifts resulting in clear changes in screen illumination[8]. Focusing schlieren has the finest resolution and quantitative information of the three large scale methods.

Focusing schlieren uses a series of grids to produce multiple schlieren imaging effects [27]. Traditionally the source grid is a commercial product, silk screened, or taped off by hand. These options are costly, difficult to employ, and limit the flexibility of the system. Floryan proposed a method of using transparency sheets and a standard printer[28]. VanDercreek used vinyl decal stickers to create larger rulings, these rulings then had to be applied to the backing accurately[29]. However these methods are limited on size and availability of materials. Laser cutting has become more accessible and offers a method for creating grids at a low cost and production time these properties will be explored here. In addition, plenoptic studies of the test region will be demonstrated.

1.2.5 Foundational Research at New Mexico Tech

Smith began work in August 2015 to characterize turbulent mixing in the post blast environment [30]. The foundational research had four main areas, explosive material selection, explosive material safety, test fixture development, and system proof testing. Small scale sensitivity testing performed by Smith indicated that the thermite mixture of $Al-I_2O_5$ is moderately impact sensitive, highly resistant to spark initiation and sensitive to friction. Smith applied both the schlieren imaging technique and imaging absorption spectroscopy to this research. Smith used a Horiba microHR spectrometer with Horiba grating 52019, a grating with 1800 grooves per mm resulting in a 44 nanometer wavelength range [30]. This grating limited the wavelength region to 40 nm, the iodine peak spans 150 nm and affirmative identification was not achieved. Smith's work provides a foundation of a test platform and method for measuring post detonation turbulent mixing.

1.3 Objectives of the Present Research

The current research will focus on the development and testing of common path absorption imaging spectroscopy with the schlieren imaging technique. The schlieren imaging technique offers a method to characterize the fluid flow; while absorption imaging spectroscopy provides data on the relative concentration and location of the iodine gas within the test chamber. The schlieren imaging technique and absorption imaging spectroscopy share similar optical components and a method to correlate these two techniques in both spatial and temporal dimensions will be demonstrated. Basic measurements of turbulent mixing will be explored using iodine as a trace gas. Focusing schlieren offers a method to transition this testing to an open air larger scale. A method to produce high quality low cost source grids with a laser cutter was explored. Limitations of laser cutting source and cutoff grids will be determined.

CHAPTER 2

DIAGNOSTIC METHODS

This research used several instrumentation and diagnostic methods to explore turbulent mixing in the post-blast environment. Tests were conducted in a shock tube test fixture. The schlieren imaging technique measured shock velocity, gas velocity, and basic turbulent mixing. Piezoelectric pressure transducers were verified shock velocity and measured explosive impulse. Absorption imaging spectroscopy measured the absorption spectra, and relative concentration of iodine in the test section.

2.1 Tunnel for High-speed Optical Research

Smith created the shock tunnel referred to as “The Tunnel for High-speed Optical Research” (THOR) from three sections, driver, optical diagnostic, and exit section [30]. Figure 2.1 is the completed tunnel split into the three sections. THOR has a constant 101.6 mm square cross section. The driver section was made from 19 mm thick 4140 steel plates. The detonation products flow from the driver section into the optical diagnostic section. This section was made from 12.7 mm thick 4140 steel and has four 7.94 mm thick optically clear acrylic windows. Each window has a viewing area of 50.8 by 177.8 mm. A pressure transducer is located upstream and downstream of the windows. The flow then enters the 2.44 m long exit section. Figure 2.2 is a length-wise cross-section technical drawing of THOR. All testing was completed using THOR and test apparatuses designed for use with THOR.

A breech block was created to hold the explosive charge and locate the primer gun in a repeatable manner. An exploded view of the block is shown in Figure 2.3. The Swagelok fitting (1) is threaded into the detonator plate (2). The detonator (3) is secured into the Swagelok fitting. The $Al-I_2O_5$ powder is poured into the swagelok fitting. The burst disk (4) is placed over the detonator plate. The completed assembly is secured into the positioning block (5) with four 1/4-20 bolts (6) and nuts (7). The holder is placed into the driver section of THOR and secured with four locating bolts (8). The placement of the breech block within THOR is shown in Figure 2.4. The burst face is considered to be the location of

the burst disk.

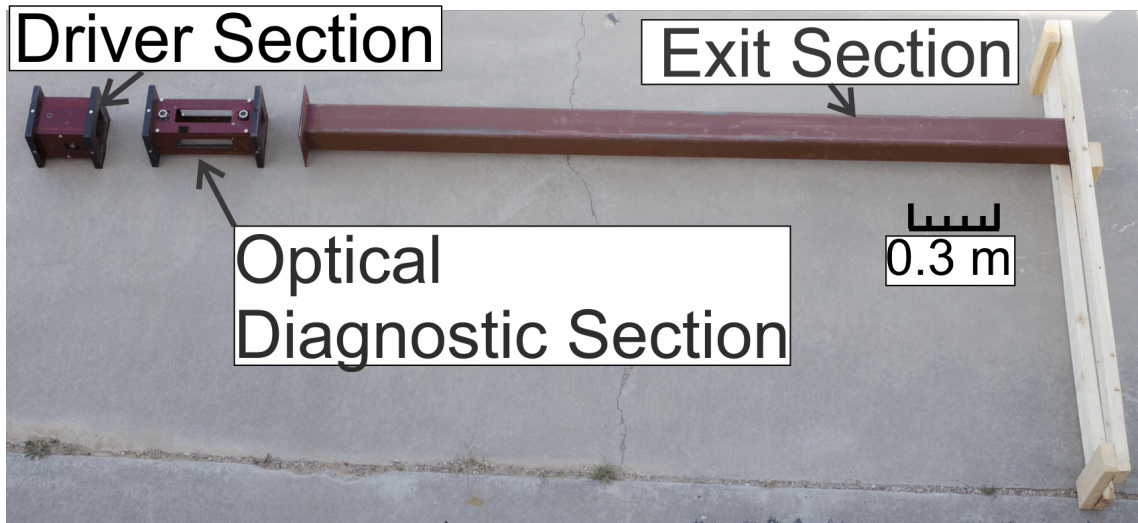


Figure 2.1: The Tunnel for High-speed Optical Research (THOR). The left side is the driver section in which the charge is placed. The middle of the image is the optical diagnostic section where flow measurements were taken. The flow vents to atmosphere through the exit section pictured on the far right.

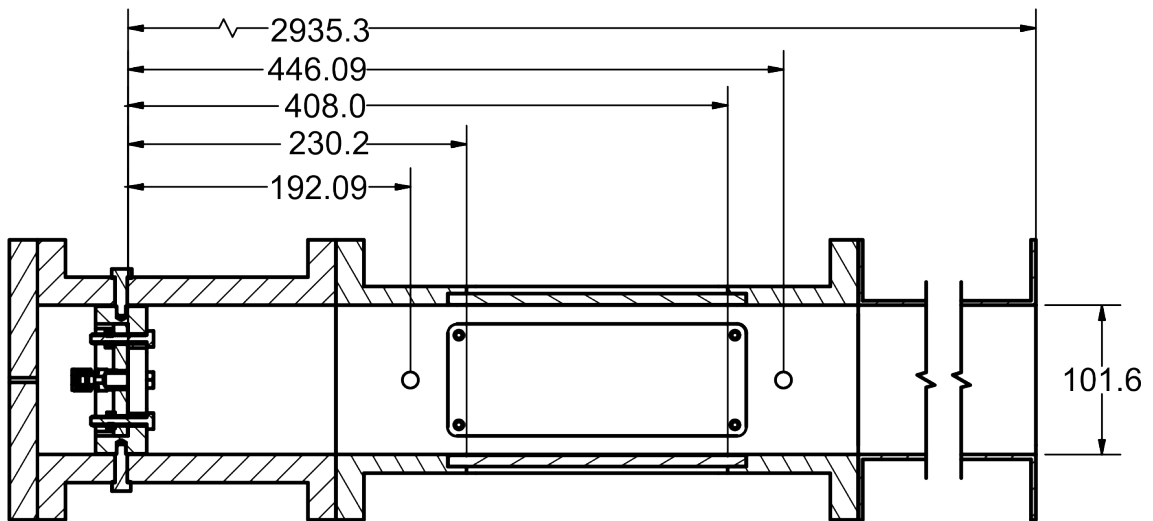


Figure 2.2: Technical drawing of THOR. Dimensions, in millimeters, pictured are the location of the pressure transducers from burst face. The detonator is located on the far left and flow exits on the far right.

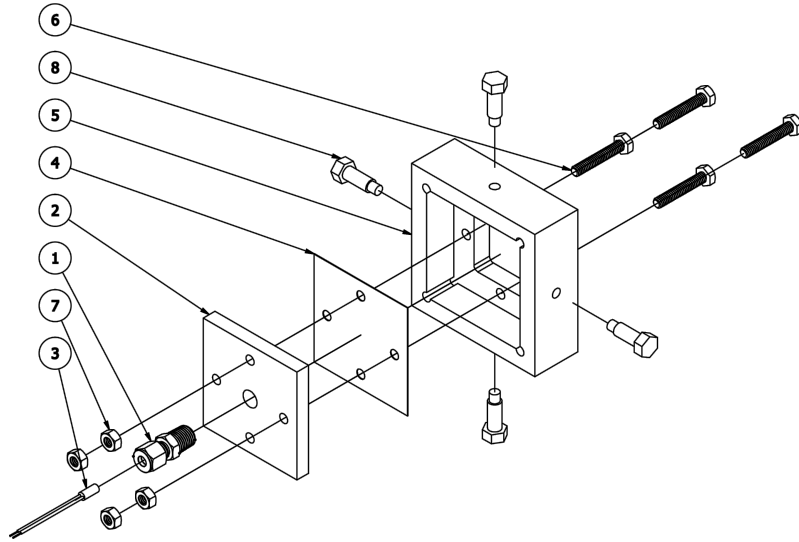


Figure 2.3: Exploded view of the breech block. 1) Swagelok fitting. 2) Detonator plate. 3) RP-2 Detonator. 4) Cellulose acetate burst disk. 5) Positioning block. 6-7) 1/4-20 Bolts and nuts. 8) Locating bolts.

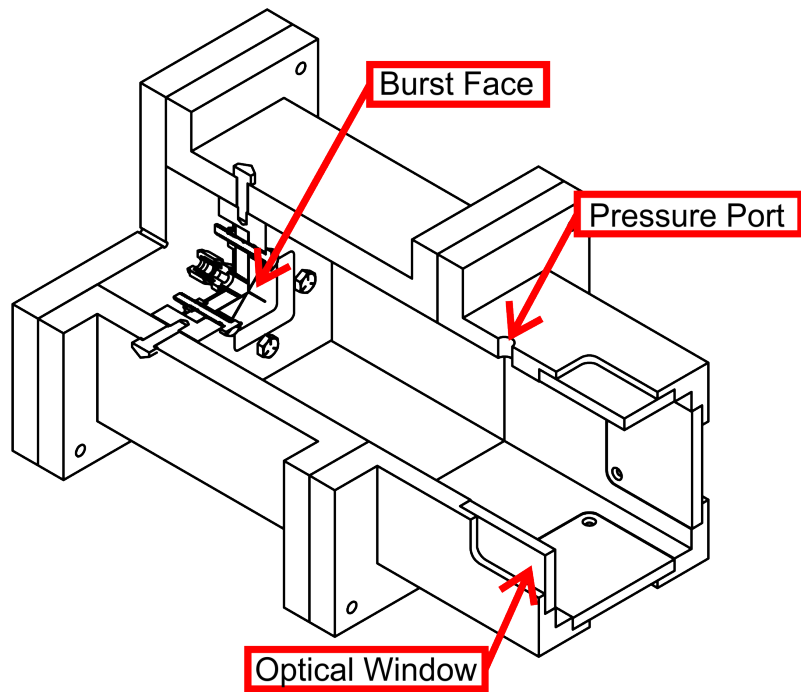


Figure 2.4: Pictured are the internal features of THOR. On the far left the breech block secured into the driver section. Middle of the image are the PCB pressure transducer ports. Right side of the image are the four optical windows.

2.2 Piezoelectric Pressure Transducers.

Piezoelectric pressure transducers provided a secondary method to measure shock velocity. The upstream pressure transducer was located 192 mm from the burst face. The second pressure transducer is located 254 mm from the upstream transducer. Figure 2.2 shows the location of these two ports. The transducers used were 6.9 MPa rated, $34.47 \text{ mV kPa}^{-1}$ piezoelectric pressure transducers from PCB Piezotronics (model 102B06). A PCB signal conditioner (model 482C15) performed the necessary signal conditioning. TBS1064 Digital Storage Oscilloscope from Tektronics recorded all pressure transducer data. Data was collected at a sample interval of $4 \mu\text{s}$ and 0.02 volts per division.

Pressure data was processed with a MATLAB code to determine time of arrival of the shock wave at each transducer. Figure 2.5 is a typical pressure trace from testing. The blue line is the upstream transducer, the red line is the downstream transducer. To calculate shock speed the physical separation of the transducers was divided by the time between shock arrival.

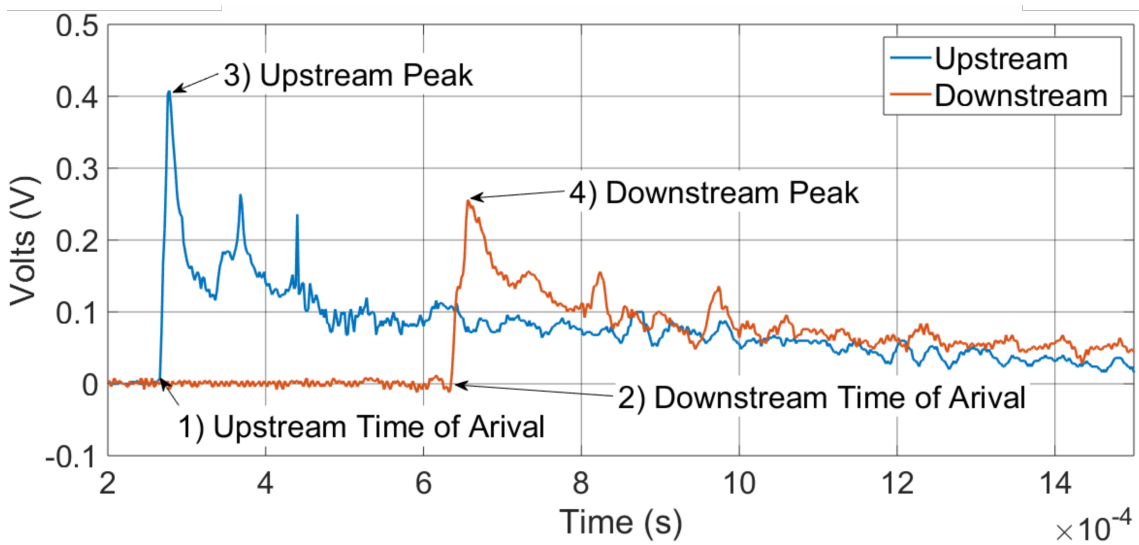


Figure 2.5: Typical piezoelectric pressure trace from a two gram $\text{Al-I}_2\text{O}_5$ charge initiated with a RP-2 Detonator test

2.3 Imaging Spectroscopy

The Beer-Lambert law defines absorption spectroscopy as shown in Equation 2.1 [21]. I is the light intensity before the absorbing material and I_0 is the intensity after the absorbing material. ϵ is the molecular absorption coefficient, c

is the sample concentration and d is the optical depth of sample. The maximum optical depth when testing in THOR is 101.6 mm, or the internal distance between the two windows. The exact optical depth and concentration of the sample is unknown during testing.

$$I = I_0 e^{-\epsilon cd} \quad (2.1)$$

For simplification the absorbency of the material was calculated. The absorbency A of the sample is defined by Equation 2.2:

$$A = \log \frac{I_0}{I} = \epsilon cd \quad (2.2)$$

To correct for spectral noise the absorbency is calculated from Equation 2.3. The spectrum from the room with the source light turned off is subtracted from both I and I_0 . Due to the fast exposure speeds used, 0.29 to 15 ms, the room noise is minimal.

$$A = \log \frac{Spectra_{Test} - Spectra_{room}}{Spectra_{ArcLamp} - Spectra_{room}} \quad (2.3)$$

2.3.1 Spectrometer System Design

For this testing absorption imaging spectroscopy was implemented, the setup is shown in Figure 2.6. A Xenon arc lamp was the light source for this testing. The light source was placed at the focal point of a simple lens. The light was collimated and then re-focused with a second lens. The region between the two lenses was the test area. The light was then focused with a small collimating lens, which matches the F number and input size of the spectrometer. This optical setup is the same optical setup that is required for the schlieren imaging technique. A Horiba microHr spectrometer equipped with grating 51019 was chosen for this testing. Grating 51019 has 300 grooves per mm, a blaze wavelength of 600 nm, and a blaze angle of $5^\circ 10'$.

The Horiba spectrometer was designed to image a vertical region, this research requires a horizontal region. The spectrometer is rotated 90° for the entrance slit to match the flow direction of THOR. A custom spectrometer mount was created to perform the needed rotation of the spectrometer. This spectrometer mount allowed for direct bolting to an optical bread board. The spectrometer was coupled to a Photron SA-X2 high speed camera. The Horiba microHr spectrometer is normally coupled to either a Horiba detector or a CCD camera with a C-mount attachment. The Photron SA-X2 camera has a physical profile larger than most CCD cameras. In order to couple this camera to the spectrometer, several custom mounts were manufactured. Six M4 socket headed cap screws were placed into the Photron SA-X2 side panel, the heads of these bolts served as guide pins for an acrylic mounting sled. The sled then was attached to the optical bread

board. Diagrams of these mounts can be found in Appendix A. The camera was mounted to the spectrometer with a C-mount adapter, the back plane between the Horiba spectrometer and Photron Sa-X2 camera was adjusted for sharp spectral lines.

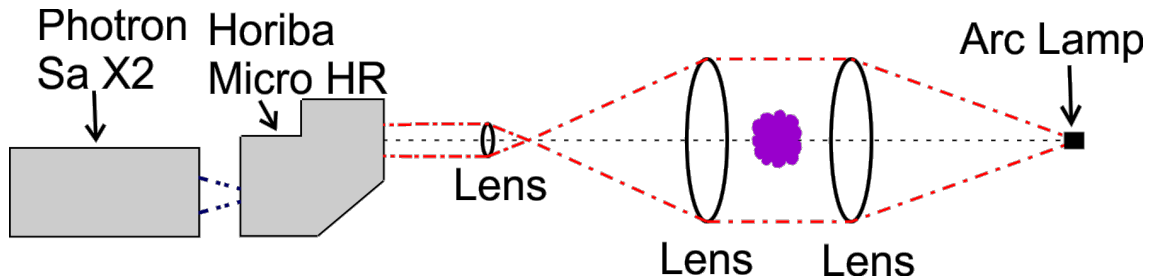


Figure 2.6: Imaging absorption spectrometer system schematic.

2.3.2 Spectrometer Calibration

A calibration system is shown in Figure 2.7. The white LED, shown on the far right, and a mercury/argon calibration source (not shown) (Ocean Optics Part HG-1) were the light sources. Two 50 mm diameter, 200 mm focal length lenses created the test section.

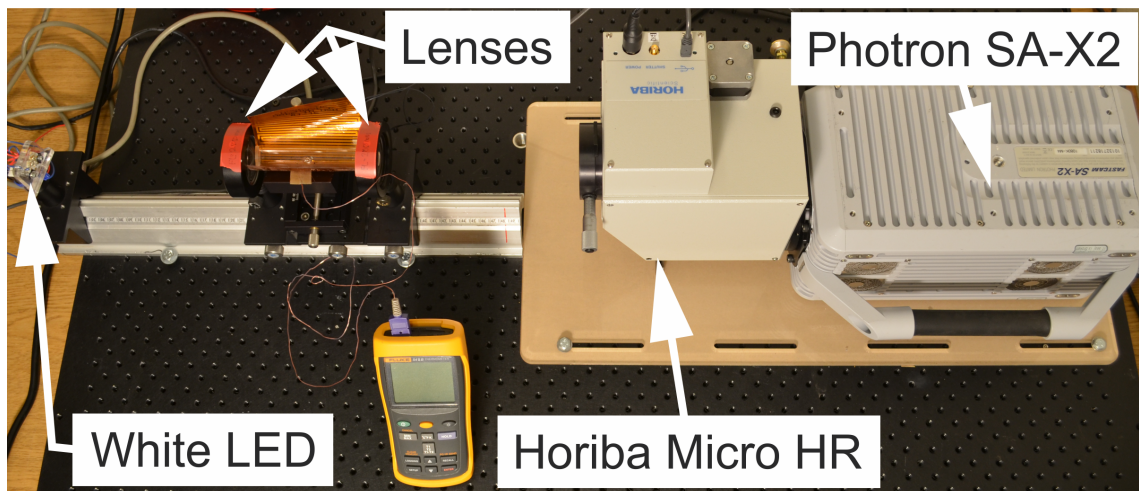


Figure 2.7: Bench-top calibration system setup.

The calibration source has a unique series of spectral peaks. Ocean optics provided theoretical wavelengths for this calibration source. These were confirmed with a single point spectrometer from Thorlabs, part number (CCS100). A

spectrum was recorded with both spectrometers. The single point spectrometer recorded wavelength and intensity. This data set was confirmed with the calibration light specifications. In Figure 2.8 the two data sets were compared. The single point spectrometer strongly agrees with the manufacturer's specifications.

The imaging spectrometer records an image with the horizontal axis denoting wavelength and the vertical axis denoting the spatial dimension. A threshold was applied to this image to convert to a binary image. The center position of each white region in Figure 2.8 is the location of a spectral peak.

A wavelength per pixel relationship was determined from the two data sets. The distance between peaks in pixels was measured from the imaging spectrometer data. The wavelength distance is then divided by the number of pixels between spectral peaks. The imaging spectral center point was also calculated from the data. This process was repeated after any change was made to the spectrometer setup. When testing with THOR, the calibration source was placed into the test section with the two side windows of THOR removed. The calibration source was moved until sufficient illumination was achieved. The entrance slit of the spectrometer was adjusted to capture sharp wavelength transitions.

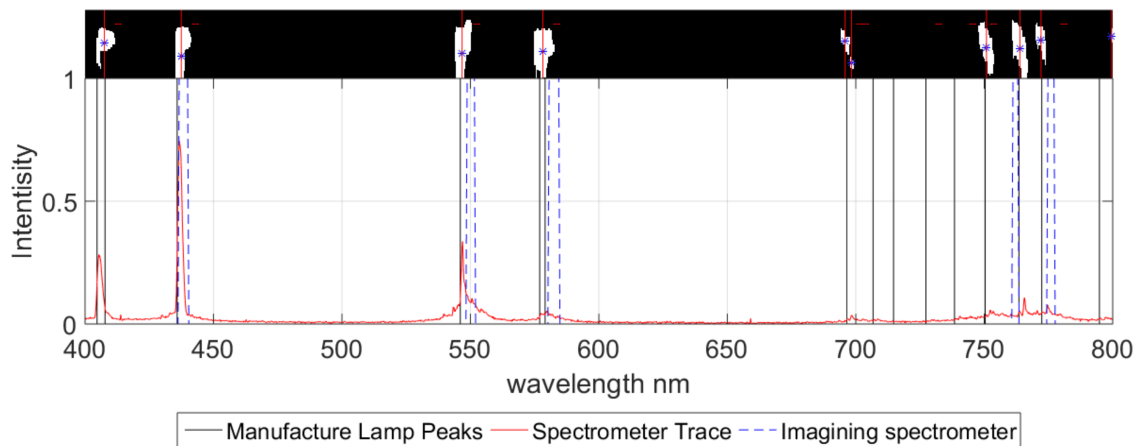


Figure 2.8: Spectrometer calibration process. Top image is the processed image showing each individual peak. The lower image is the plotted results. The manufacturer's peaks are plotted with straight black lines. The blue dotted line is the intensity plot from the imaging spectrometer. The red line is the spectral response recorded from the single point spectrometer.

2.3.3 Iodine Calibration

The spectrometer system performance was tested with an iodine reference cell from Thorlabs. The reference cell (part number GC19100-I) has a face diame-

ter of 19 mm and a length of 100 mm. The reference cell was heated with a Kapton heater till the surface temperature was 85 °C. The results of this are shown in Figure 2.9. In the top graph the imaging spectrometer's spectrum of the white LED was compared to the single point spectrometer's spectrum. The dual peak structure of the white LED's spectrum is shown in both spectrometers.

The middle graph of Figure 2.9 is the spectrum before and after the iodine reference cell is heated. The reference cell could not be removed without affecting the optical path of the light. It is assumed that only trace amounts of iodine gas were present in the cell before heating. The middle graph shows the shift in intensity from 450 to 650 nm. Of note is the non-ideal intensity from 460 to 490 nm. The intensity of light in this region approaches zero. The effect of this is shown in the bottom graph in Figure 2.9. The values from literature match closely with the experimental results with a few exceptions[24]. In the region from 460 to 490 nm the absorption values are clipped. The low intensity of the LED spectrum in this region is the cause.

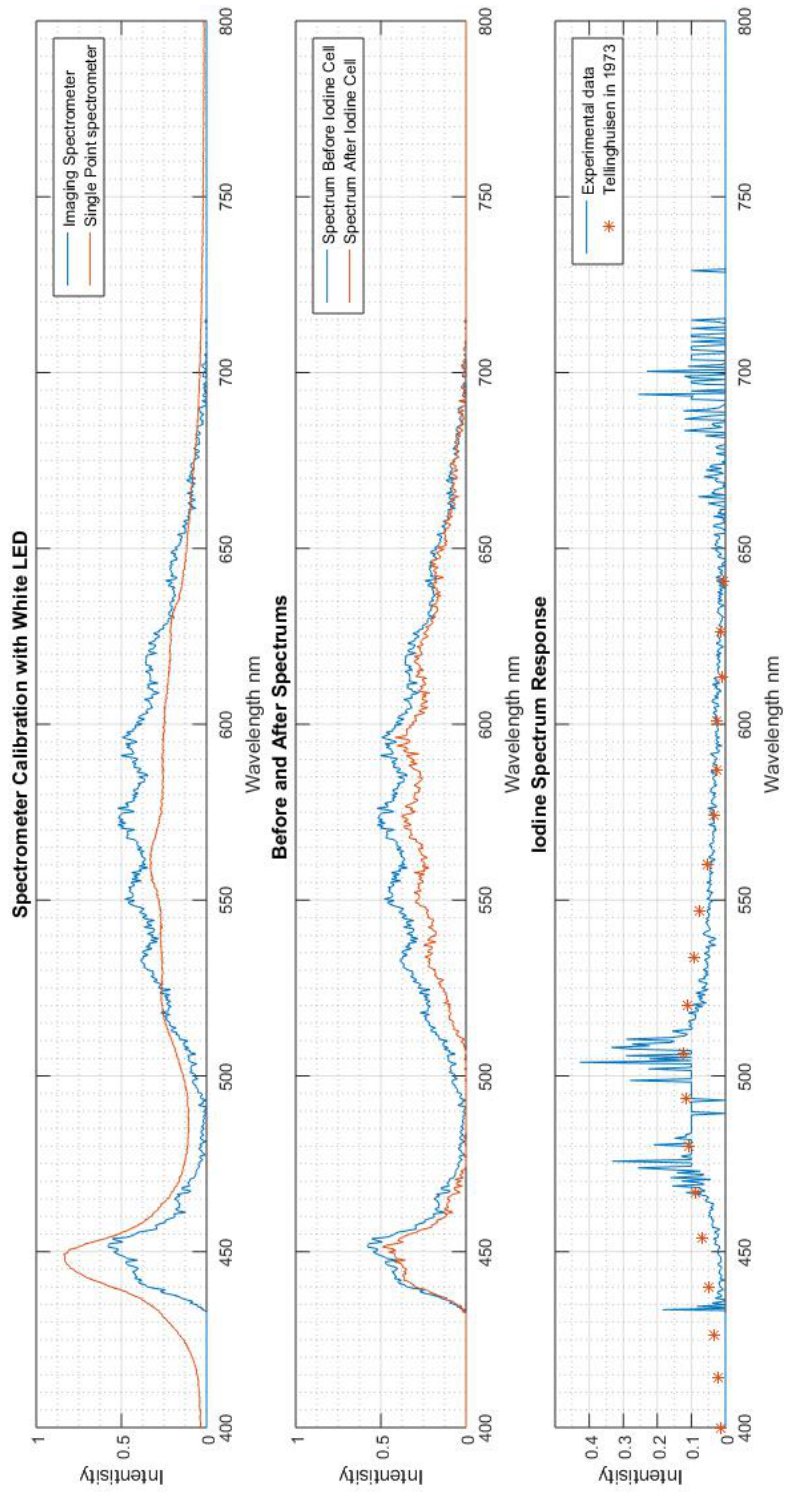


Figure 2.9: Top) White LED spectrum recorded with single point spectrometer and imaging spectrometer. Middle) Spectrum before and after heating the iodine reference cell. Bottom) Absorption spectrum compared to literature spectral response [24].

2.4 Schlieren Imaging Technique

A typical schlieren imaging system, as shown schematically in Figure 2.10, contains only a few optical elements including convex lenses, a light source, knife edge, and camera[8]. The point light source is located at the focal point of the lens, resulting in collimated light. A second matched lens was placed some distance from the first lens. The region between the two lenses is the test section. The second lens focuses the light back to a point. At the focal plane a knife edge was placed to block a portion of the light[8]. After the knife edge a high speed camera was placed. Two types of light sources were used, a 1000 W Xenon arc lamp by Newport Optics (model 66924) and a high brightness LED. Due to the intensity of the arc lamp a neutral density filter was used to reduce the brightness, this filter was placed before the knife edge.

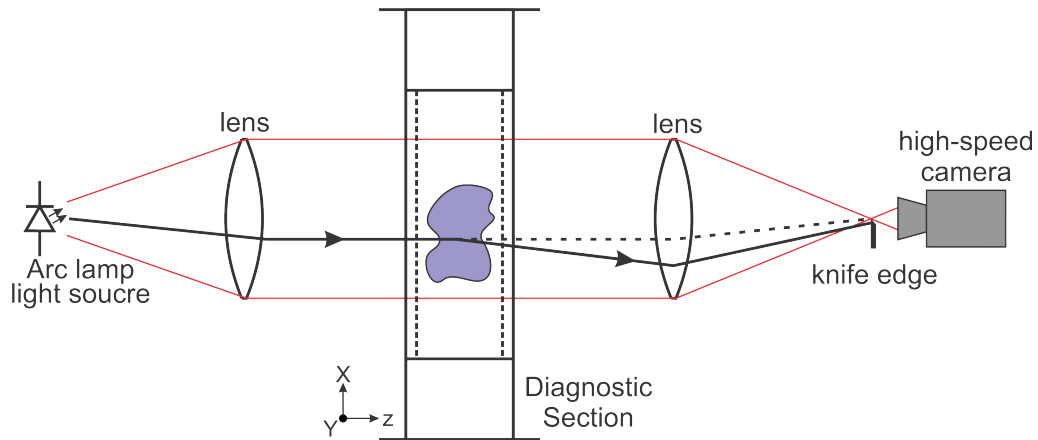


Figure 2.10: Schlieren imaging technique optical system schematic

2.4.1 Data Analysis

Examples of the schlieren imaging technique images are shown in Figure 2.11. The schlieren imaging technique images were post processed to remove background distortions and increase contrast. The 15 different optical surfaces collected dust and debris during testing and these imperfections were removed through post processing. Post processing was accomplished by subtracting a “no flow” tare image from the “flow” images. Contrast and brightness adjustments were made to make flow features distinguishable. The resulting image is shown in Figure 2.11 B, the images have fewer distortions and the contrast was improved. Of note are the supersonic particles to the right of the shock wave. In image A these particles are not visible, when processed a multitude of small 3 to 8 pixel particles are present in the field of view as seen in image B.

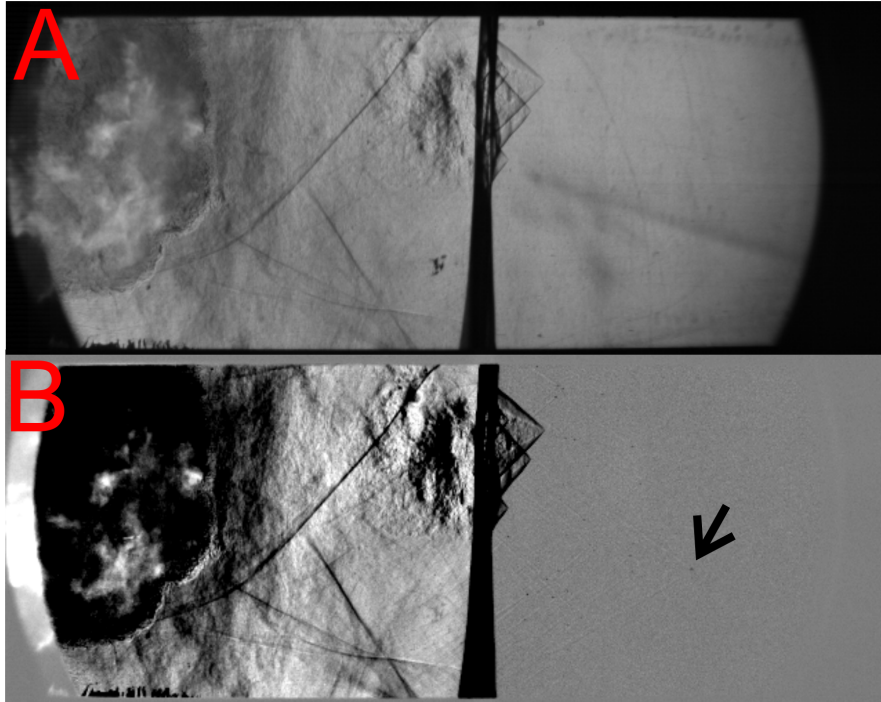


Figure 2.11: Two schlieren imaging technique image examples. In image (A) is the schlieren imaging technique examples have not been processed. Image (B) shows the post-processed image. Small fragments become are visible in image (B). One particle is highlighted by the drawn arrow.

To calibrate the schlieren imaging technique images an image is recorded of a known calibration target as shown in Figure 2.12 A. The physical dimensions of the calibration block are related to the number of pixels covered by the block. In the case shown, the 38.1 mm region of the calibration block covers 177 pixels in the schlieren imaging technique image. Thus the relationship is $0.216 \text{ mm pixel}^{-1}$.

The shock wave velocity was measured by determining the location of the leading edge of the shock wave in multiple schlieren imaging technique image frames. The distance traveled was computed and divided by the time between image frames to calculate the shock wave velocity. An example of this processing is shown in Figure 2.13.

2.5 Streak Imaging

During processing it was determined that streak images would be the best way to represent data temporally. Streak images are essentially space time dia-

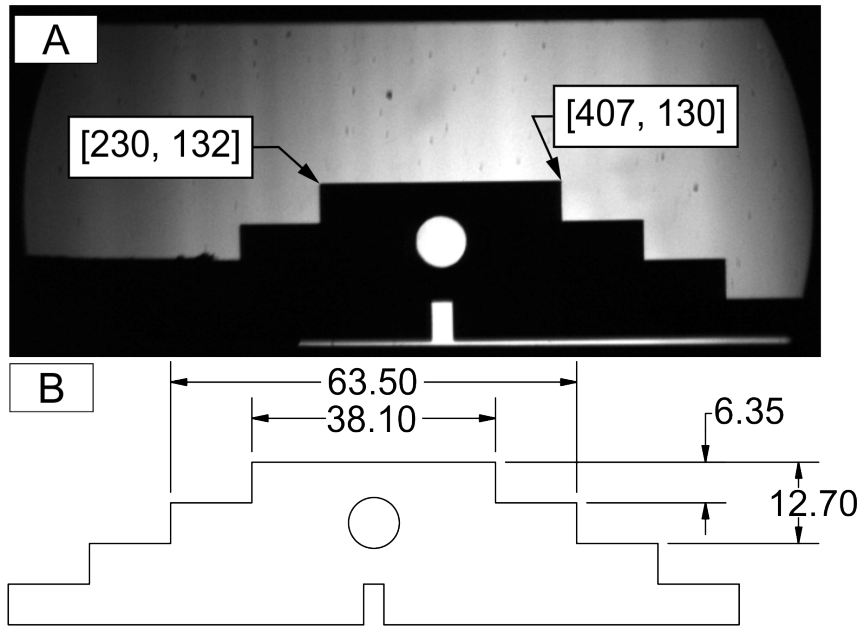


Figure 2.12: A) Calibration object in optical test section. The pixel locations for the two corners are labeled. B) Technical drawing of the calibration block using millimeter dimensions.

grams of the data[31]. This technique has been used for explosive research and allows for temporal analysis of the schlieren imaging technique images[32]. Examples of this processing are shown in Figure 2.14. A single line of pixels was extracted from each schlieren imaging technique image and then stacked into one master image[13]. Settles suggests creating these images through MATLAB with the output of an image file[13]. In image A of Figure 2.14 the 150th row of pixels is extracted from the schlieren imaging technique image. This single pixel row of the schlieren imaging technique analysis closely matches the narrow spatial band that the absorption imaging spectrometer averages the light intensity from. The same process was applied to the spectral data by extracting an average absorptivity over a given wavelength region. A second output of a three dimensional MATLAB "surface" plot provided easier manipulation of the data sets. These two types of streak images are presented in Figure 2.14. The middle image was generated as an image file, the bottom image was created using a surface plot of the streak data. The surface plot breaks the resolution limits and allows for resizing. In addition, the color of the surface streak image is easily change with a simple color map.

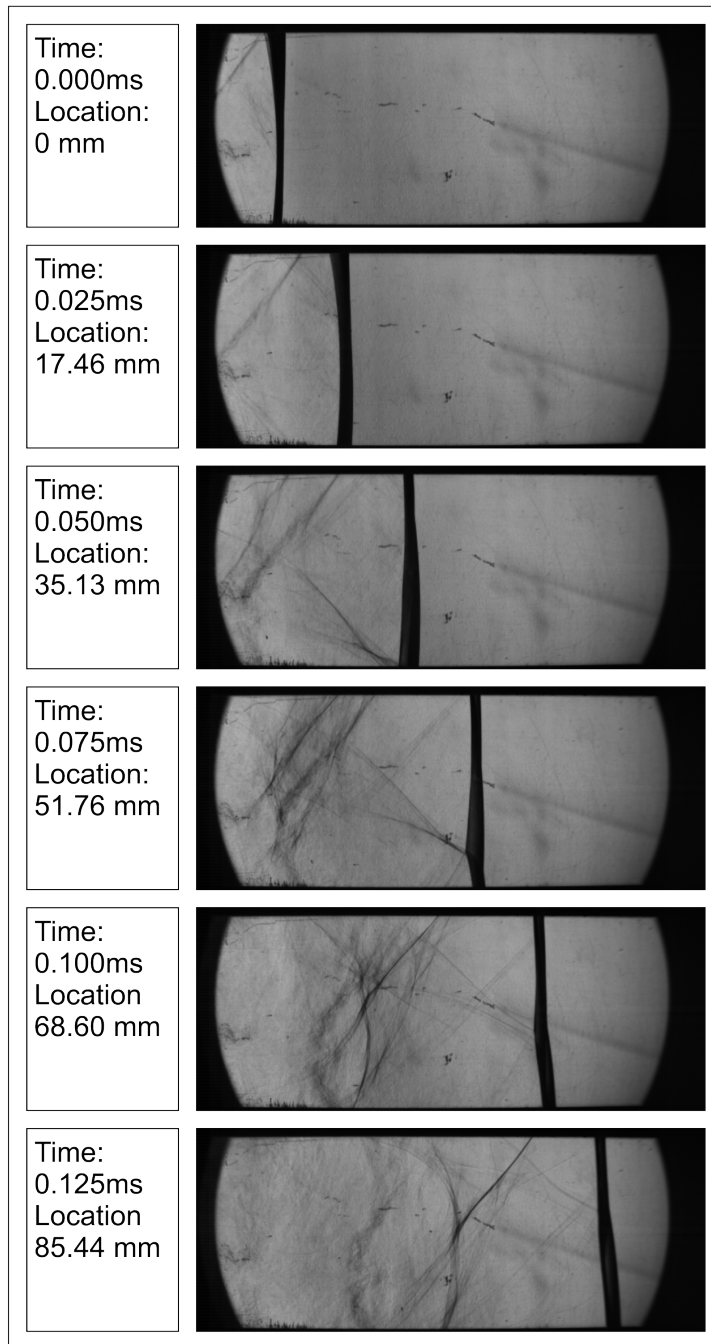


Figure 2.13: Six image frames from a two grams of $Al-I_2O_5$ thermite charge initiated with a RP-2 detonator showing the shock wave progression through the field of view. The distance from the initial shock wave location in frame one is calculated in millimeters. The image sequence was recorded at 40,000 fps.

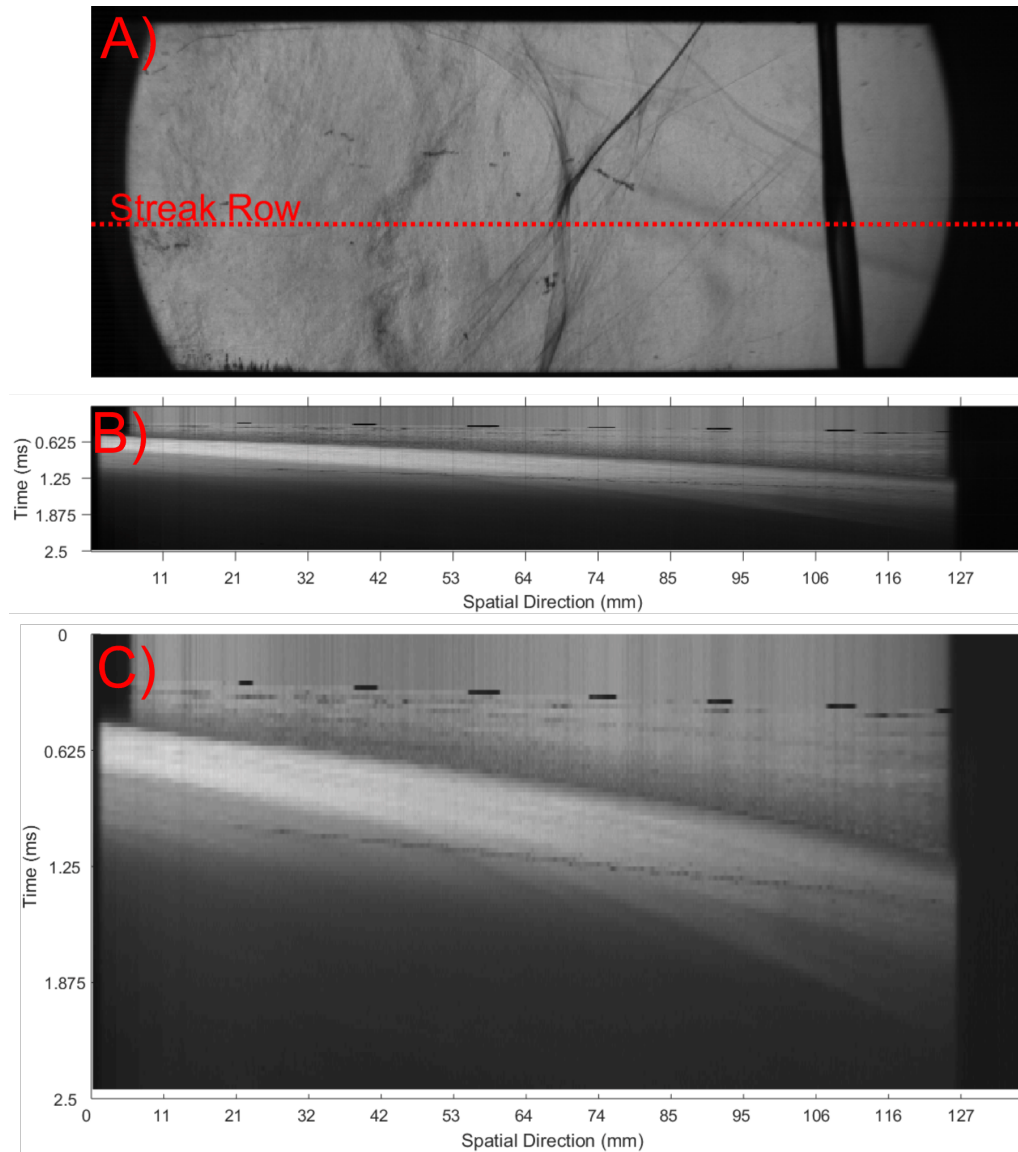


Figure 2.14: A) Schlieren imaging technique image with streak pixel location. B) Streak image presented as an image. C) Streak image presented as a surface.

CHAPTER 3

COMMON PATH SCHLIEREN IMAGING TECHNIQUE AND ABSORPTION IMAGING SPECTROSCOPY

The schlieren imaging technique and absorption imaging spectroscopy were applied on a common optical axis. A single arc lamp illuminated the optical components. A traditional schlieren imaging technique setup was used. However, before the receiving focal point a beam splitter was placed to send half the light to each optical instrument. Unique problems to this system, including correlation, alignment and diffraction effects on the absorption spectroscopy were overcome. A correlation procedure for the schlieren imaging technique and absorption imaging spectroscopy was explored.

3.1 Optical System Design

This system was housed in East Lab of the Torres lab Complex at the Energetic Materials Research and Testing Center (EMRTC), a research division of New Mexico Tech, located adjacent to campus in Socorro, NM. East lab is a dual chamber testing bunker. Chamber one was the control room from which the cameras were operated remotely along with the RISI FS-17 firing set used to initiate the detonator. The second chamber was the testing chamber with the Tunnel for High-speed Optical Research (THOR). In the middle of the chamber a 1 by 2 m optical table was placed. THOR was mounted to this table with six 31.75 mm square aluminum legs. The exit end of THOR was supported by a wooden structure. The optical table provided a rigid mount for all the optical components. The completed test setup is shown in Figure 3.1.

The system is diagrammed in Figure 3.2. The arc lamp was mounted facing into the bunker. A first surface mirror turned the expanded light into the first collimating lens. The field lenses were 700 mm focal length and 127 mm in diameter. THOR was mounted between the two lenses. The second lens refocused the light to a focal point. Before the focal point a beam splitter was placed. Half of the light was sent to the imaging spectrometer and the remaining light continued through a neutral density filter, knife edge, camera lens and into the Phantom V711 camera for the schlieren imaging technique. The light sent to the



Figure 3.1: Image of the installed THOR facility in the East Lab test chamber. Centered is THOR with the open exit section facing outward. Right side is the transmitting optics. Left side beyond THOR are the receiving optics.

imaging spectrometer was refocused with a 25 mm diameter 60 mm focal length lens. In Figure 3.3 the setup of the transmitting optics is shown with the light path overlaid. In Figure 3.4 the receiving optics are shown with the light path overlaid.

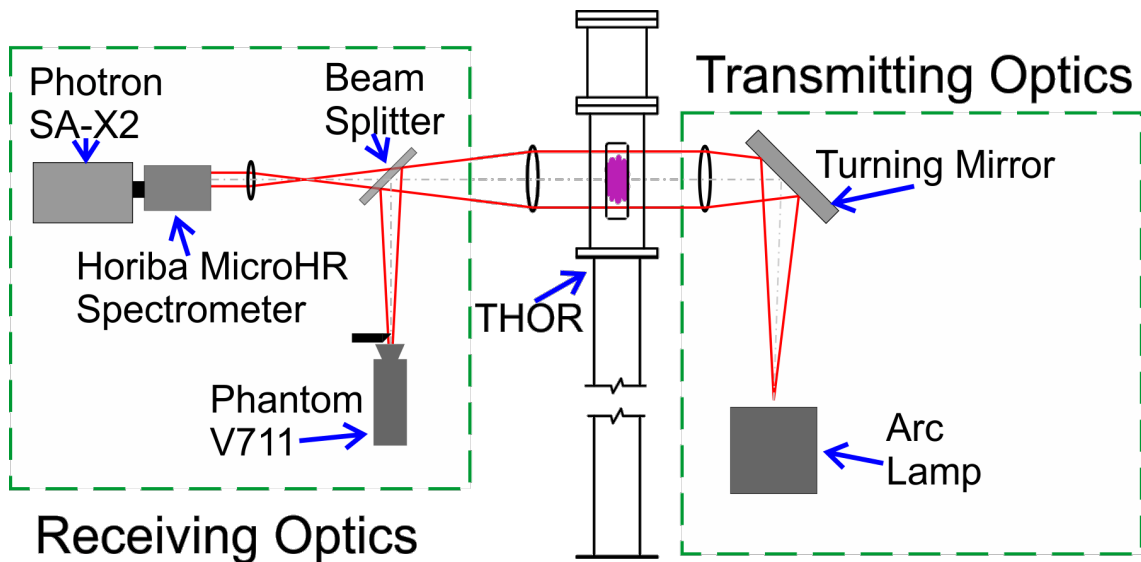


Figure 3.2: Diagnostic setup schematic

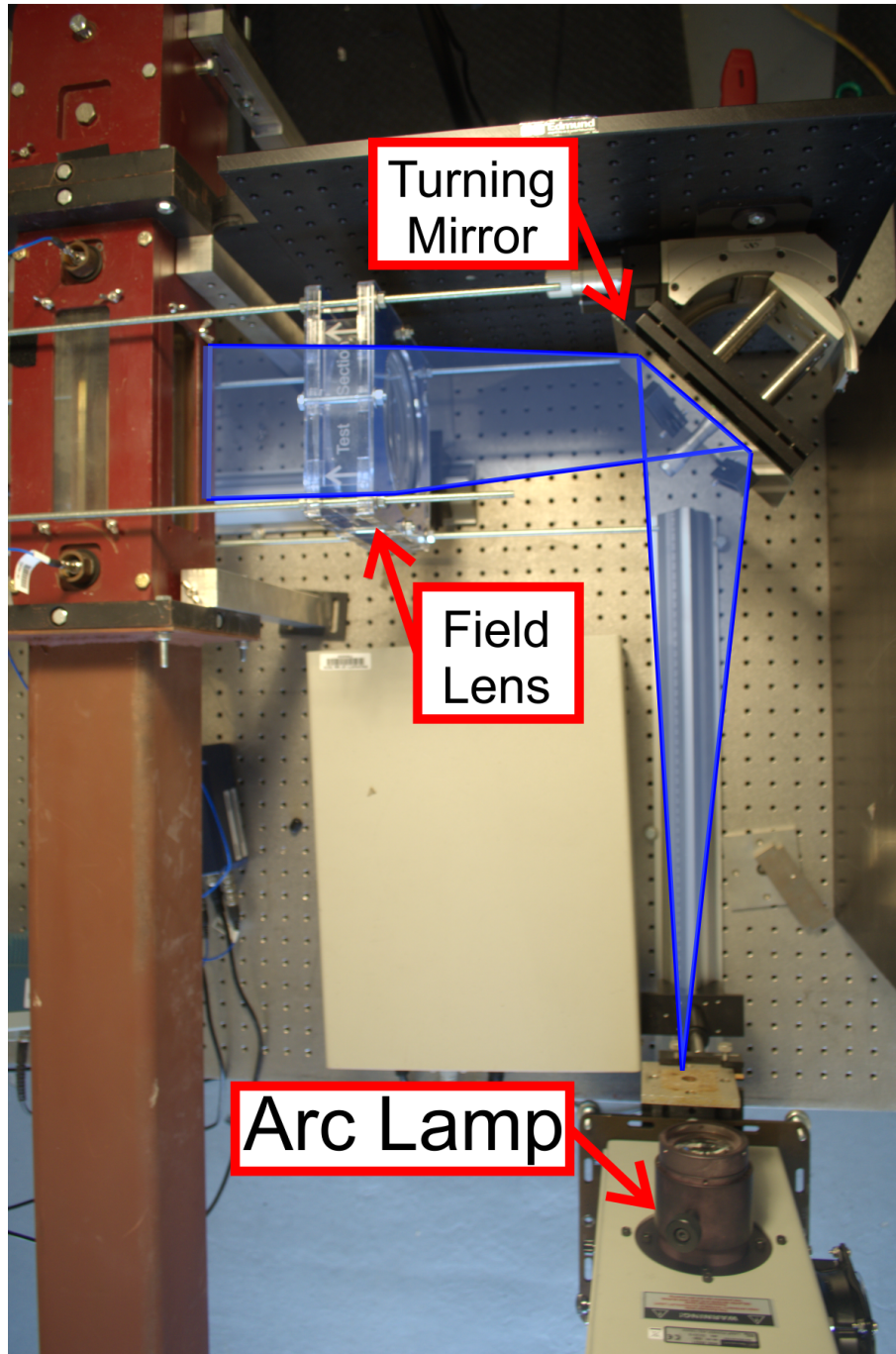


Figure 3.3: Image of the transmitting portion of the optical setup. Arc lamp is located on the bottom right. The light was sent to the turning mirror located on the top right. The light was directed through the field lens on the top left by the turning mirror.

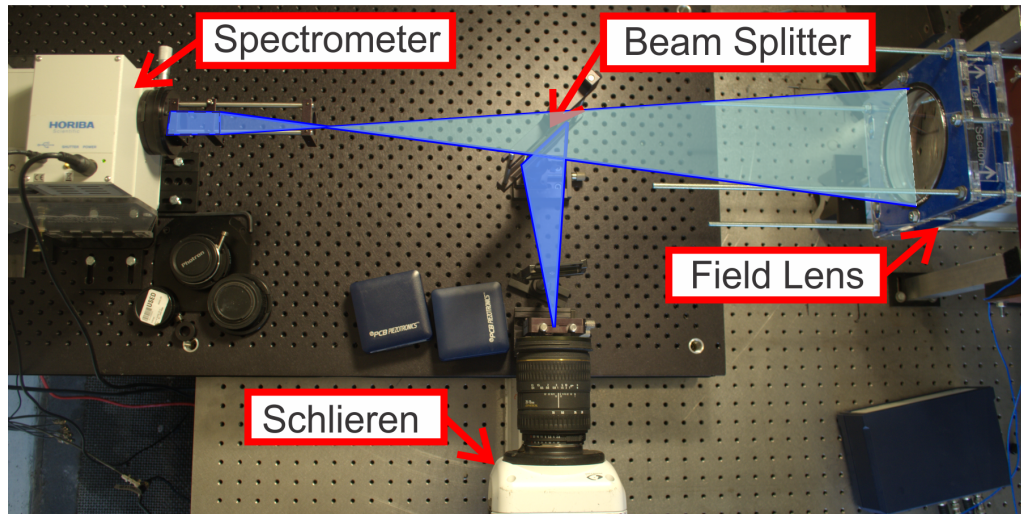


Figure 3.4: Image of the receiving portion of optics including the spectrometer and schlieren camera. The light comes from the collimated test section on located on the far right through the field lens. The beam splitter is located in the middle of the image. Half of the light was sent to the schlieren imaging technique optics located in bottom center of the image. Half of the light was sent to the spectrometer located on the left side of the image.

3.1.1 Light Source Characterization

A Xenon arc lamp was selected for illumination because both the schlieren imaging technique and absorption imaging spectrometer require a high intensity light source. Recording at 20,000 to 30,000 fps with maximum shutter speeds of 0.29 ms through optically dense materials required high intensity light input. The absorption imaging spectrometer also required a light source with continuous spectral output in the desired range of 450 to 650 nm.

The spectral output of the arc lamp was measured by the single point and imaging spectrometers. In Figure 3.5 the two spectral data sets are shown. The intensity of the imaging spectrometer's and single point spectrometer's spectrum was normalized to a maximum of one. In addition, the efficiency of the imaging spectrometer diffraction grating and Photron sensor with respect to wavelength is shown. The single point spectrometer trace shows the arc lamp's spectrum began at 375 nm and oscillates in intensity over the 425 to 700 nm range. The grating efficiency peaks at 580 nm with a steady decrease to zero at 300 nm. Above 600 nm the grating retains a high efficiency from 90 to 70 %.

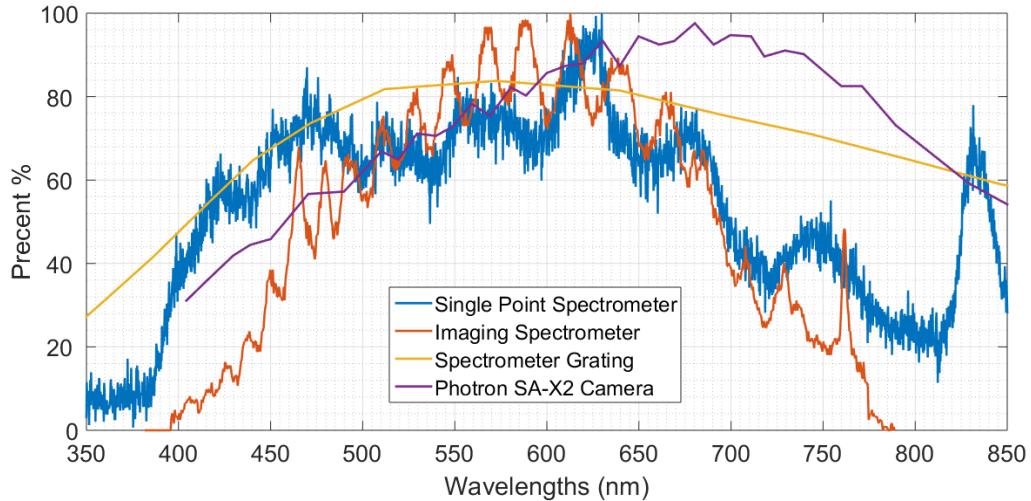


Figure 3.5: The efficiencies curves that dictate the spectral response. Included is the arc lamp spectrum, Photron Sa-X2 CMOS sensor and grating efficiency.

3.1.2 System Noise

Through testing it was determined the arc lamp introduced system noise due to temporal variations in the light output. To determine the noise of the spectrometer a test series was taken with no media present in the test section. The average image intensity of each frame was calculated and plotted with respect to time. The resulting graph shown in Figure 3.6 is sinusoidal. The arc lamp has a 2 % change in light intensity due to the flicker of the arc. An FFT analysis was performed and the noise was predominantly from a 130 Hz oscillation.

To correct for noise issues a baseline shift was applied to the data [21]. The spectral response of iodine is from 450 to 650 nm. Above this region from 650 to 725 nm there was no expected spectral response for any of the tests. The average absorption value from 660 to 675 nm was calculated at each spatial location. This value was subtracted from every wavelength at the spatial location. In addition Savitsky-Golay smoothing was applied to reduce small variations.

3.2 Correlation of the Schlieren Imaging Technique and Absorption Imaging Spectroscopy

In order to correlate the two optical systems the center location of each data set relative to the physical location was determined. The two systems were setup to final test conditions and a series of correlation images were recorded. Several different steps were required due to the two systems recording different

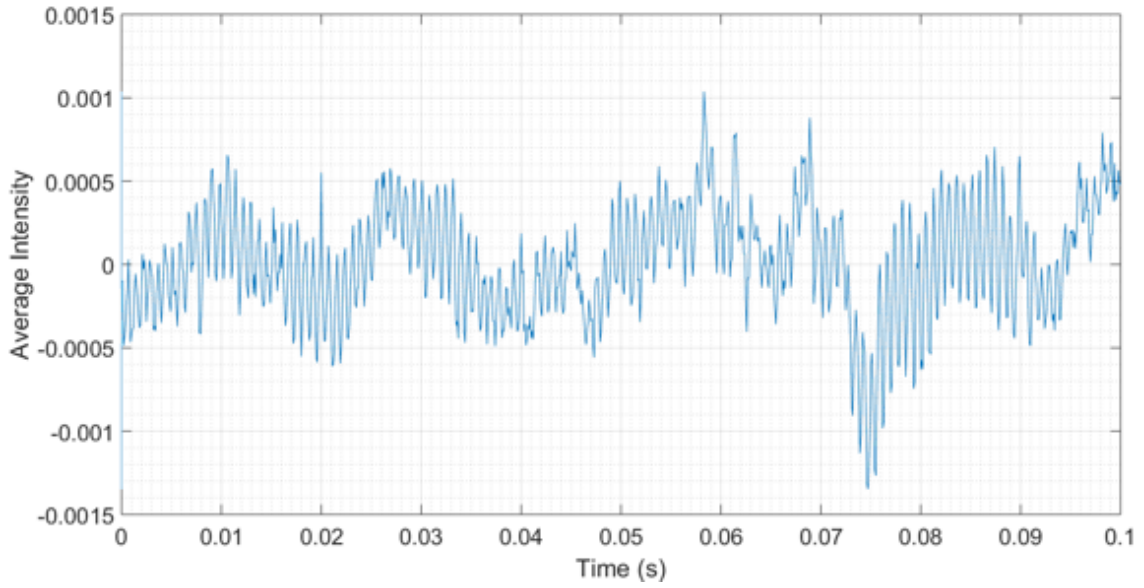


Figure 3.6: Average arc lamp flicker over time.

types of data.

Since the imaging spectrometer only records spatial information in one dimension and averages the light intensity over the second physical dimension the location and height of the viewing window is required. A light block was translated vertically upwards through the test section. When a negative shift of pixel intensity was detected an image was recorded with the schlieren and spectroscopy cameras. This image sets the lower bound of the imaging spectroscopy window. The process was repeated for the upper bound of the imaging spectroscopy window by translating vertically downwards through the test section.

Next a gauge block was placed into the the test section and an image was recorded with both cameras. The pixel center of both data sets was determined. The pixel distance to one edge of the block was determined for both data sets. Figure 3.7 is an example of this correlation process. The edges considered for this correlation are highlighted with dashed lines. The imaging spectrometer calibration image was slightly out of alignment causing a gradient in the spatial dimension. The alignment issues are from less than one degree of rotation off the optical axis. The alignment methods employed could not provide the precision needed to achieve perfect alignment. The imaging spectrometer had to be collinear to the optical axis and the Photron sensor had to be normal to the spectrometer's instrument optical axis. The Photron being a 12 kg camera makes this alignment difficult with traditional optical components.

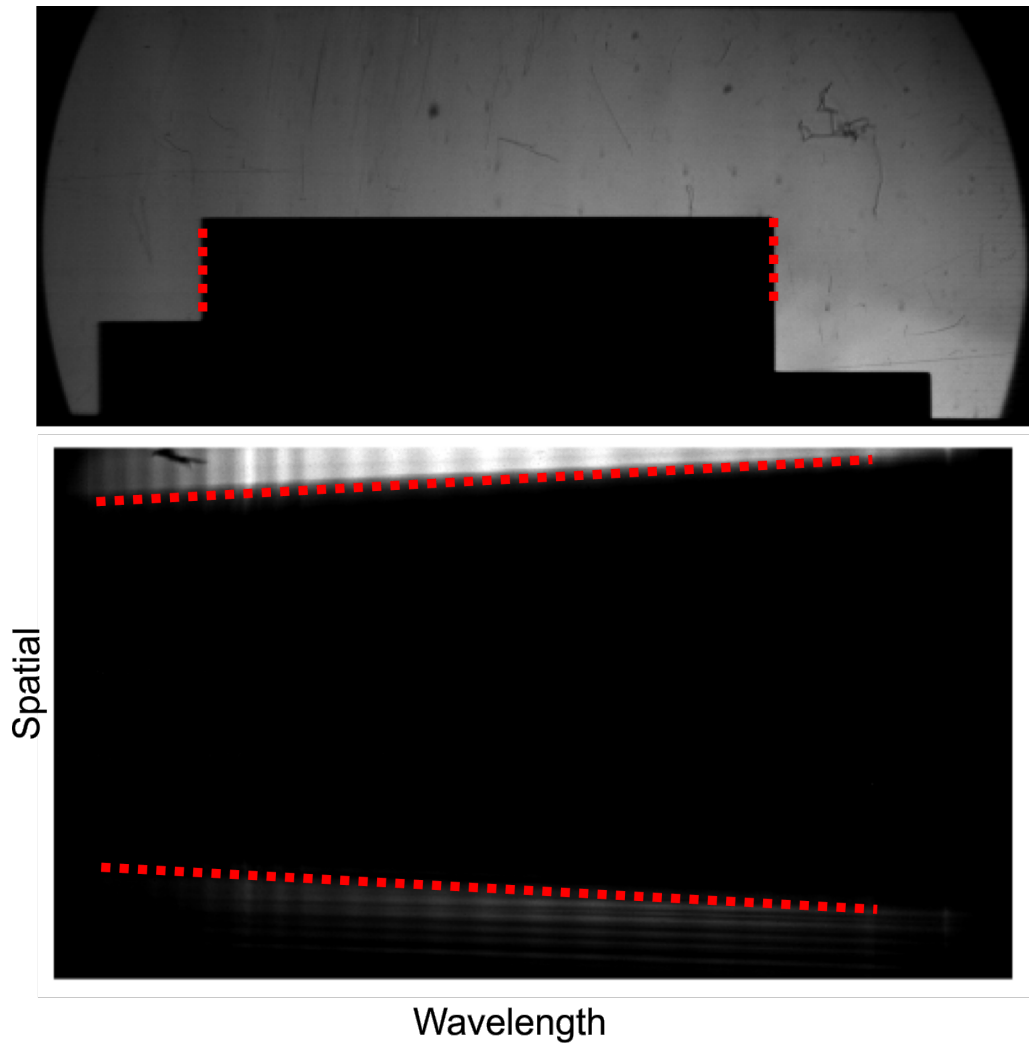


Figure 3.7: Top image is a gauge block located inside of the test section recorded with the schlieren imaging technique system. Bottom image is of the same gauge block recorded with the imaging spectrometer.

CHAPTER 4

IODINE PLUME VALIDATION EXPERIMENTS

A simplified test series was performed to determine system performance and required testing methods. Iodine gas was injected into THOR and analyzed with schlieren imaging technique and absorption imaging spectroscopy. Determining the relative concentration and location of the iodine cloud was the primary objective of this test series. The moment of first injection to fully filled test chamber was measured. This testing showed the repeatability and sensitivity of the system. The effect of residual iodine in the test chamber was examined and determined to be a source of error.

4.1 Test Methods

Iodine crystals were sublimated in a steel reaction vessel with a butane torch to produced iodine gas. To increase the velocity and visibility of the flow inside of the test chamber, helium was used as a push gas. The test setup is shown in Figure 4.1. For each test 50 to 100 mg of iodine powder was loaded into the steel reaction chamber. The lower THOR window was replaced with an aluminum plate which provided a connection for the reaction vessel. A helium supply line was connected to the steel chamber. Flow was controlled with a manual ball valve. The helium gas entered the chamber at 100 kPa through a 6.35 mm orifice. The chamber was heated with a butane propane torch for 90 s. The steel chamber surface temperature was approximately 150 °C. The ball valve was then opened to release the helium-iodine gas mixture into THOR. The complete optical system, schlieren imaging system and absorption imaging spectroscopy were triggered simultaneously.

4.2 Helium Gas Plume

The effect of the helium gas was first analyzed with no iodine present. Heat was not applied to limit residual iodine from sublimating in the test section. In Figure 4.2 two frames are shown, first when the helium jet has entered the schlieren imaging technique image before entering the imaging spectroscopy

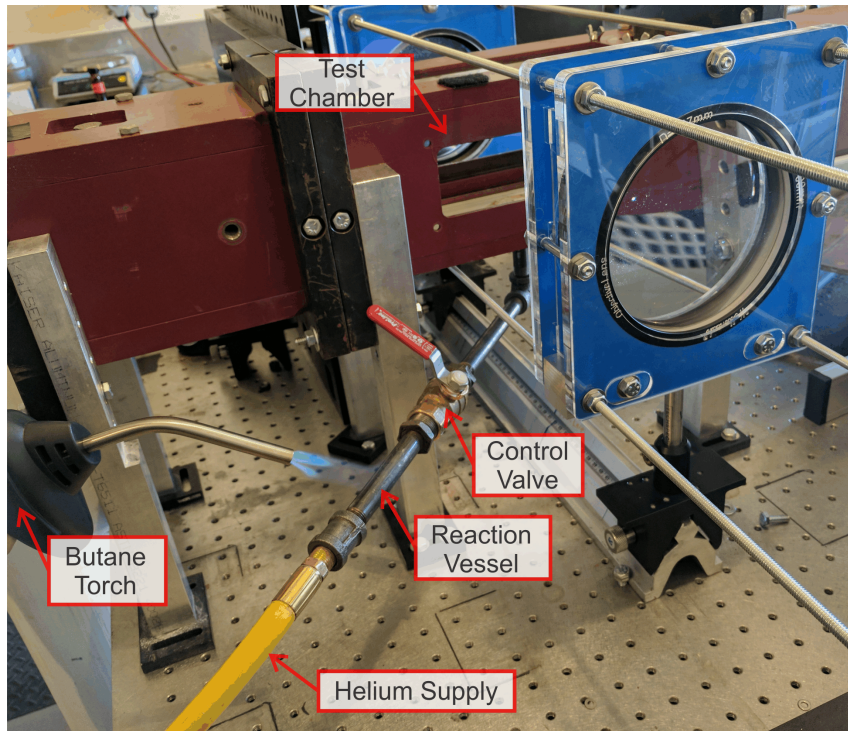


Figure 4.1: Test setup for iodine gas plume measurements.

region. The second frame shows when the jet has filled most of the vertical region of the schlieren imaging technique image. In the top image of Figure 4.2 the imaging spectroscopy data has no response. The jet then continues to grow with time at 6.3 ms the plume has reached full width at 20 mm. The helium gas front has a velocity of approximately 6 m s^{-1} . In the region of the plume the imaging spectroscopy data has more noise than the surrounding regions.

In Figure 4.3 the spectral response is plotted at three spatial location. The middle location is within the helium gas plume. The frame time for image is the same as the previous image set. The spectral response is only a background signal caused by the jet in the spectral band.

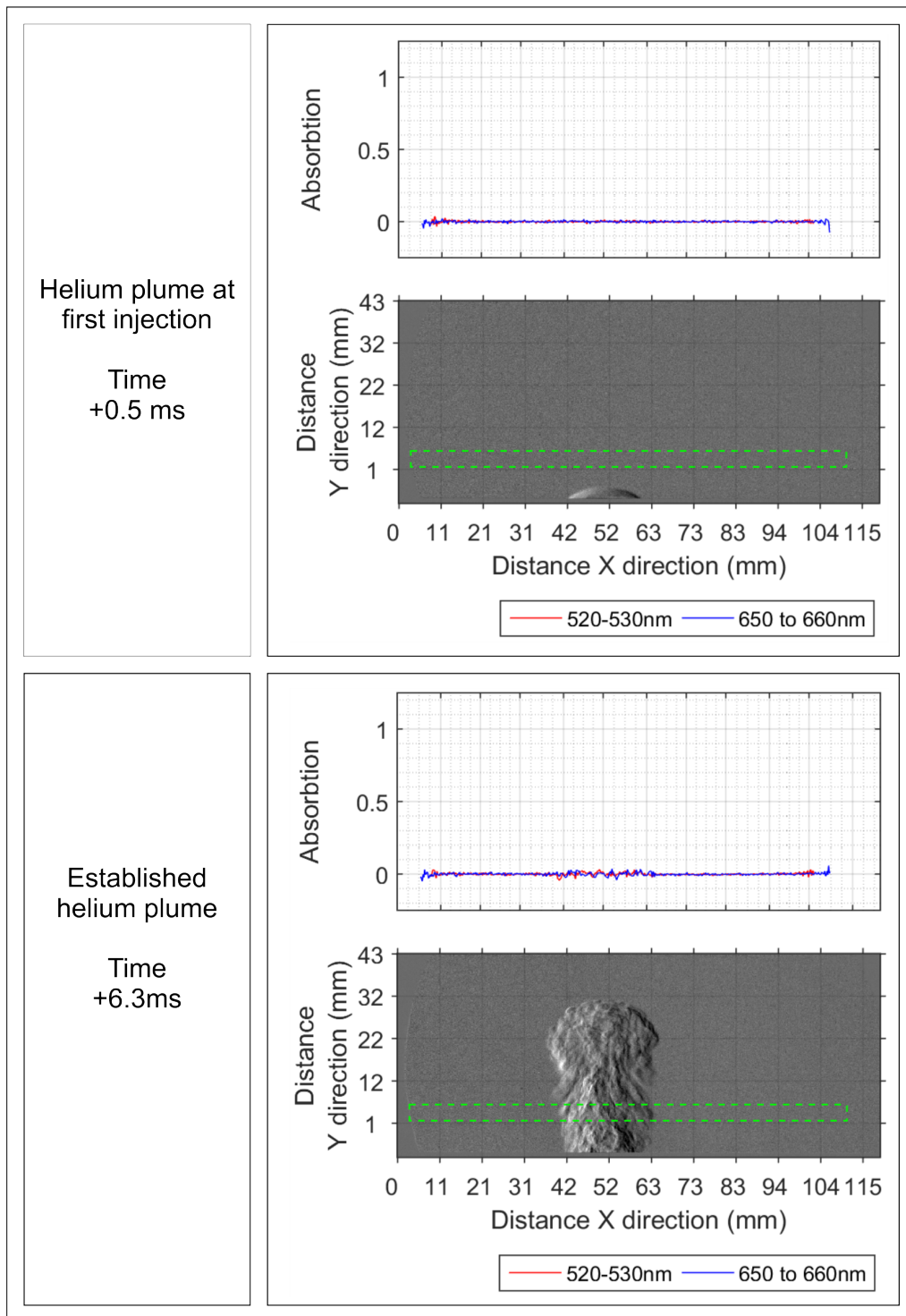


Figure 4.2: Helium gas plume response shown with two wavelength regions

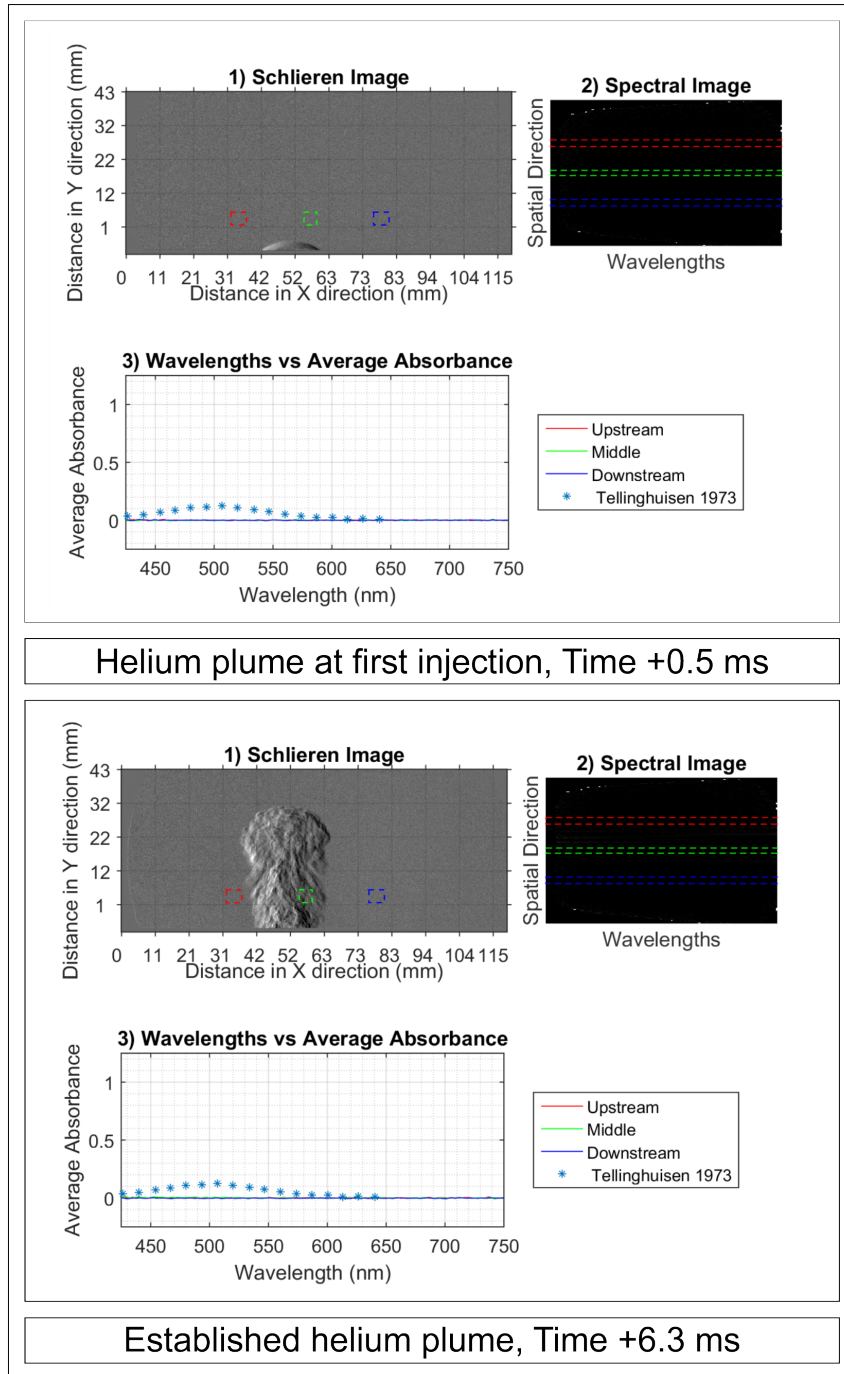


Figure 4.3: Helium gas plume response shown with three spatial regions

4.3 Helium-iodine gas plume

Iodine gas was then added to the helium gas plume by the described sublimation process. During testing a pink purple hue was noted in the gas plumes, indicative of iodine gas being present. This testing was repeated three times, each time with 50 to 100 mg of iodine per test. The first test was conducted with clean optical windows, the second test the windows were cleaned with soap and water, the third test was conducted with no side windows. From prior research, it was unclear if trace iodine was deposited on the windows and what effect this could have on the spectroscopy data. From this testing it was noted trace iodine does change the spectral response. Test two was processed with both a tare image from the used window and from a clean window. Results showed a discrepancy it was determined that each test requires brand new clean windows.

Seen in Figure 4.4 the helium gas plume was present in the test chamber for 24.3 ms, at this time the spectral response in the 520-530 nm region begins to change. This graph shows the average absorbency from 520 to 530 nm and 650 to 660 nm. The work by Tellinghuisen plotted in Figure 4.5 describes the iodine peak at 520 nm [24]. The literature spectral profile is plotted along with the spectral response at three locations within the test section. This figure shows the spatial region near the plume having characteristic iodine trends.

The iodine-helium gas plume continued to grow, at 33.3 ms the spectral response is characteristic of iodine being present. The same two plot types are shown for this time. In Figure 4.6 the width of the gas plume has an elevated spectral response in the peak wavelengths. The highest absorption occurs in the middle of the plume with the response falling to zero at the edges as would be expected for a circular jet. Figure 4.7 from 500 to 650 nm the spectral response of the middle spatial location closely matches the expected response. However below 500 nm the response does not match.

The helium-iodine gas plume continues to fill the test chamber at 37.3 ms the spectral response at the peak wavelength is lowered as more helium gas enters the test chamber. The two plots are shown in Figures 4.8 and 4.9. After this time the iodine continues to remain in the test section at a lowered concentration level.

The absorption at the peak wavelength was recorded for each frame. This was then normalized from zero to one to produce a relative concentration of iodine with regards to time. Three frames are shown; 24.3, 30.5, and 33.25 ms. At 30.5 ms the maximum relative concentration was found. Of note the regions which iodine gas is present feature a high level of absorption, making the plume darker than a pure helium gas plume.

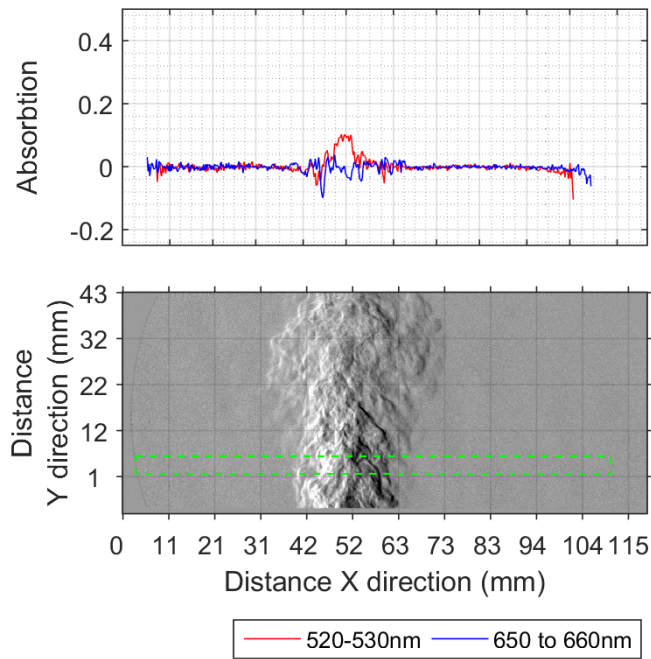


Figure 4.4: Start of helium-iodine gas plume in the test chamber shown with two wavelength regions.

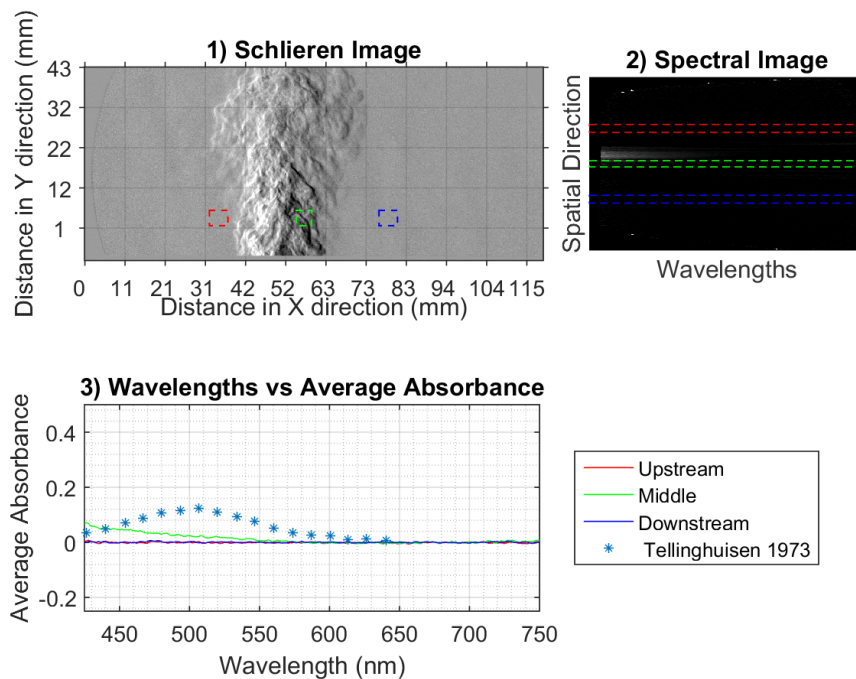


Figure 4.5: Start of helium-iodine gas plume in the test chamber shown with three spatial regions.

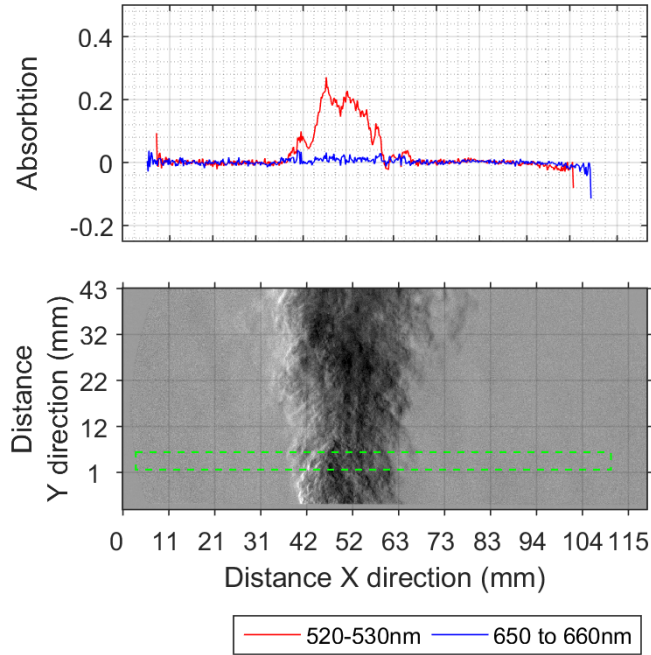


Figure 4.6: Helium-iodine gas plume in the test chamber shown with two wavelength regions.

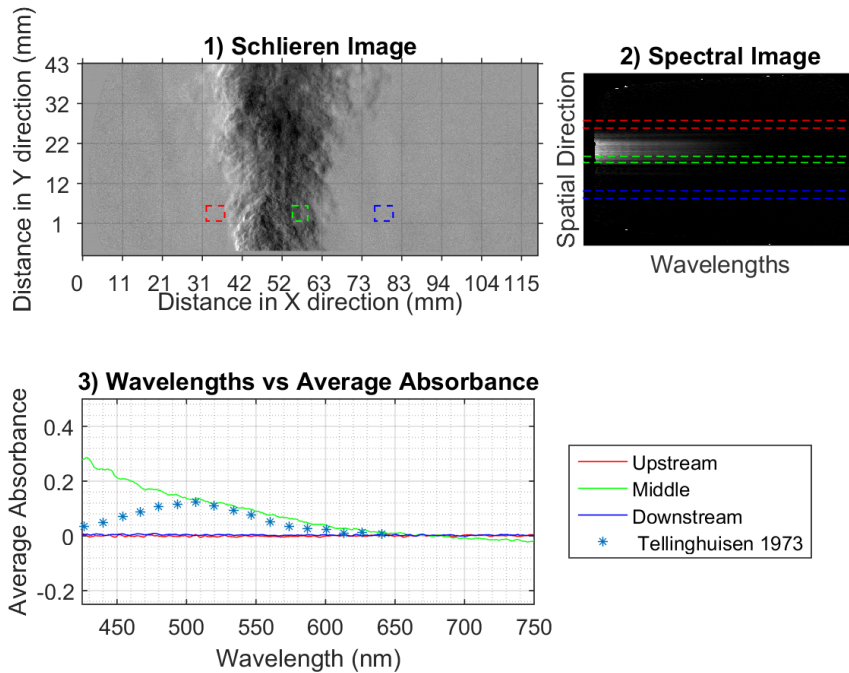


Figure 4.7: Helium-iodine gas plume in the test chamber shown with three spatial regions.

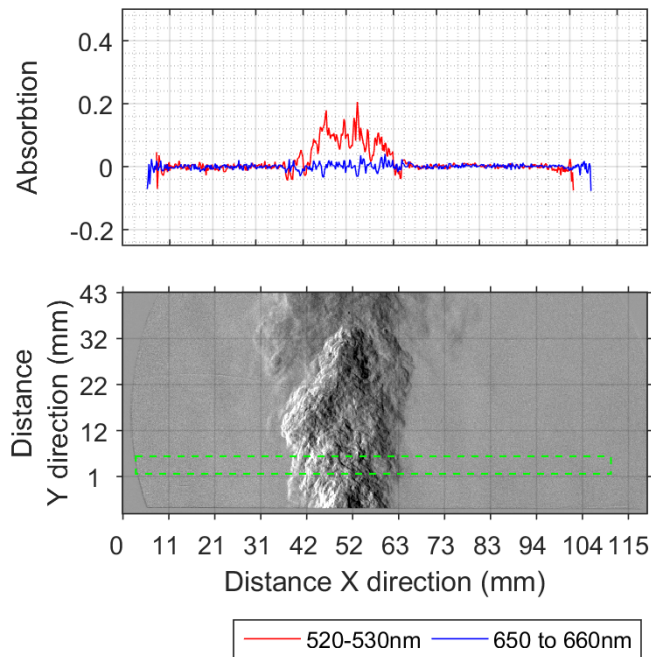


Figure 4.8: Reduced iodine gas concentration in the plume in the test chamber shown with two wavelength regions.

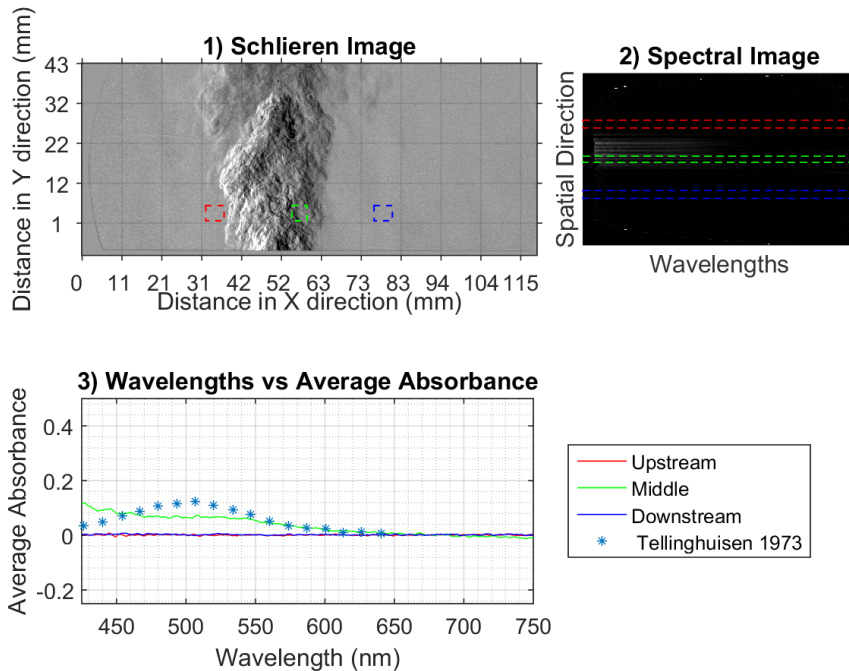


Figure 4.9: Reduced iodine gas concentration in the plume shown with three spatial regions.

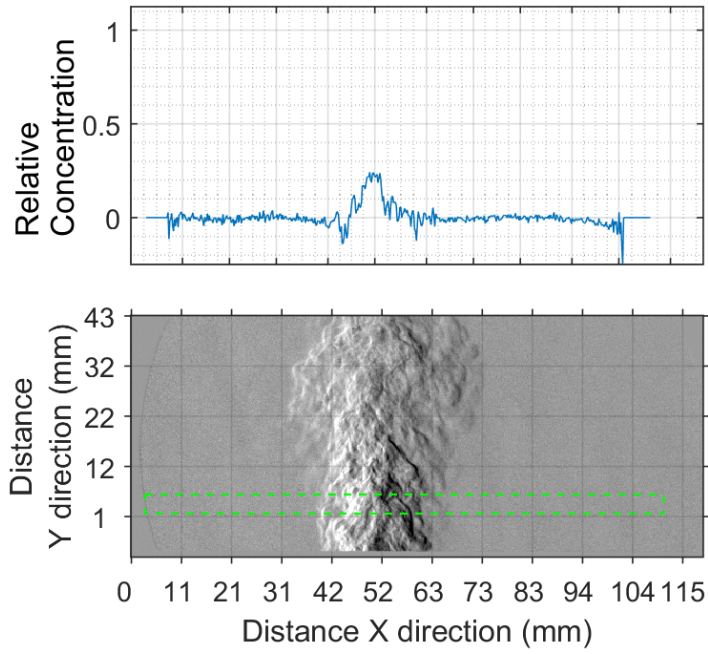


Figure 4.10: Relative concentration of iodine gas in the test chamber at 24.3 ms

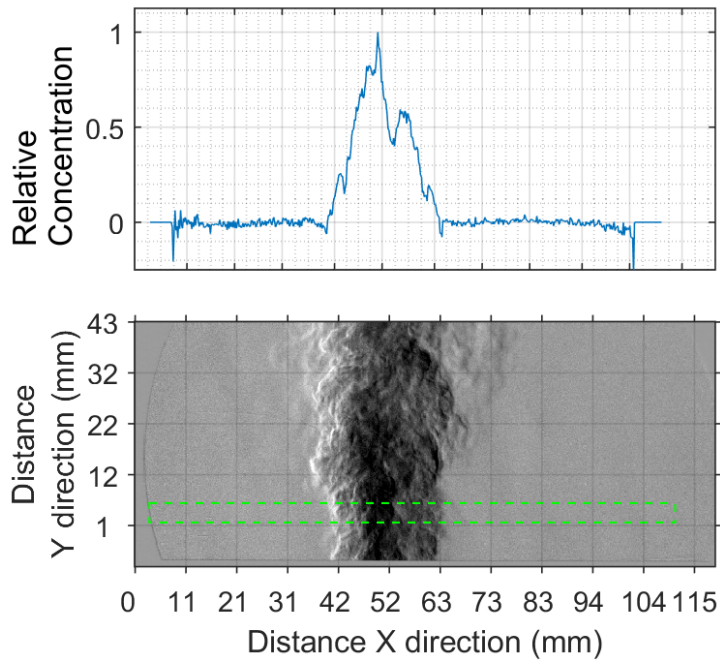


Figure 4.11: Relative concentration of iodine gas in the test chamber at 33.3 ms

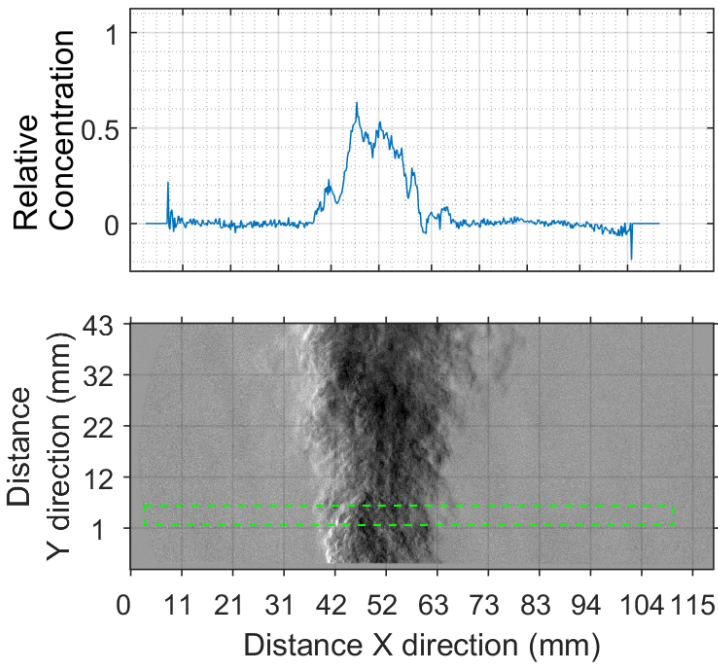


Figure 4.12: Relative concentration of iodine gas in the test chamber at 33.3ms

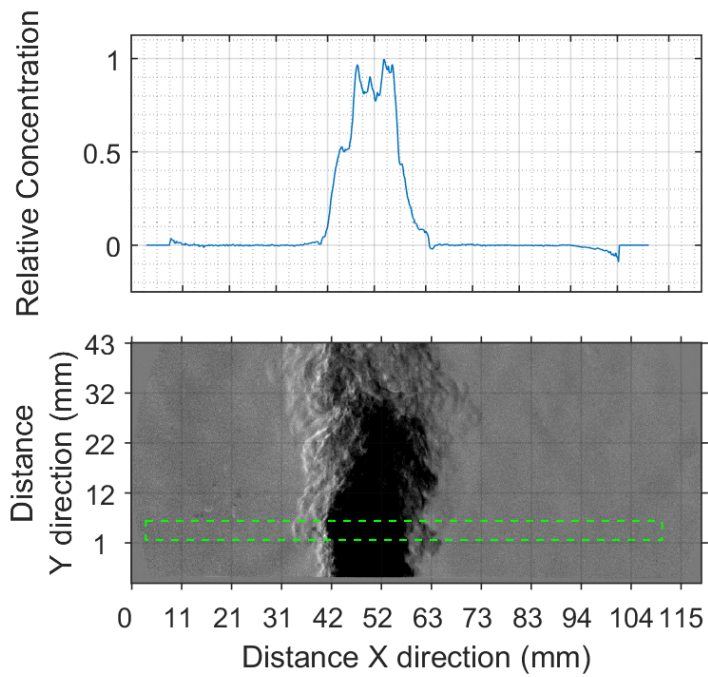


Figure 4.13: Higher concentration of iodine gas at 20 ms. The schlieren imaging technique image is dark in the center of the plume.

4.4 Data Analysis

The three tests are summarized in Table 4.1. All three tests had similar initial gas velocities at 4 m s^{-1} . The time for iodine gas to be present in the test chamber varies over 10 ms. Tests one and two took approximate 5 ms to reduce the concentration of iodine gas from the peak value. Test three had a stronger spectral and schlieren imaging technique response to the iodine and required 16 ms to observe a decreased iodine gas concentration. The frame that features the highest concentration of iodine gas is shown in Figure 4.13. During test three the spectrometer recorded complete light absorption from 450 to 550 nm for 6 ms. The absorption Equation 2.2 becomes non-physical at 90 % due to the log term. To avoid this a simple boundary was added setting regions of greater than 90 % absorption to one.

Table 4.1: Experimental Conditions

Test	Iodine Gas Present (ms)	Iodine Peak Gas Concentration (ms)	Reduced Iodine Concentration (ms)	Initial Gas Velocity (m s^{-1})
1	24	33	37	4
2	17	23	29	4
3	14	21	37	4.

The spectrometer and schlieren imaging technique data sets were successfully correlated in both spatial and temporal. Background signal from the helium gas was isolated with a baseline shift. Regions of iodine were identified with absorption imaging spectroscopy. These regions match well with expected results of higher iodine gas concentration in the center of the gas plume trending towards zero at the gas plume edges. The three tests demonstrated the repeatability of the system. A bound to the absorption values greater than 90 % was determined and test three reached full light absorption.

CHAPTER 5

SHOCK WAVE INTERACTION WITH IODINE PLUME EXPERIMENTS

A simple test series using shotgun primers and a helium-iodine gas plume were examined for turbulent mixing and system performance. First a shotgun primer with no gas plume in the test chamber was used to examine a shock wave and explosive product gases with the schlieren imaging technique and absorption imaging spectroscopy. There is no known spectral response in the 450 to 600 nm of the lead styphnate ($C_6H_9N_3O_8Pb$) and barium nitrate $Ba(NO_3)_2$ commonly found in 209 shotgun primers. The pure 209 primer test allowed for characterization of the spectral response and gas motion in the test chamber independent of a helium-iodine plume.

Then tests with a helium-iodine gas plume present in the test chamber were performed after the background signals were isolated. The shotgun primer produced a shock wave and the plume introduced helium-iodine gas into the chamber. The ultimate goal of testing was to combine a shock wave with iodine gas rich explosive products using $Al-I_2O_5$ thermite driven with a RP-2 detonator. Thus it is vital to understand basic shock interaction with the spectral data, explosive product mixing and determine methods to extract relative concentration from the spectral data sets.

5.1 209 Shotgun Primer Test Series

A 209 shotgun primer was used for a simple a shock wave source. This primer was initiated with a spring loaded firing pin pen style flare launcher. The flare launcher was mounted to the breech block, the Swagelok mounting plate was replaced with a plate that had a 12.7 mm hole in which the flare launcher was placed. The block was inserted into the first 25 mm of the optical diagnostic section. The schlieren imaging camera recorded at 30,000 fps with an exposure of 0.29 ms. The spectral data was recorded at 30,000 fps with an exposure of 0.29 ms.

5.1.1 Background Signal Processing

A unique background signal was identified when the spectrometer captured several regions of negative absorption or an increase in light intensity. The Beer-Lambert law requires collimated light rays through the test section. Regions which have been diffracted deviate from the law and are non physical. This was observed with the 209 shotgun primer test series and again in later testing. In Figure 5.1 the spectroscopy data is compared to the schlieren imaging technique images for a shock wave produced with a 209 primer. The shock wave has a clear relation with the peak in absorption followed with a non physical negative absorption value. The 209 shotgun primers had a weaker signal than the signal produced with a RP-2 detonator. This is related to the structure and strength of the shock wave.

The same baseline shift as discussed in Section 3.1.2 needed for correcting for system noise was found to reduce this refraction signal. In Figure 5.3 this processing is shown with two wavelength averages over the spatial dimension. Before the baseline shift was applied the spectrum is uneven. After the baseline shift, shown in the lower image, the response from 520 to 530 nm was isolated. Testing with the RP-2 detonator showed similar trends. The shock wave observed in this testing is shown in Figure 5.2. This figure includes the spectral response, schlieren imaging technique images and the absorption profile image. The cyan rectangle detonates where the baseline shift information was taken from. The shock wave in the schlieren imaging technique images is black due to a change in the orientation of the knife edge. The absorption profile image shows a white band indicating a high absorption in the region of the shock wave across all wavelengths sampled. After the baseline shift this band was reduced. This baseline shifting is not completely successful due to the spatial gradients within the spectral data sets causing system noise. The higher wavelengths have a lower mm per pixel relationship causing the shock wave to have a wider spatial appearance at the high wavelengths.

A second approach to visualize the data cube is shown in Figure 5.4, three spatial locations were selected and the spectral response at each location was plotted. The baseline shift method does not correct for all background signals of the spectral data. In Figure 5.4 the normalized spectra response has iodine like trends. This may have been from trace iodine left in the test chamber or a product of the explosive gases.

5.1.2 Data analysis

In the top image of Figure 5.5 the schlieren imaging technique images were used to create a streak image of the test. The spectral response before the baseline

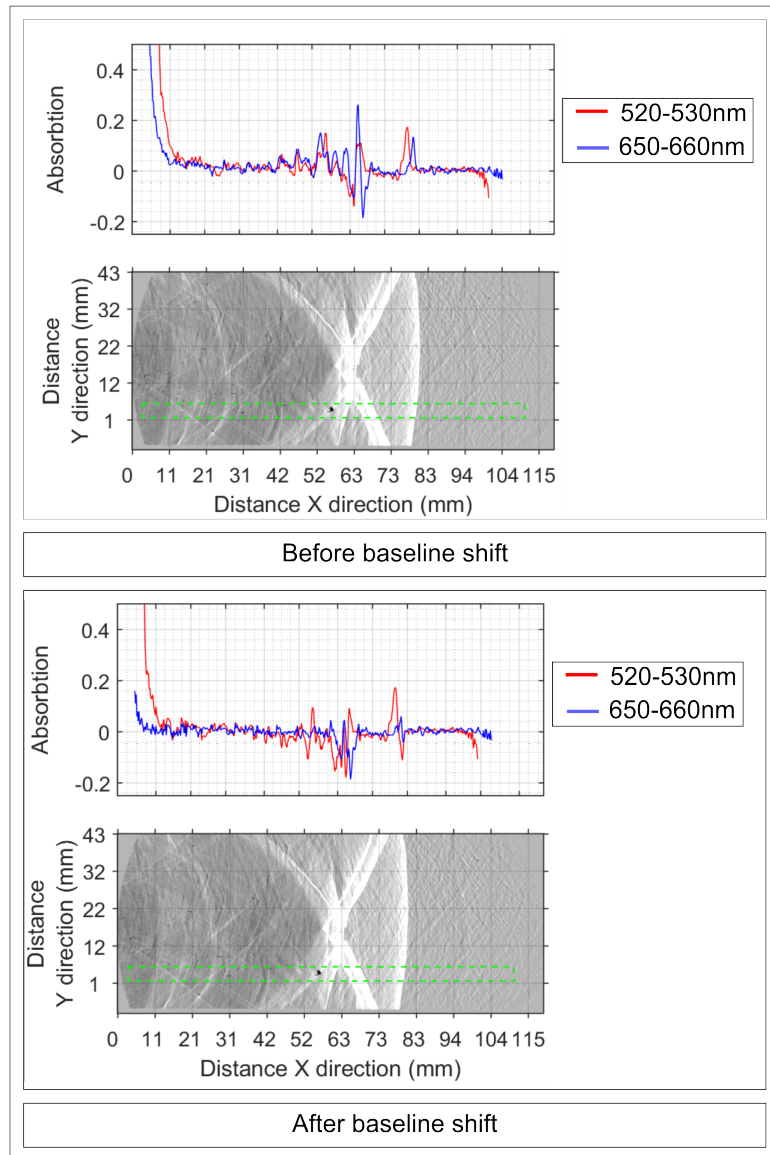


Figure 5.1: Schlieren imaging technique images and absorption imaging spectroscopy images showing the effect of the 209 primer shock wave. The schlieren image has as strong transition from white to gray at the region of the shock. The spectroscopy data has a peak that is located at the same time and position. The lower image set has had a baseline shift applied. The noise is reduced, however there are still several peaks related to the shock wave.

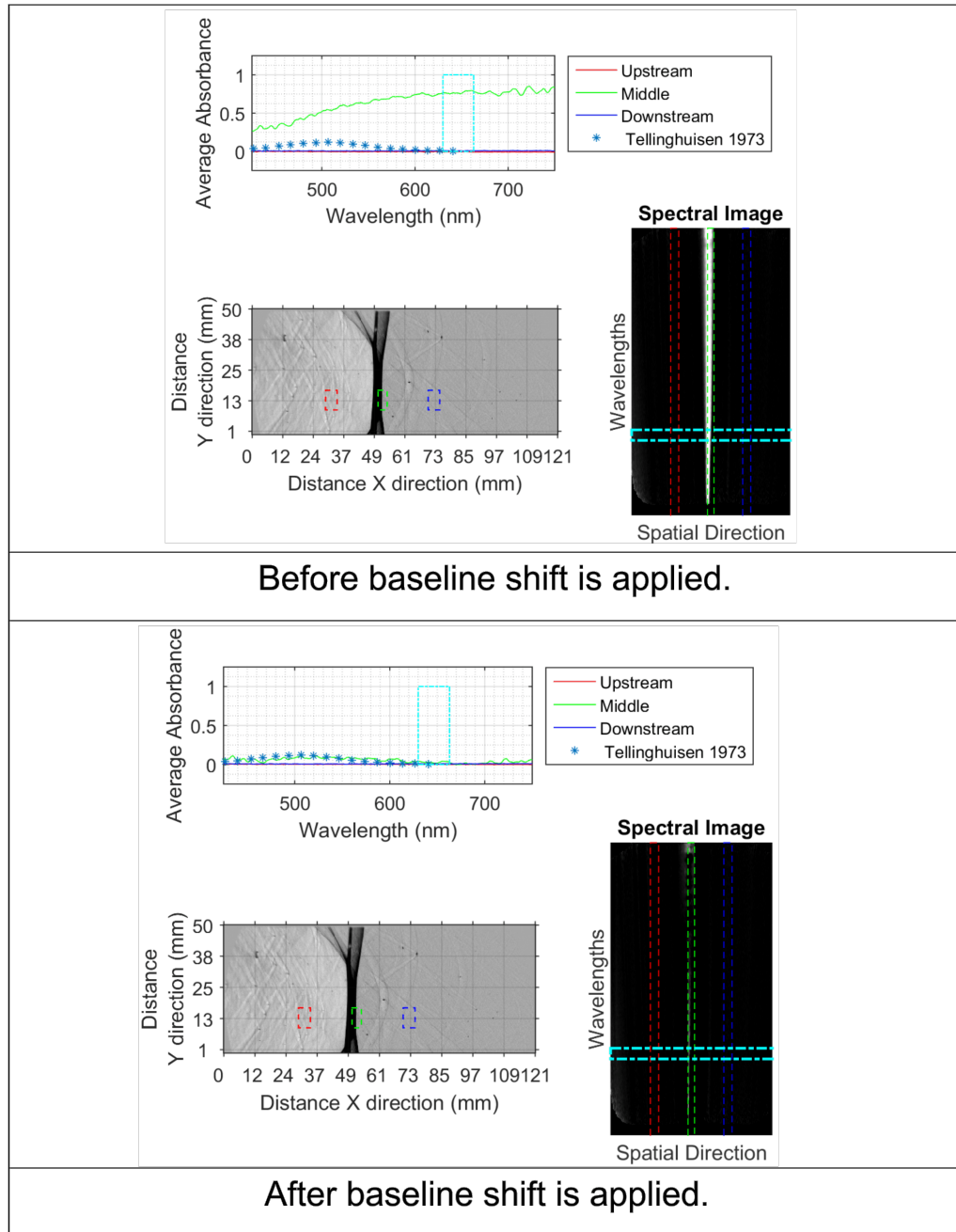


Figure 5.2: Two image sets including spectral response, schlieren response and absorption profile image showing the RP-2 detonator shock wave. Top image is before the baseline shift has been applied. A white band in the absorption image is the shock wave. The cyan rectangle is the region in which the baseline absorption shift was calculated. In the lower image the spectral response has been shifted based on the response from 660 to 675 nm. The white band in the spectral image was reduced.

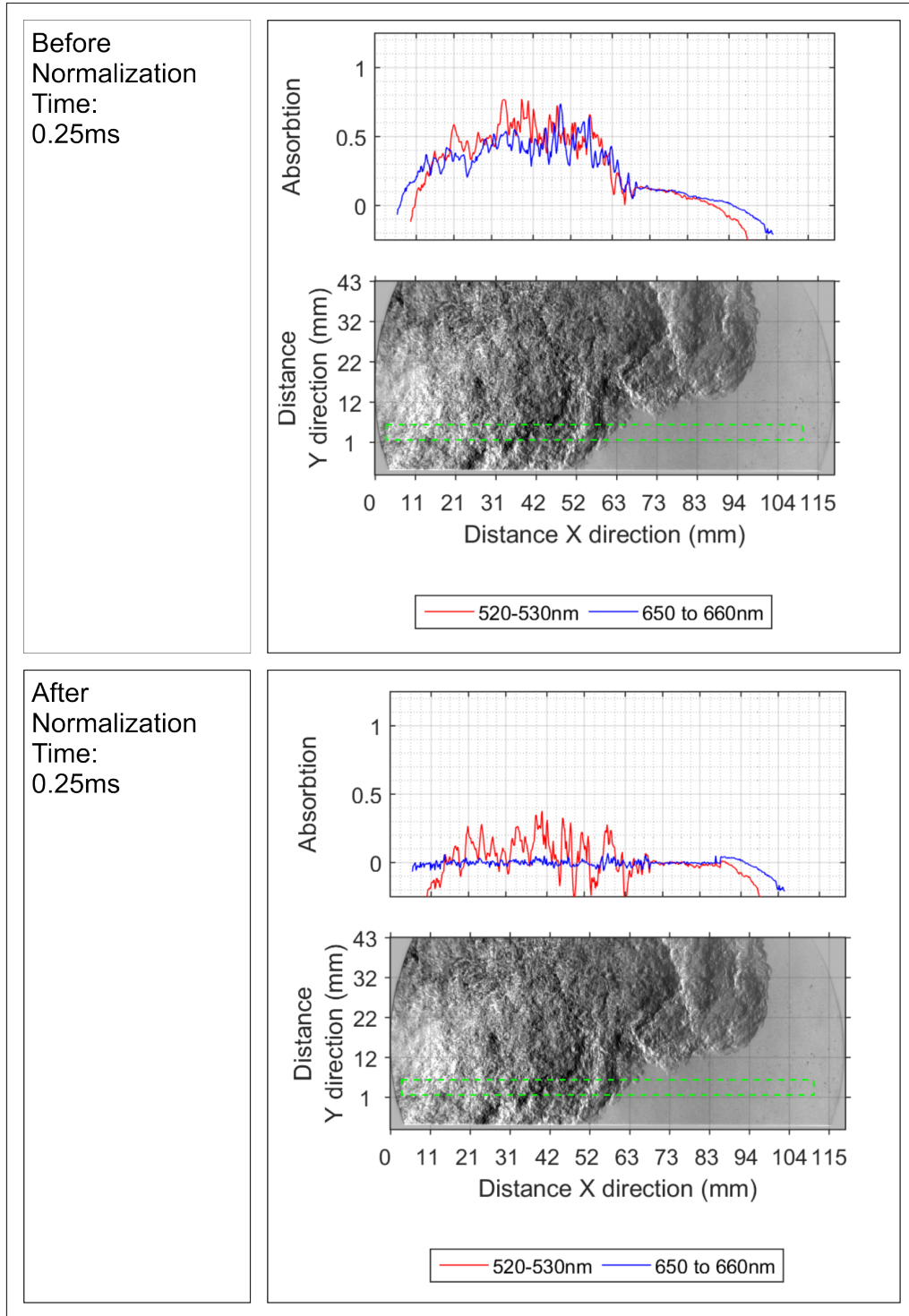


Figure 5.3: Top image is before normalization has been applied, the 520-530 nm trend is difficult to analyze. In the lower image the spectral response has been normalized based on the response from 660 to 675 nm.

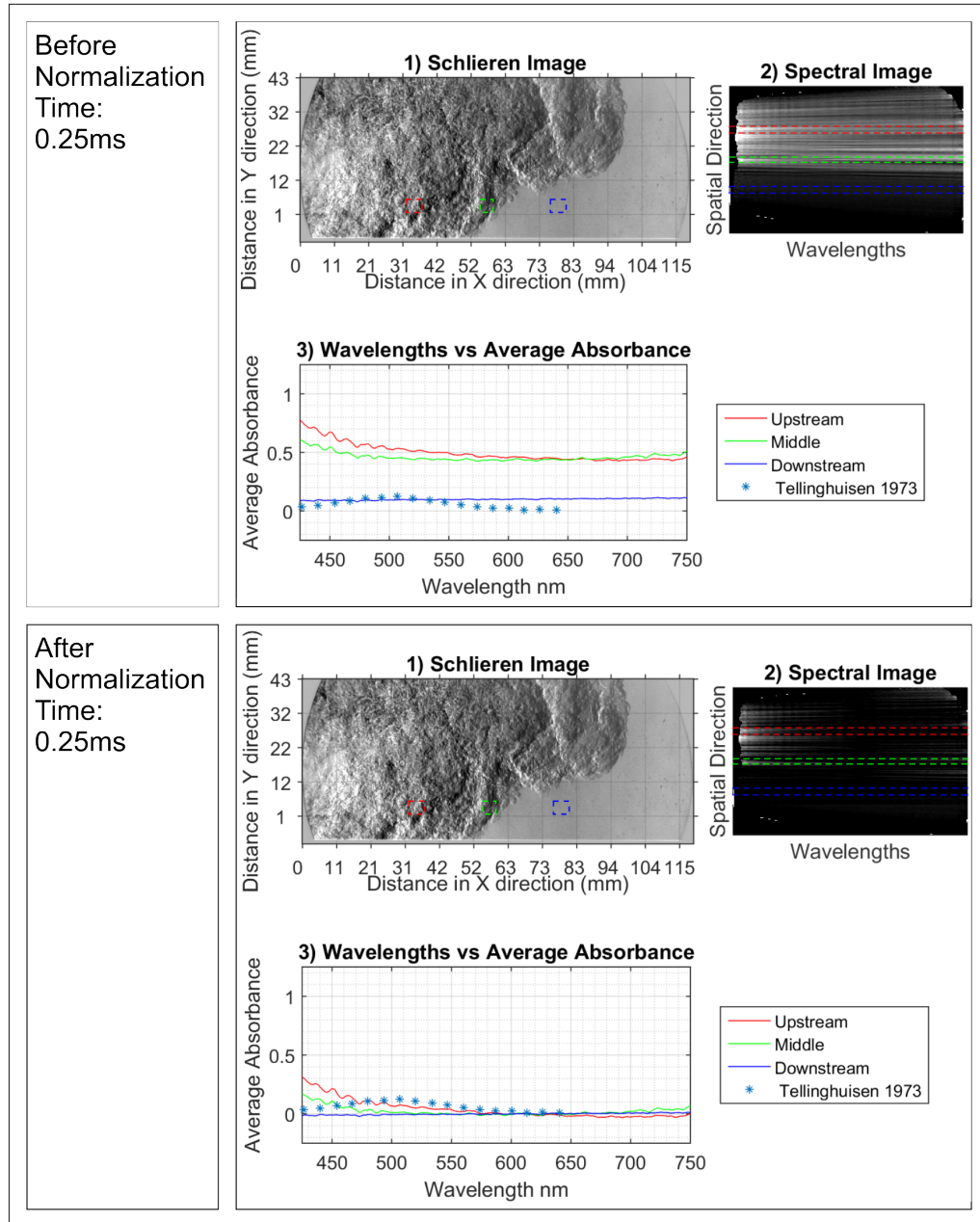


Figure 5.4: Schlieren imaging technique image and absorption imaging spectroscopy image showing the effect of the explosive gas products from a 209 shotgun primer. The schlieren imaging technique image shows a large turbulent cloud in the test section. Before the background signal is removed the upstream and middle locations show absorption values above 0.5. After the baseline shift the absorption values are zero. Below 500 nm there is an upward trend to the spectral response. Trace iodine left in the test chamber maybe a cause, the chamber had iodine present 15 minutes prior to this test.

shift is plotted as a three dimensional surface as shown in middle image of Figure 5.5. The color of the graph shows the relative absorption in the 520 to 530 nm region. At 0.5 ms the shock wave enters the test section followed by the explosive product gases. The shock wave is a series of peaks traveling from left to right as expected. The gases enter and begin to slow down. Initially the gases cause a large absorption increase and then diffuse over time.

The baseline shift was then applied and is shown in bottom image of Figure 5.5. The spectral signal of the product gases were removed. The strong absorbency signal caused by the shock wave was removed from the data set. The overall absorbency of the product gases was decreased to noise centered around zero. Sharp refraction regions such as between the product gases and ambient air have also been removed. This data set also showed that the edges of the spectroscopy data are predominantly noisy. Suggesting that stray light or other grating effects were involved. These regions were then removed by cropping the spectral images.

This testing demonstrated that background optical signals such as an optically dense gas cloud or noise from a shock wave could be removed from the spectral data set with a baseline shift. This method does not have complete success with isolated peak structures. A more detailed approach is needed to correct for this background signal. However with a complimentary schlieren imaging technique image peak structures and noise are identified easily.

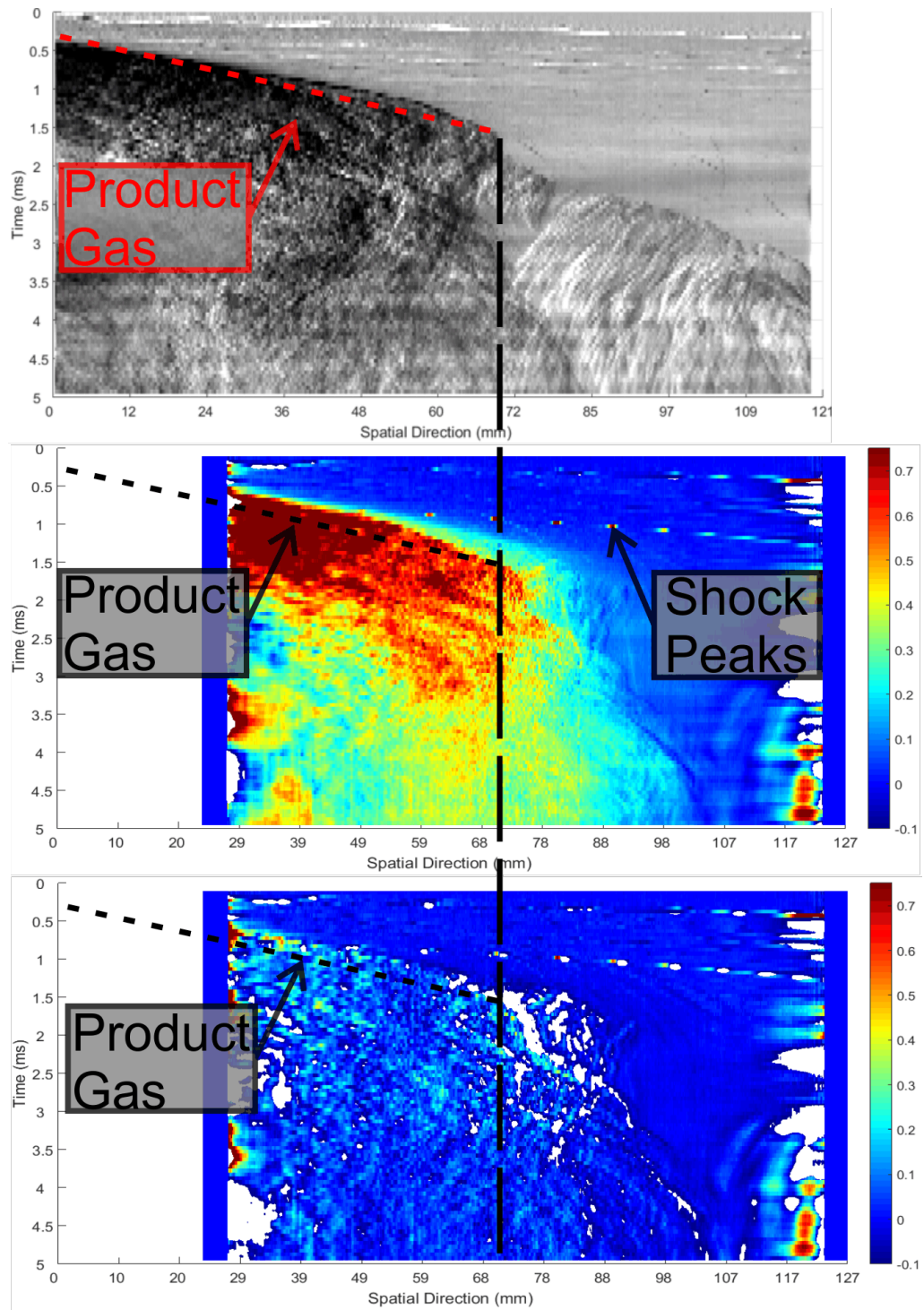


Figure 5.5: Top image is a schlieren imaging technique streak image. Middle image is the spectral streak image before the baseline shift. Bottom image is the spectral streak image after the baseline shift.

5.2 Iodine Gas Shock Wave Interaction

The effects of post shock wave turbulent mixing was tested. The iodine gas was injected with helium as previously shown in Figure 4.1. The helium-iodine gas plume was then perturbed with a shock wave created with a 209 shotgun primer. The same methods as a pure primer were used; the shotgun primer was fired after the ball valve was opened. This process was performed manually and timing of the event varied widely, no method was pursued to improve timing. The schlieren imaging technique camera recorded at 30,000 fps with an exposure of 0.29 ms. The spectral data was recorded at 30,000 fps with an exposure of 0.29 ms. These images were been down sampled to 15,000 fps for presentation purposes.

5.2.1 First Injection to Shock Wave Interaction

Test one and two did not capture the moment of helium injection. The timing of test three was such that the helium-iodine gas plume was captured from first injection through the shock wave interaction. Test three is presented first with the complete event streak image to describe first injection to shock interaction. The fluid motion inside of THOR is bounded by the top and bottom wall and this streak image set shows the complex nature of the flow.

Figure 5.6 summarizes the schlieren imaging technique and absorption imaging spectral response for test three in a streak image. The color map of the spectral streak image represents the relative concentration of iodine gas. Helium enters and fills the test section at 14 ms. Iodine gas enters and fills the test section at 15 ms. The iodine gas fills the test section and began to recirculate after reaching the top wall of THOR. This is shown as flow features out side the expected gas plume region. The recirculating helium gas mixed with iodine gas settling at the bottom of THOR at 200 ms causing an increase in the concentration of iodine. At 240 ms the shock wave and product gases enter the test section. Due to down sampling the effects of the shock wave is not visible as only one shock frame is present.

5.2.2 Full Field Analysis

During test one the plume is fully developed in the test chamber and the spectral response shows an even absorption profile along the the entire spatial axis. Data analysis used two methods, full field frame analysis and streak imaging to observe the fluid flow regimes. The frame analysis allowed fluid motion outside of the spectral window to be observed. The top image in Figure 5.7 shows

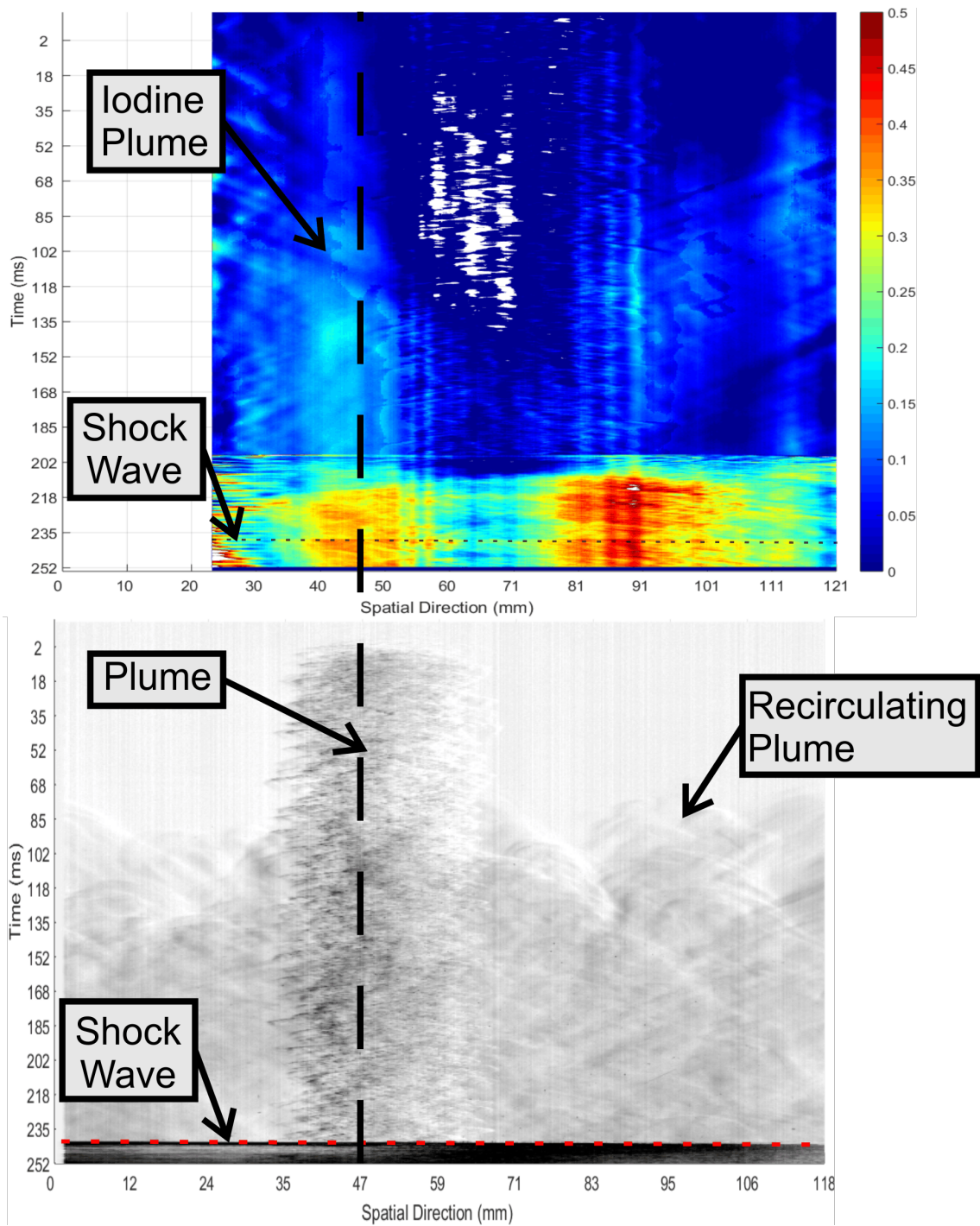


Figure 5.6: Top image is a streak image of relative concentration of iodine in test 3. Time progress from the top downward, the x axis is spatial. Bottom image is of a schlieren imaging technique streak image from test 3.

the shock wave from the 209 primer entering the test section . The shock is then observed in the middle of the helium-iodine gas plume in the lower image. The shock wave is visible for two frames before interacting with the gas plume. The shock wave velocity was calculated to be 475 m s^{-1} .

In Figure 5.8 the shock wave has crossed the original gas plume location. The leading shock wave is attenuated within the gas plume as seen in the lower image. The spectral response does not have a strong response to the shock wave. At 0.18 ms the product gases from the 209 primer are observed entering the test section.

The product gas front approaches the spectral window in Figure 5.9. During these frames the gas is moving at approximately 100 m s^{-1} . The spectral response has a limited change in absorption level.

In Figure 5.10 time has progressed by 0.54 ms till the product gasses begin effecting the spectral response. In the 24 to 36 mm range the absorption level begins to increase at 520 to 530 nm. The lower image at 0.90 ms shows the rise in absorption moving in the flow direction.

The next two frames capture a sharp increase in the absorption 520-530 nm value in the 24 to 36 nm region. The absorption peaks to 100 % in this region. The 48 to 83 mm spectral response is steady with few changes. Beyond 83 mm there is a region of lower absorption that approaches zero. These two peaks continue to flow down the test chamber in Figure 5.11. The high absorption region recovers 0.6 ms later. This peak is also seen in the 650 to 660 nm absorption level. The nature of this peak suggests it is a non physical since it arises quickly, within two frames, and returns to normal shortly. This maybe a reflected shock moving through the field of view.

5.3 Streak Image Analysis

The relative concentration for this test series is summarized in a streak image shown in Figure 5.13. Streak image processing was also applied to the schlieren imaging technique data set and is shown in Figure 5.13. The two images have similar features. At 0 ms the shock enters the test section, a slight increase in the absorption profile and a horizontal line in the schlieren imaging technique image. The shock travels through the test section and the gas products begin mixing. At approximately 4 ms the flow changes direction due to a reflected shock. At this point regions of high absorption are observed.

The same processing was applied to the second test. Similar features can be seen in the two streak images. Figure 5.14 summarizes the response for test

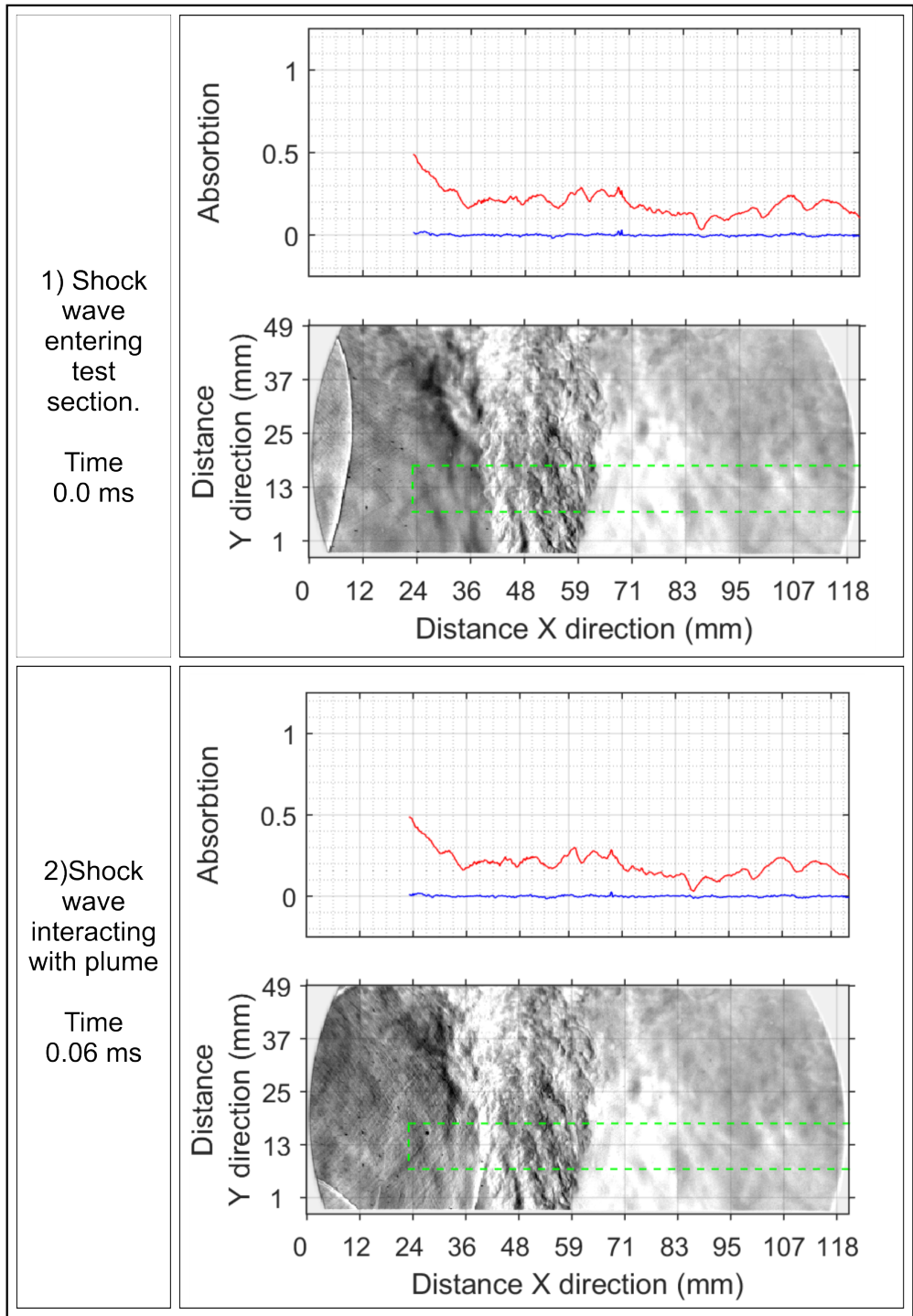


Figure 5.7: Peak wavelength average in red, off peak response in blue. Lower image is the schlieren imaging technique image.

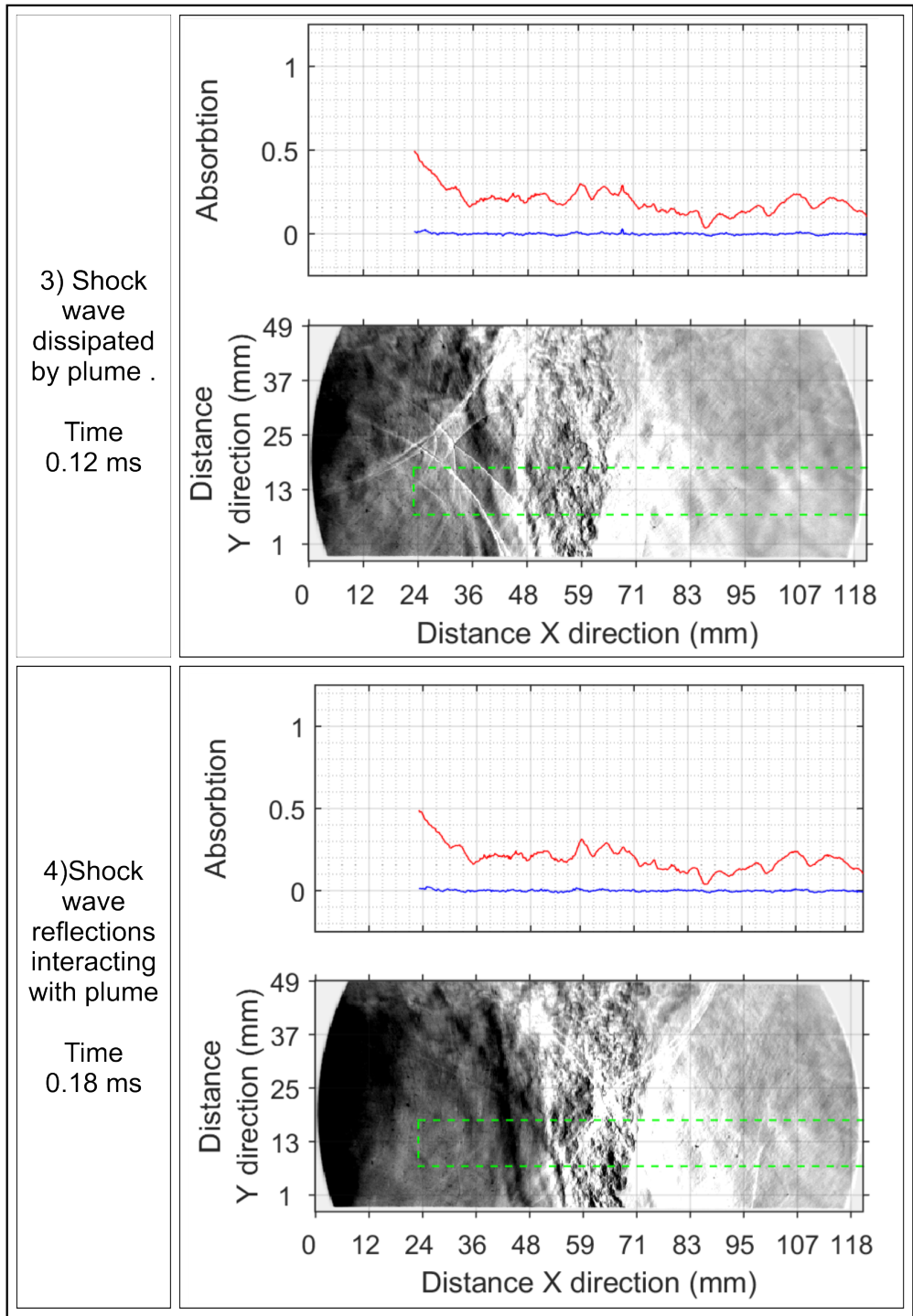


Figure 5.8: Peak wavelength average in red, off peak response in blue. Lower image is the schlieren image.

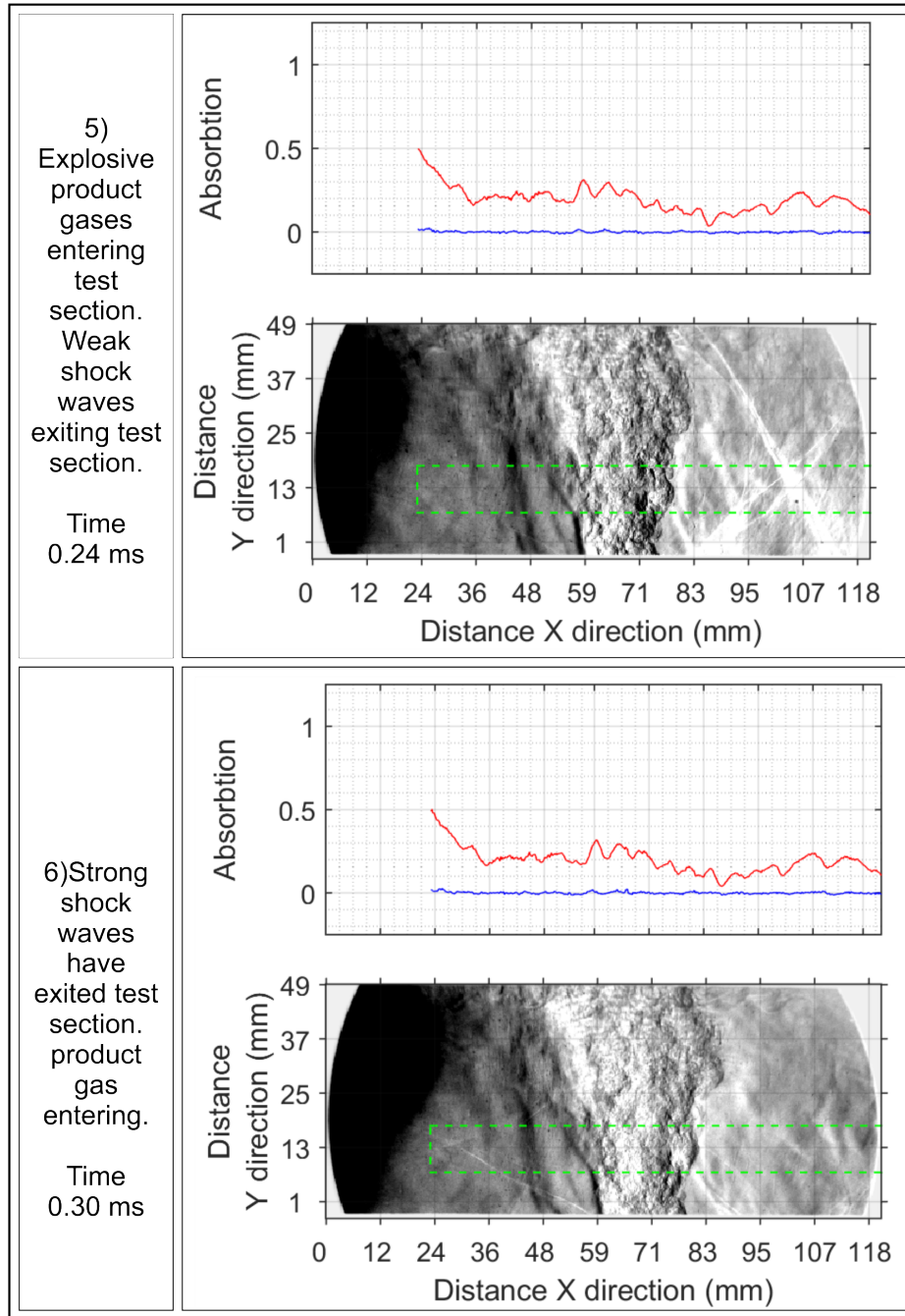


Figure 5.9: Peak wavelength average in red, off peak response in blue. Lower image is the schlieren imaging technique image.

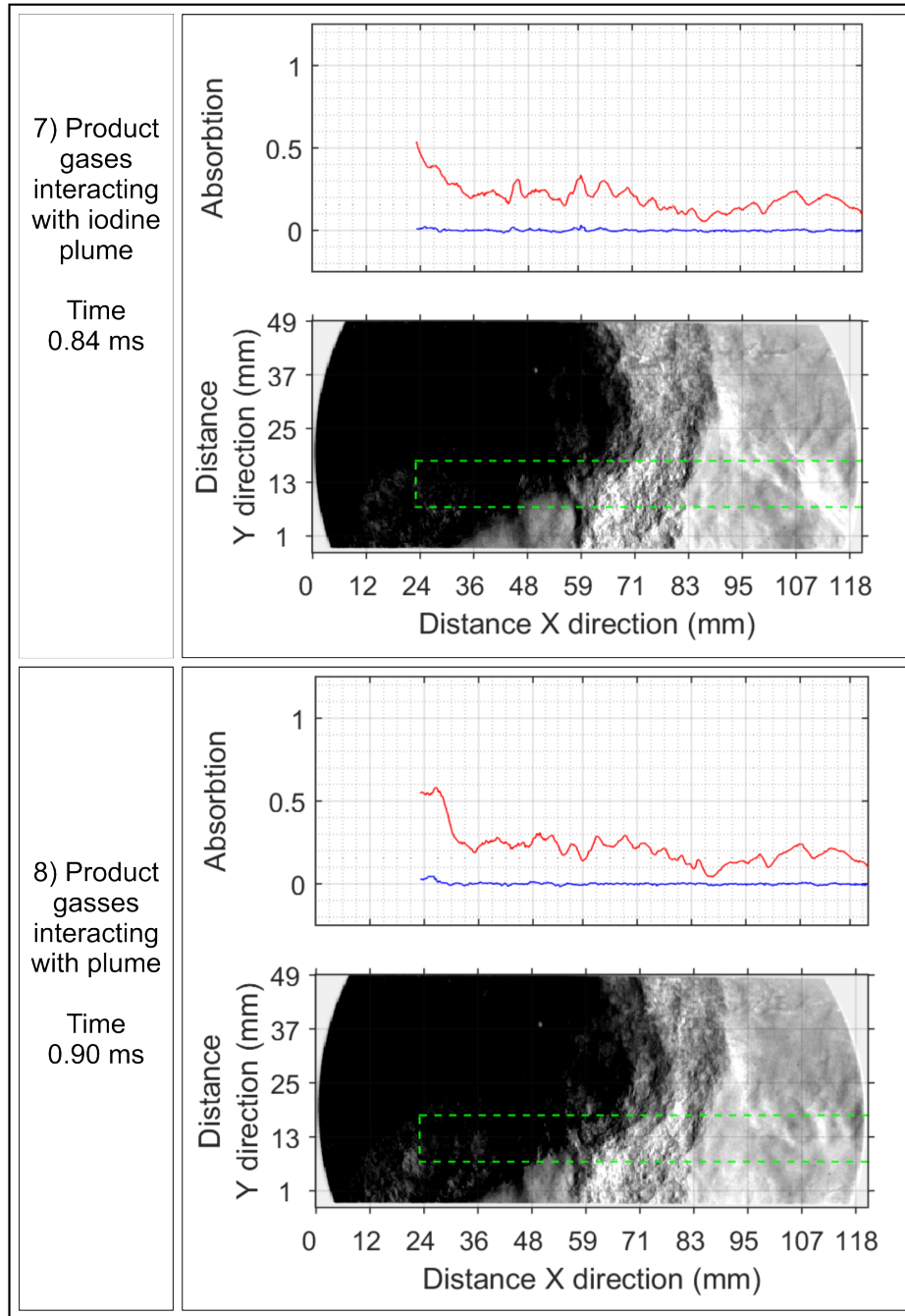


Figure 5.10: Peak wavelength average in red, off peak response in blue. Lower image is the schlieren imaging technique image.

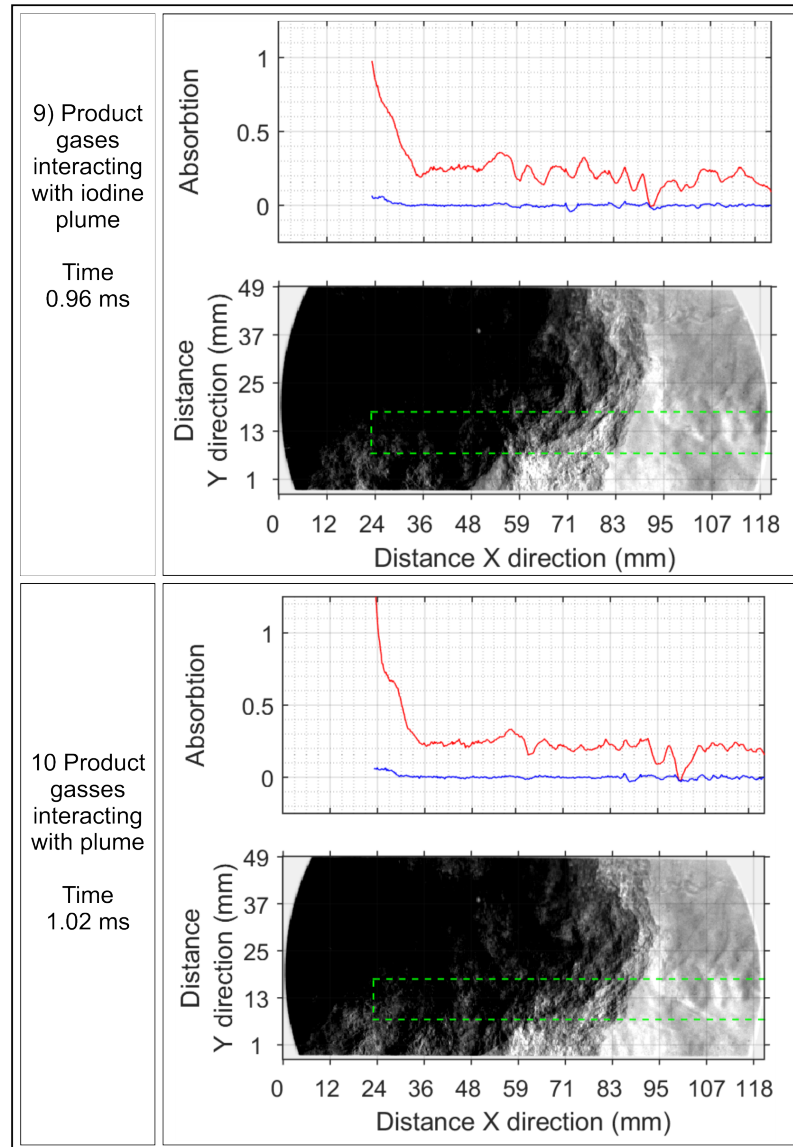


Figure 5.11: Peak wavelength average in red, off peak response in blue. Lower image is the schlieren imaging technique image.

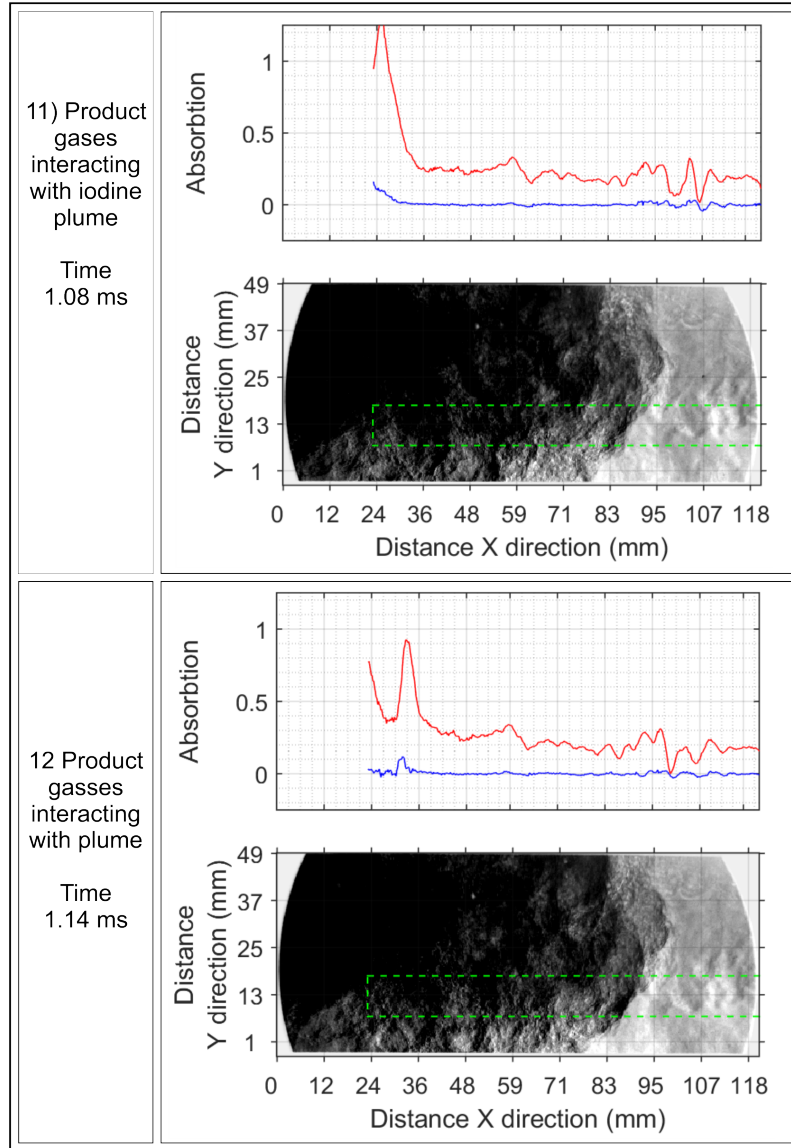


Figure 5.12: Peak wavelength average in red, off peak response in blue. Lower image is the schlieren imaging technique image.

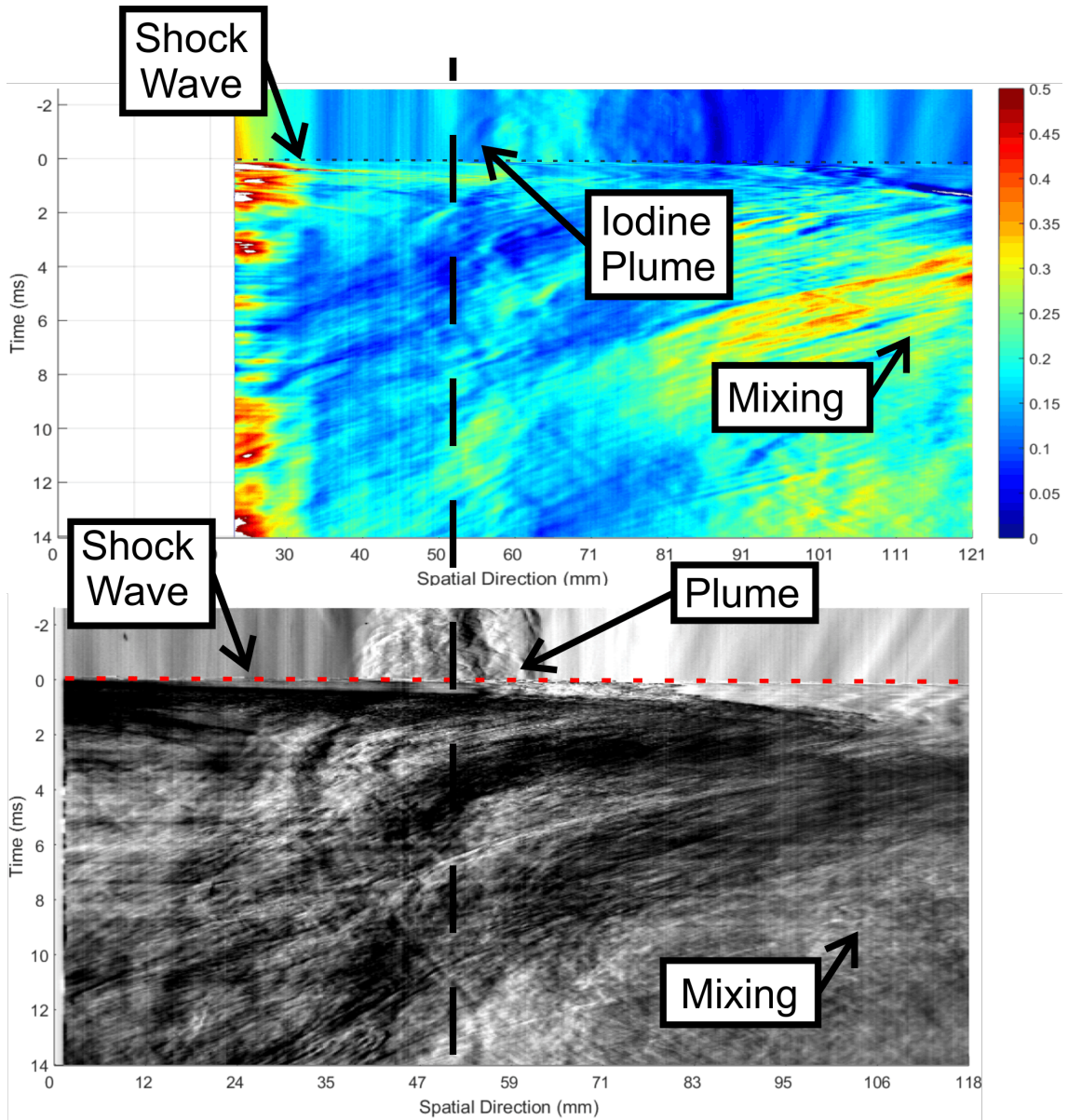


Figure 5.13: Streak image of the schlieren imaging technique data set and relative concentration of iodine gas for test 1. Time progresses from the top downward. The x axis is spatial for both data sets.

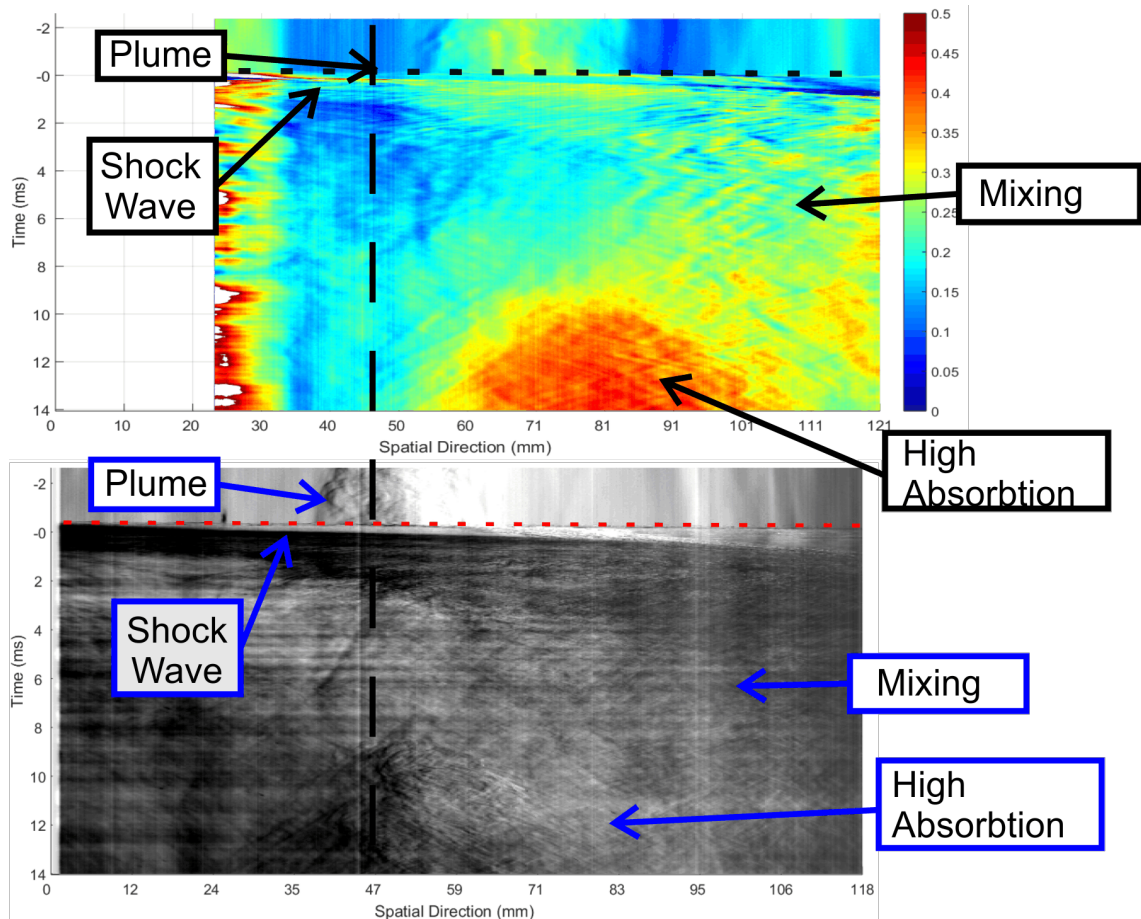


Figure 5.14: Streak image of the schlieren imaging technique data set and relative concentration of iodine for test 2. Time progresses from the top downward. The x axis is spatial for both data sets.

two. The shock enters at 0 ms and disrupts the plume. Down stream at the later time the concentration of iodine gas increases. At approximately 10 ms the gas plume is established in the center of the test section. Figure 5.14 summarizes the spectral response for test two. The shock enters the test section at 2.5 ms shown as a sharp line across both streak images. Explosive and helium-iodine gas products then fill the test section.

5.4 Conclusions

Simplified shock wave interaction with a helium-iodine gas plume tests were conducted. These tests demonstrated a background signal from large refractive index changes such as a shock wave. A baseline shift was applied and

background absorption signals were successfully removed. A primer was used to create a shock wave which interacted with a helium-iodine gas plume. Flow features such as a shock wave, reflected shock waves and turbulent mixing were observed. The shock wave pushed the helium-iodine gas plume downstream and then the explosive product gases mixed with the gas plume. This mixture introduced iodine gas that had fallen out of the spectral window. During test two there was a large region of higher absorption indicating higher concentration of iodine gas. The reflected shocks pushed some of the iodine gas back into the spectral viewing window.

CHAPTER 6

IODINE IDENTIFICATION WITH $Al-I_2O_5$ PRODUCT GASES IN TURBULENT POST BLAST FLOWS

The final step was to combine the shock wave source and iodine injection to one event. To accomplish this 500 mg of $Al-I_2O_5$ thermite was initiated with an RP-2 detonator. The testing goal was to combine the two sources to begin to characterize the post blast environment including turbulent mixing. Through this testing larger gas volumes and optical densities were noted. This testing also included the use of PCB pressure transducers for shock velocity measurements.

6.1 Test Methods

The $Al-I_2O_5$ thermite was mixed the day of testing at a ratio of 78.8% I_2O_5 and 21.2% Al by mass. The two powders were weighed and placed into a mixing container. This mixing container was placed on a rock tumbler for 30 minutes. The binary thermite mixture is shown in Figure 6.1 taken after mixing. A Teledyne RISI RP-2 detonator was secured into a Swagelock fitting that was attached to the mounting plate. The $Al-I_2O_5$ powder was poured into the Swagelock fitting. A laminate burst plate was placed over the open end of the fitting. The assembly was bolted together with the positioning block. The entire assembly was secured into THOR and four set bolts retain the assembly in a repeatable position. The detonator leads were fed through the back plate of THOR. The back plate was then attached to THOR with four 1/4-20 bolts. All equipment was operated remotely from a control bunker.

The schlieren imaging technique camera was operated at 30,000 fps with a 0.29 microsecond exposure. The imaging spectrometer was operated at 30,000 fps with a 5 microsecond exposure. The front entrance slit was set to a 5 μ m height and 8 mm spatial width.

6.2 Shock Velocity

The shock velocity was calculated for each test. In Table 6.1 the shock velocities are reported. The two methods agree with less than 10 % difference. Test



Figure 6.1: $Al-I_2O_5$ thermite powder used for testing.

Table 6.1: Shock velocity measurements

Test	Type of test	PCB shock velocity (m/s)	Optical shock velocity (m/s)
1	RP-2	461 ± 15	466 ± 10
2	Thermite	577 ± 20	557 ± 10
3	Thermite	599 ± 10	584 ± 10
4	Thermite	661 ± 10	611 ± 15
5	Thermite	695 ± 5	676 ± 15

one is a RP-2 detonator with no thermite. Test four had more fragments from the burst disk. This contributed to larger error in the optical velocity measurements since the shock wave was not clean. The velocities found with the PCB transducers should theoretically be slower than optical velocity since the shock wave is slowing down through the test section and the transducers are located 0.254 m apart. Several sources of error are possible including an error in the position of the transducer, signal noise, wall effects on the shock wave, and sampling rate of the oscilloscope. An exact cause of this error was not determined.

6.3 RP-2 Detonator with no thermite

A RP-2 detonator with no thermite charge was used to identify the background spectral signal and fluid flow features. The results of this testing are shown in Figure 6.2. The top image is the schlieren imaging technique streak image for 50 ms after the shock wave. The schlieren image shows several fluid flow interactions with the shock wave and reflected shock waves. To understand this

streak image a wave diagram was made showing the shock wave interactions. This wave diagram is shown in Figure 6.3. The background spectral signal of this testing is shown in the middle image of Figure 6.2. The background spectral signal was removed and the resulting signal is shown in the lower image.

6.4 RP-2 Detonator 500 mg of thermitite

6.4.1 Full Field Analysis

All tests were analyzed with through the full field. Test two will be presented here for analysis. The shock wave is shown in the middle of the test chamber +0.1 ms from the time it entered the test section in Figure 6.4. The spectral response is retarded by 11 mm to the location of the shock in the schlieren image. This error was from a camera synchronization error. During test three the shock wave position in the spectra data correlates well with the schlieren imaging technique data. There is a small calibration error in the spectra data since the spatial direction is not uniform in size. The baseline shift does not fully remove the shock wave from spectral data. The shock wave produced by the RP-2 detonator has a larger refractive index change than the shock from a 209 prime seen in Figure 5.1.

The explosive product gases then enter the test section following the shock wave. Two distinct gas regions can be identified in the product gases. The first of which enter the field of view at +0.26 ms, however the gases are located higher in the chamber than the spectral band. These gases have a velocity of approximately 375 m s^{-1} . The first traces of iodine are detected at +1.03 ms as shown in Figure 6.5. The test section is filled with gas and a dark region is observed above the spectral band. This first gas region is characterized by lower refractive index changes as seen in the schlieren imaging technique images.

During this test series a unexpected fluid motion was observed following the shock wave. Particles were observed entering the test section from the top and bottom of the field of view. These particles and gas appear to be from a leaking top and bottom window. Mounting and burst disk debris is also observed in the test section. These particles appear as regions of complete light absorption during the test.

The second gas region enters the test section at 1.53 ms. This gas region has a higher refractive index and absorbs light in the lower wavelengths. At +3 ms the darker gas region has travel the entire spatial distance as seen in Figure 6.6. This optically dense gas cloud persists in the test chamber till the end of the data sets. The upstream spatial absorption profile reaches full absorption 0.8 ms before the middle spatial profile. The 100 % absorption level continues till the end of the test suggesting that the optical windows became coated with iodine and the gases within the test section are iodine rich.

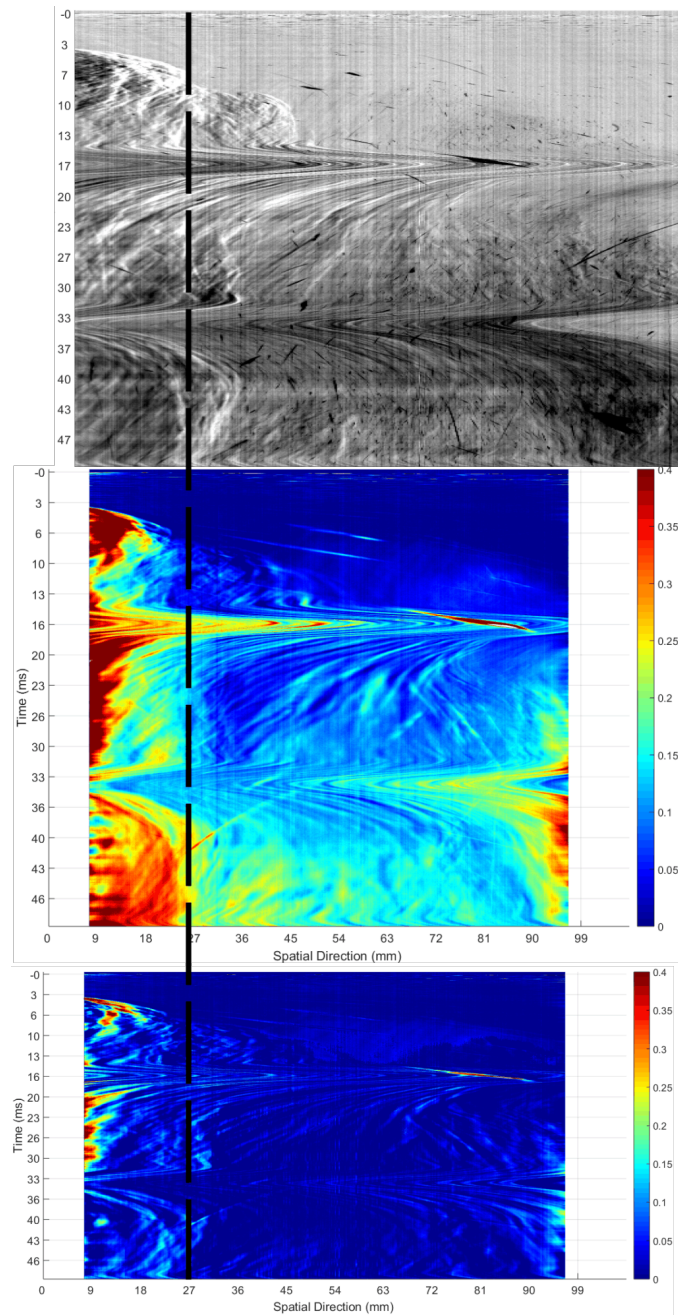


Figure 6.2: Top) Schlieren imaging technique streak image. Middle) Spectral background signal. Bottom) Spectral background signal after the baseline shift.

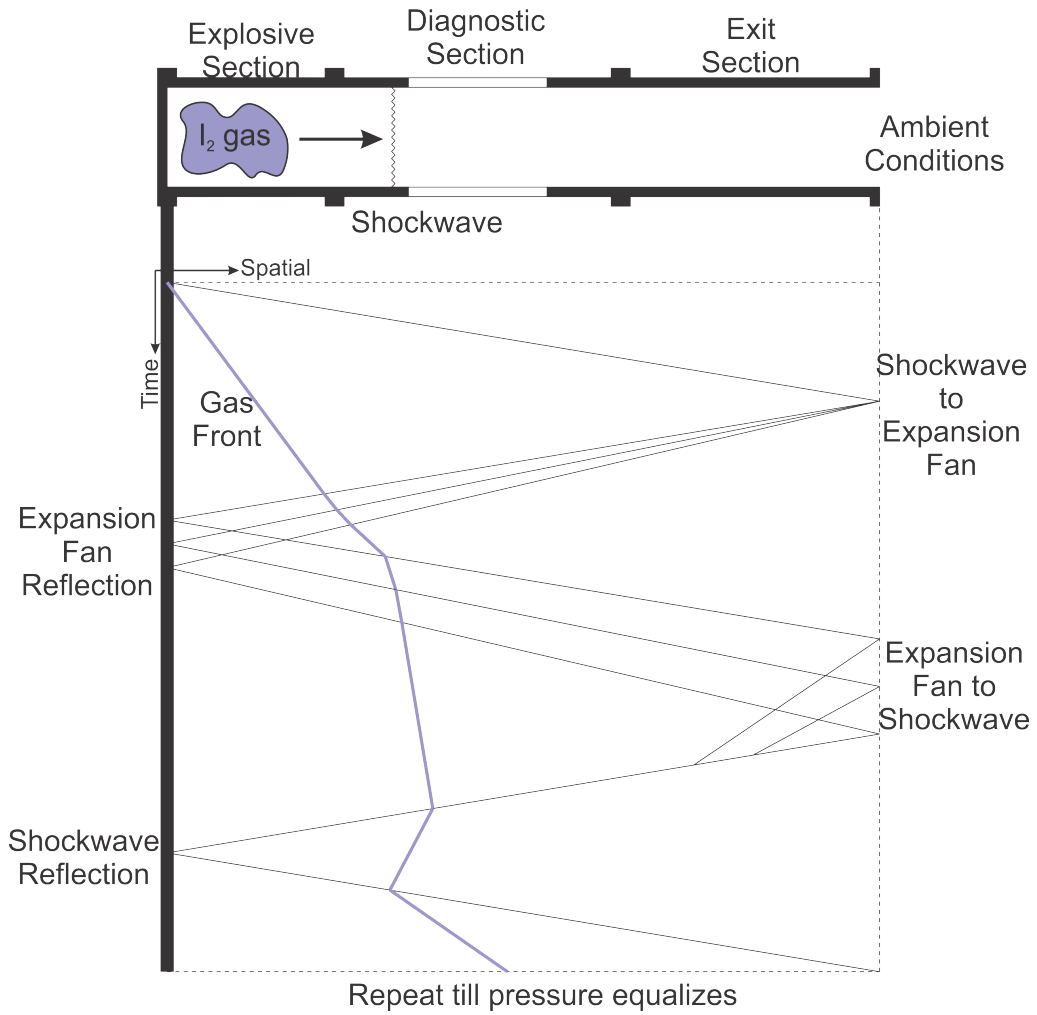


Figure 6.3: Wave diagram detailing the theoretical shock wave interactions in the shock tunnel

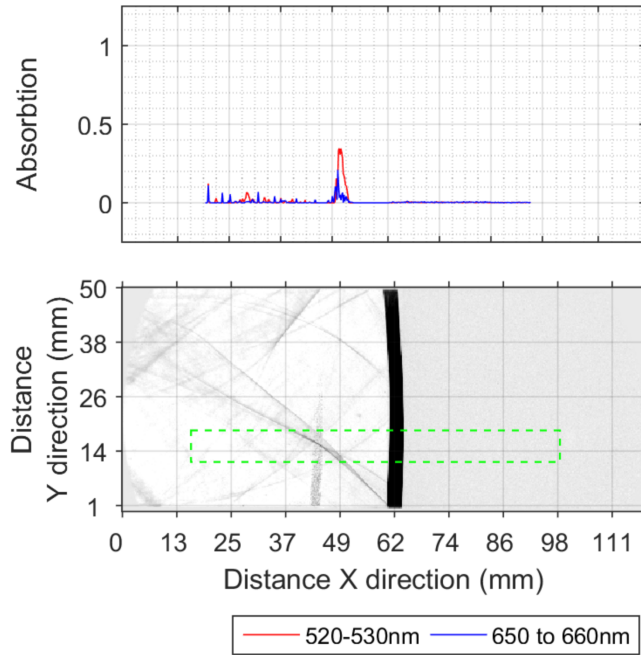


Figure 6.4: Frame three of test two showing the shock wave in the middle of the test chamber. Spectral response is retarded by 11 mm. This error is from camera synchronization.

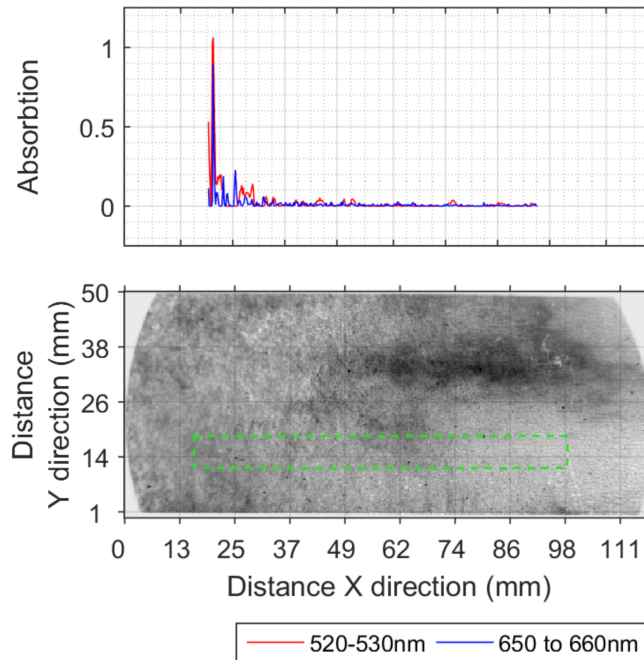


Figure 6.5: Start of iodine gas in test one

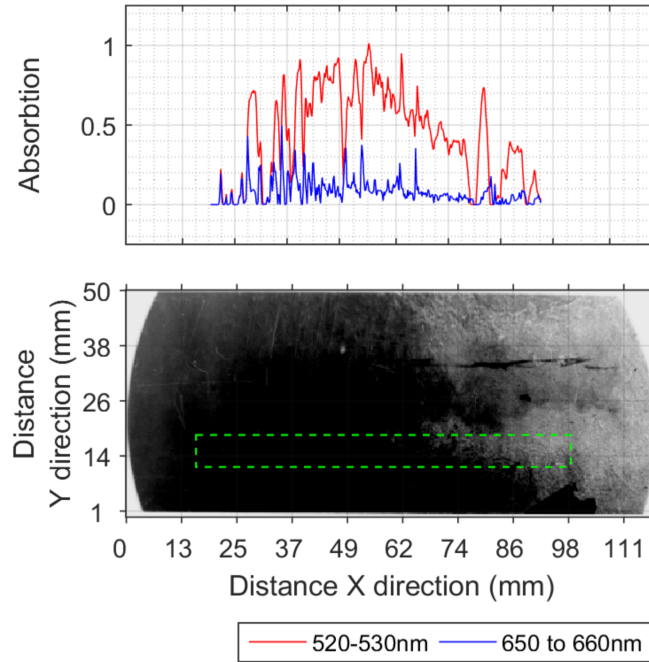


Figure 6.6: Test chamber filled with iodine.

The full field analysis shows an initial region of fast moving non absorbing gas products. This gas cloud is from the detonator explosive product gases and a small fraction of the $Al-I_2O_5$ thermite. The second region of gases has a characteristically higher absorption level in the 520 to 530 nm range. These gases are optically dense and the schlieren imaging technique images are blacked out. This suggests the $Al-I_2O_5$ thermite is not explosively detonating but burning and propagating through the test chamber. The spectrometer is able to still capture some fluid movement in this dense gas region. The amount of residual iodine on the windows is unknown during testing. This is a source of error for the spectroscopy data.

6.4.2 Streak Image Analysis

The tests are summarized in streak images. The first thermite test is shown in Figure 6.7. The shock wave enters the field of view at 0 ms. In the schlieren imaging technique streak image the shock wave appears as a dotted sloping line. Similar features are present in the spectral streak image. The iodine concentration begins to sharply increase at 1.53 ms and continues to fill the test section. The schlieren imaging technique streak image only shows the lead edge as the gas is absorbing most of the light. The gas rapidly decelerates in the test section at 5 ms

the gas contracts after a reflected shock wave passes through the test section.

Test three reached full absorption at upstream location early in the test. The resulting spectral image only has a narrow ridge where the data is meaningful. The streak images for this test are shown in Figure 6.8. During this test a piece of tape was used for better holding of the detonator. This piece of tape smeared the window around 1.25 ms resulting in loss of data at several points. In the schlieren imaging technique images the tape is observed entering the test section and hitting the window. As the tape travels down stream a residue is left on the window. The streak images show similar trends as test two. A time delayed high absorption in the 520 to 530 nm region cloud of gas enters the test section around 1.5 ms. This cloud decelerates and begins to reverse direction. The gas cloud mixes within the test section and concentrations vary spatially.

Test four featured the darkest gas cloud and the data is only meaningful in a few areas. The streak images for this test are shown in Figure 6.9. The spectral image only has a ridge of data. Late time during this test has complete absorption of the light. This could be from variations in the $Al-I_2O_5$ thermite as no optical changes were made.

A single column of data was extracted from the streak images. The schlieren imaging technique data was inverted such that a dark region was considered to have an intensity of one and a clear section is zero. This allows the spectra response to be directly compared to the schlieren imaging technique response. This processing was done for test two and three. Test four was dark and did not offer any meaningful data for this processing.

The vertical streak row image for test two is shown in Figure 6.10. The top image traces the response at 25 mm from the upstream edge of the schlieren imaging technique field of view. The schlieren imaging technique data features a shock wave at 0 mm shown as a sharp peak. The spectral response trails the schlieren imaging technique response. This shows the gas that immediately follows the shock wave is not iodine rich. The spectrometer shows a sharp peak to full absorption shortly before the schlieren image is completely black. Following this peak the spectrometer and schlieren imaging technique data sets trend towards full absorption of the light. The lower image in Figure 6.10 traces the response downstream at 81 mm from the upstream schlieren imaging technique field of view edge. This traces also features a shock wave in the schlieren data. The spectra data trails the schlieren response with a larger separation suggesting that the iodine front is slowing as it travels through the test chamber. The second test shows very similar trends as the first thermite test. The upstream image was taken from 28.5 mm and the downstream image was taken from 89 mm. These data set are shown in Figure 6.11.

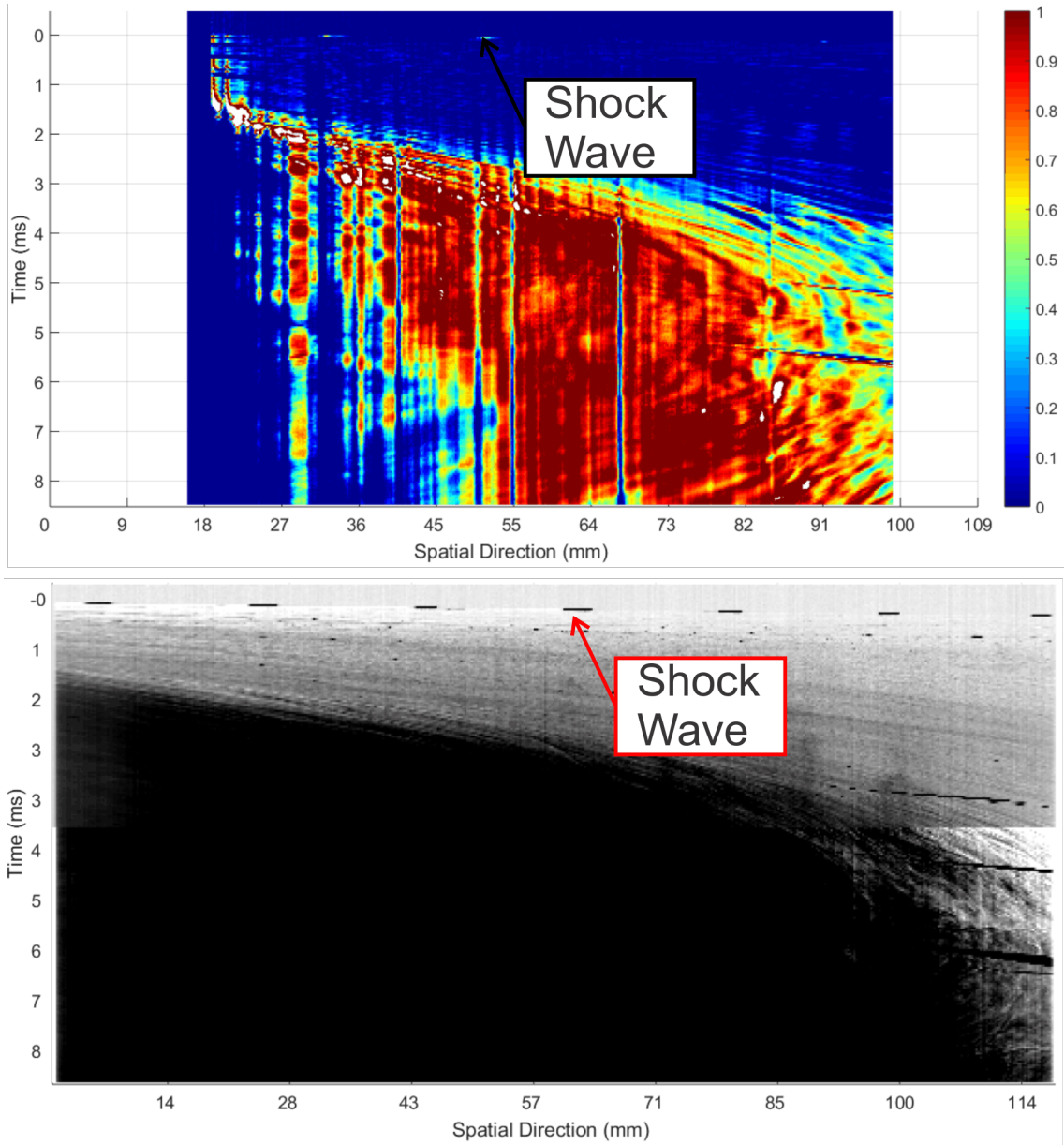


Figure 6.7: Streak images of the relative concentration of iodine during test two

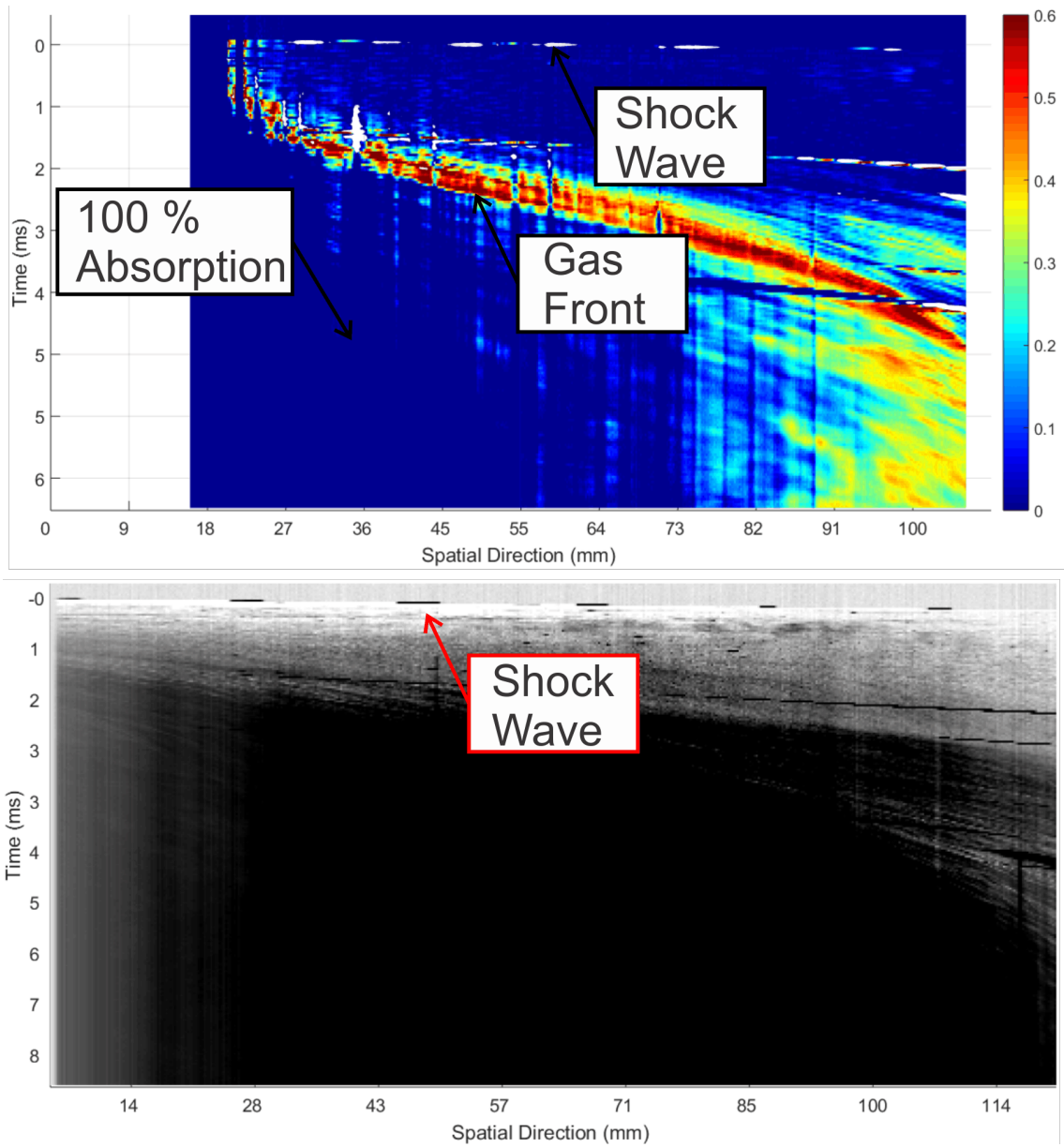


Figure 6.8: Streak images of the relative concentration of iodine during test three

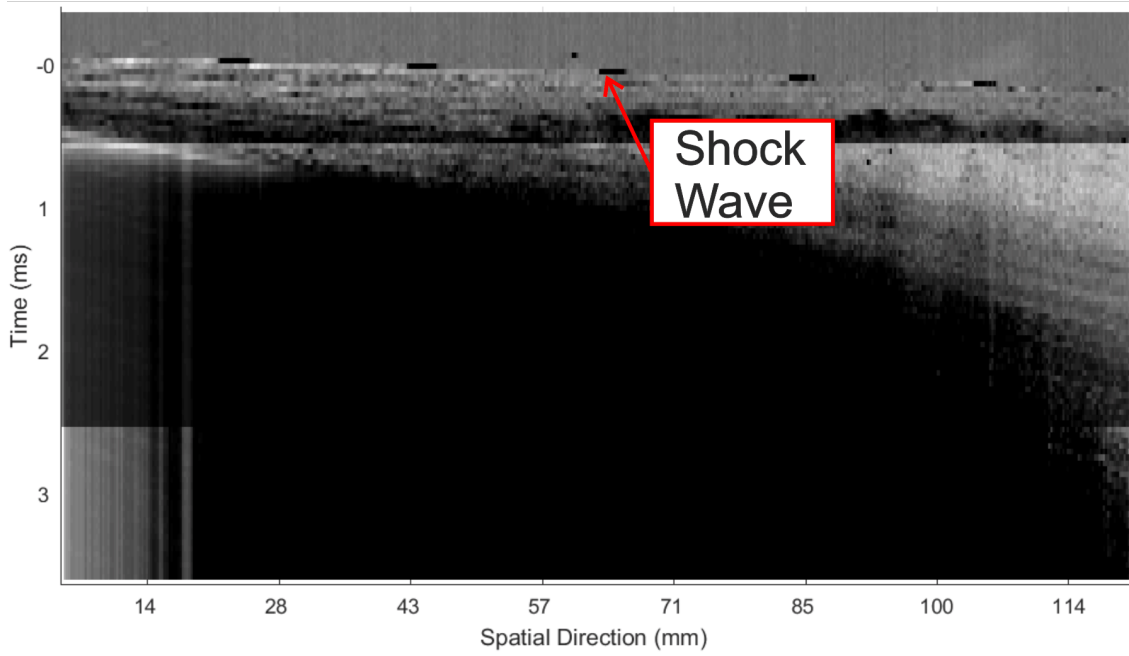
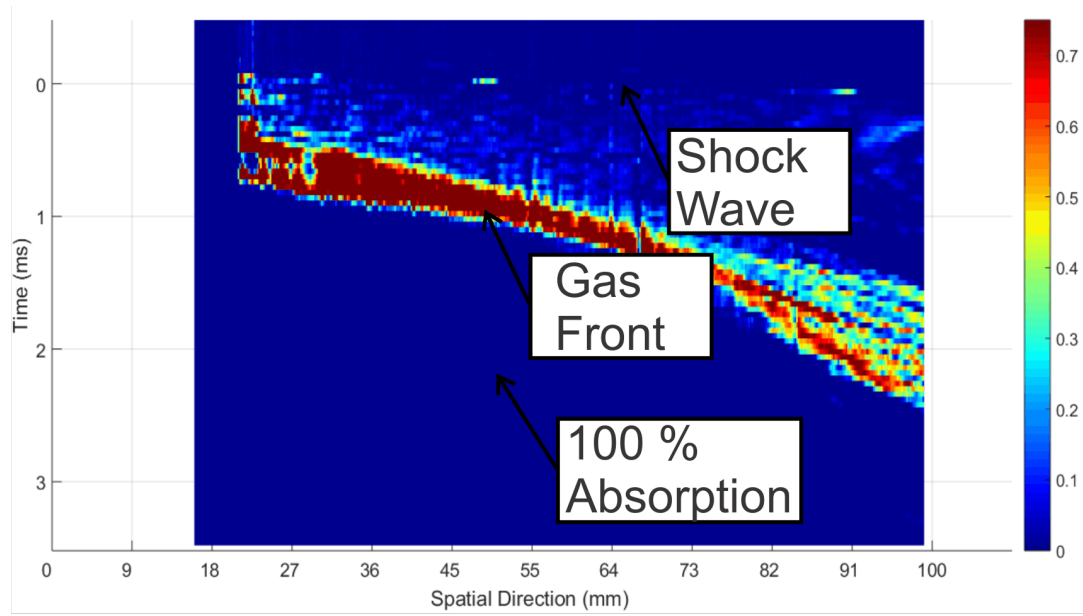
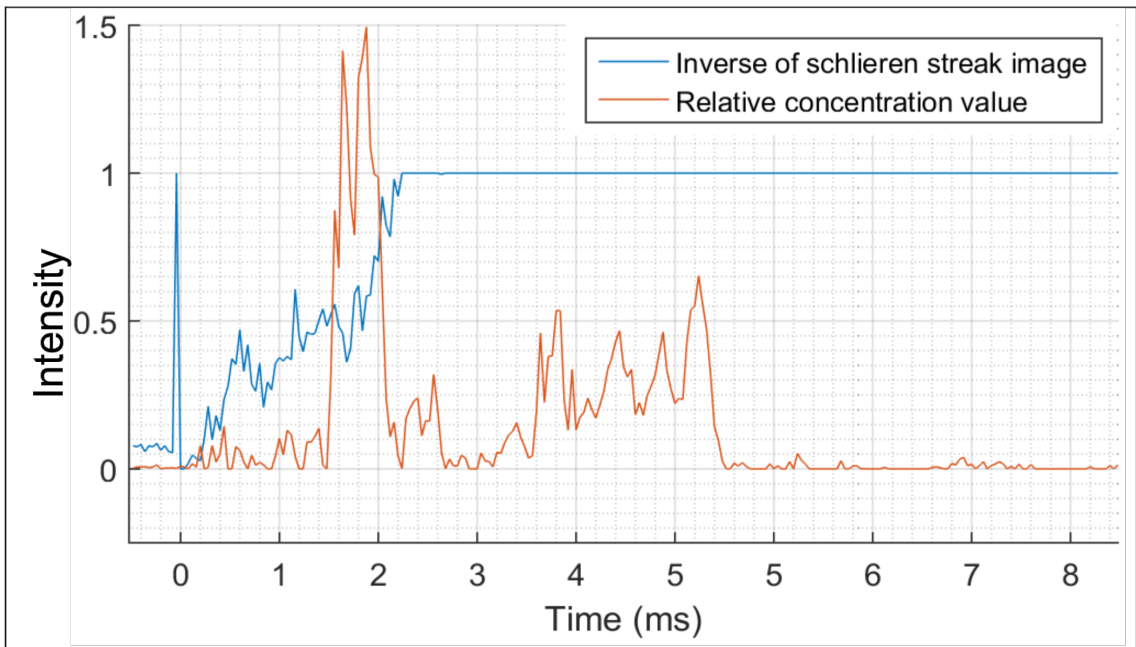
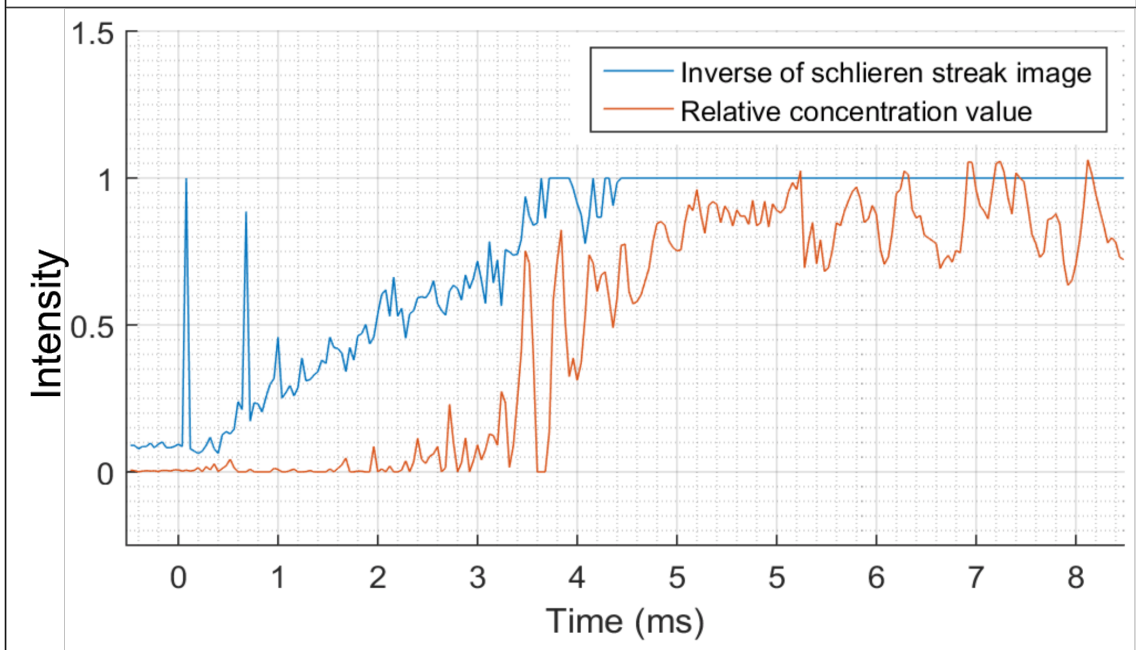


Figure 6.9: Streak images of the relative concentration of iodine during test four

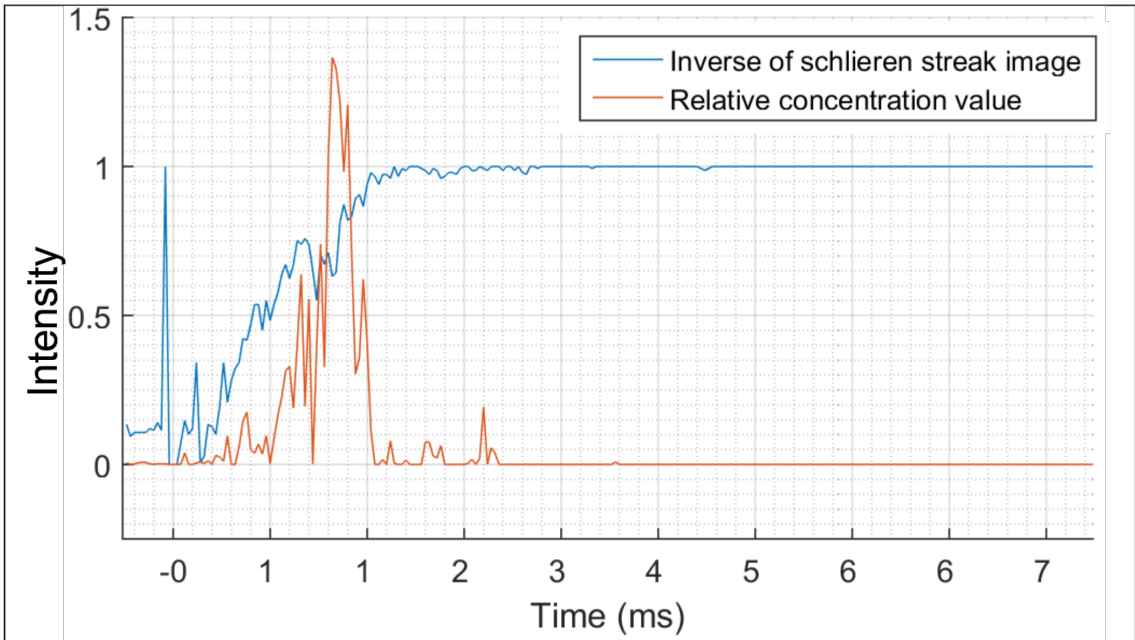


25 mm from upstream edge of schlieren field of view.

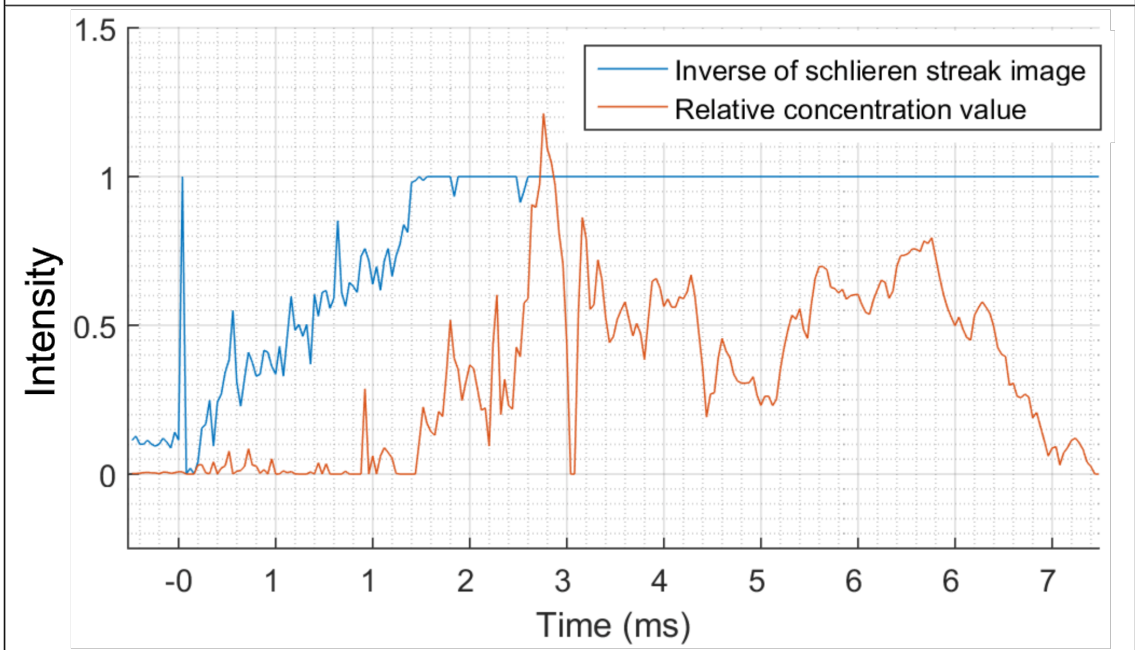


81 mm from upstream edge of schlieren field of view.

Figure 6.10: Vertical row from both schlieren imaging technique and absorption imaging spectroscopy streak images plotted at two distances from test two.



28.5 mm from upstream edge of schlieren field of view.



89 mm from upstream edge of schlieren field of view.

Figure 6.11: Vertical row from both schlieren imaging technique and absorption imaging spectroscopy streak images plotted at two distances from test three.

6.5 Conclusions

The final testing series combined the shock wave source and iodine injection. The RP-2 detonator created a strong shock wave which resulted in a stronger spectral response than the 209 shotgun primer. The addition of the thermite increased shock velocity and the optical density of the product gases. The spectroscopy data showed a dual gas front event with the first gas front having low concentrations of iodine gas and the second gas front having high concentrations of iodine.

CHAPTER 7

LARGE SCALE OPTICAL METHODS

Focusing schlieren optical systems were explored for the ability to perform large field of view imaging of refractive fields. The goal to evaluate these systems for the feasibility of making the same refractive imaging measurements in an expanding explosive environment in a free-field explosion. Several modifications to traditional focusing schlieren systems were explored here including laser-cut grids and a plenoptic camera. The laser cut grids offered an efficient method to produce scalable grids at low cost. These grids were limited to less than 0.5 lines per mm due to the nature of poster board and the tolerance of the laser cutter. A mixed system with laser cut source grids and a commercial Ronchi ruling as the cut off grid provided high sensitivity. A plenoptic camera was applied to the bench top system for a limited depth of focus sweep through the entire test region. This same focus sweep of the test section can be done with traditional methods, however, the plenoptic camera allows a single image to capture full field data.

7.1 System Quantification Targets

Two depth of field targets were designed to measure and demonstrate the concept of focusing schlieren. Focusing schlieren has the unique ability to limit the depth of field (DOF) or the amount of the optical path that is in focus. The traditional demonstration of depth of field is crossed jets located at different distances along the optical axis[28, 17]. Crossed jets do not demonstrate the exact depth of focus and the focus gradient since the jet is three dimensional. The two updated targets are shown in Figure 7.1. The first design is a glass ruler designed to be placed at a 45° angle to the optical axis. The ruler is used to measure both the depth of field and the height of the field of view. The ruler has tick marks every 2.828 mm in addition to three letters. When placed at 45° to the optical axis, the ruler denotes planes every 2 mm along the optical axis. The three letters (NMT) demonstrate the focus of the system similar to a common eye exam chart. The second target made from clear acrylic is a staircase design with planar spacing of 10 mm. Each measurement plane is perpendicular to the optical axis with this target.

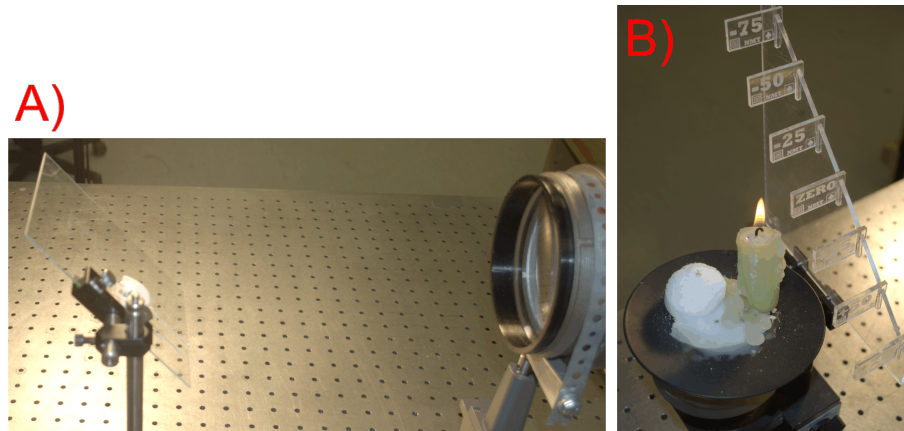


Figure 7.1: A) Glass ruler depth of field target. B) Staircase depth of field target.

7.2 Traditional Lens Schlieren

A traditional lens schlieren system was used as a reference system for comparisons of depth of field, ease of setup, and field of view. A single LED provides the point source of light for this system. Two 120 mm diameter, 700 mm focal length collimating lenses were selected for this system. The lenses were spaced 1000 mm apart. A Nikon 80-200 mm lens was mounted to a Nikon D5100 DSLR to capture the images. This camera's focal plane is at 50 mm from the first lens. The focusing target's zero plane was placed at the focal plane.

The results of the traditional system are shown in Figure 7.2. The full 80 mm range of the DOF target is in strong focus. The target's 45° placement is optically flattened. The three letters (NMT) are sharply focused and do not vary throughout the depth of the target. A soap bubble was placed in front of the target. The bubble's edge is sharp and clear. The interior features of the soap bubble are identifiable.

7.3 Traditional Focusing Schlieren

The most basic focusing schlieren is an in line system as shown in Figure 7.3. As described by Weinstein, the system's field of view is restricted by the size of the Fresnel lens, and the large format lens[27]. The light source is expanded and then refocused using the Fresnel lens. The source grid is placed in front of the Fresnel lens for uniform illumination. The region between the source grid and the large format camera lens is the test region. The large format camera lens collects and refocuses the light. The cutoff grid is placed in the plane where the source grid is refocused sharply. A relay lens is used to refocus the light to the

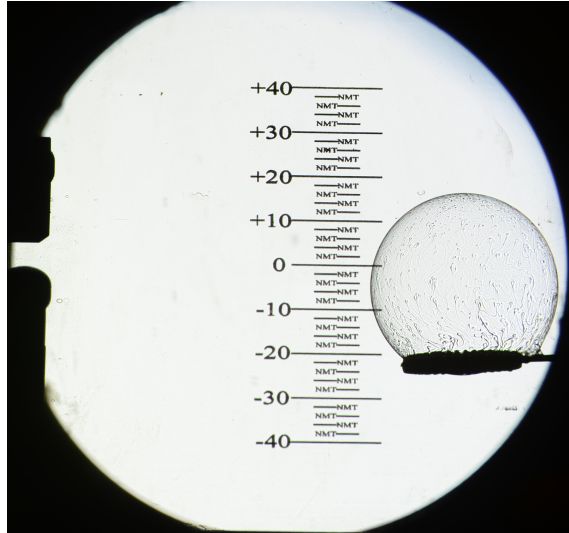


Figure 7.2: Traditional lens schlieren system with 80 mm field of view with a depth of focus greater than 80 mm.

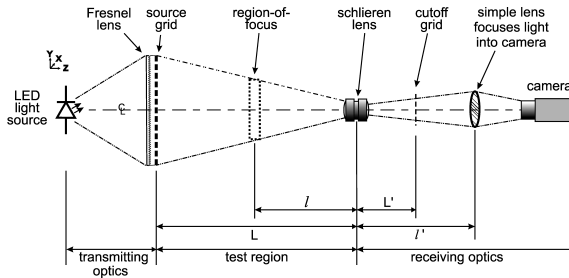


Figure 7.3: Traditional inline focusing schlieren system.

size of the camera lens. The relay lens is the focusing element for the camera.

Weinstein standardized the method to determine several key focusing parameters in the 1993 paper. Weinstein then updated and simplified these equations in 2010 [27, 33, 28]. The key formulas are reproduced here in Equations 7.1-7.5. The sensitivity of a focusing system is defined in equation 7.1. The value of L is the distance from the schlieren lens to the source grid, L' is the distance from schlieren lens to the cutoff grid, l is the distance from the center plane of the target to the schlieren lens. b is the distance between lines, assuming a 50 % cutoff $a = 1/2b$. All tested system designs have been tabulated in Table 7.1.

$$\epsilon_{min} = \frac{(20626aL)}{(L'(L - l))} \quad (7.1)$$

The size of the minimum resolution of detail is defined in Equation 7.2

[27]. λ is the wavelength of light and the magnification factor m equals l'/L' .

$$w = \frac{(2l' - L')\lambda}{(mb)} \quad (7.2)$$

The sharp focus depth is defined in Equation 7.3[27]. A is the aperture diameter.

$$DS = \frac{(2wl)}{(A)} \quad (7.3)$$

The unsharp focus depth is defined in Equation 7.4[27]. Weinstein chose that the minimum flow resolution w would be 2 mm.

$$DU = 2 * w * \frac{(l)}{(A)} \quad (7.4)$$

For best results the number of blended line pairs needs to be greater than 5 and greater than 8 is preferred[27]. The number of blended pairs is determined by Equation 7.5.

$$\phi = \frac{(An(l' - L'))}{(2l')} \quad (7.5)$$

7.4 Lens and grid Schlieren updates

7.4.1 Construction of Source and Cutoff Grids

Traditionally the source grid is photographically developed, silk screened, commercial product, or taped off by hand. The cutoff grid is either produced with photographic film methods or sized to fit a commercially available photo-etched Ronchi ruling[27]. These options are costly, difficult to employ, and limit the flexibility of the system. Laser cutting uses common materials such as paper and has a larger maximum size. Multiple panels can be joined to create a large source grid.

The modified systems developed here used source grids that were manufactured with NMT's VIS 6.60, 60 W laser cutter from Universal Laser Systems. Poster board was chosen for the cost and simplicity of laser cutting. The design for the grids were made in Solidworks. Laser cutting is an art form and little to no research has been performed at this scale on the optimization of system parameters. The current process for optimization is trial and error.

There are three cut settings to optimize: percent power, percent of speed, and the frequency of the laser module. When optimized a high tolerance cost effective grid is possible. A higher frequency transfers more energy to the paper, but allows for tighter tolerances. Universal laser describes laser frequency

as Pulses Per Inch (PPI). The speed and power were adjusted so that the paper is cut and removed without excessive heat and over penetration. The laser cutter kerf diameter or cut width was measured to be approximately 160 μm for this testing. The optical quality of the focusing lens, cutter settings, and the focus of the lens are factors in the kerf size. In addition the poster boards have varying thickness, material density, and flatness. Another problem is during laser cutting the material can become warped due to uneven heating of the material.

The effects of changing the speed of the laser cutter can be seen in Figure 7.4. The side nearest the focusing lens is shown in image A and the face that was the farthest away is shown in image B. The laser cutter cut is a tapered cut for two reasons, the beam size increasing when farther away from the focal point and the heat spreading in the material. In this figure a single pass of the laser cutter was repeated with varying the speed. The right line is the recommended settings of PPI of 500, speed 25 %, and power at 41.8 %. The middle line is a 40 % speed and the far left line is 50 % speed. The right line has burrs and the cut is incomplete. The left most line has crisper edges with less over penetration. Thinner materials will reduce three dimensional effects of the laser cutting process.

In Figure 7.4, image C, the grid is optically measured to determine the final cut size. As shown in the Figure 7.4, image C the optical edge of the grid is not crisp, an average of five measurements was used to determine the final cut width. The measurement was taken as the width of the solid line region. The 508 μm grid was measured at 662 μm , a 30 % error. The same process was repeated for the 1016 μm grid the final cut size was determined to be 1125 μm , an 11 % error.

The commercial Ronchi ruling was also examined and is shown in Figure 7.4, image D. The edges of the black strips are crisp and have a clear transition from clear to opaque. At this scale, a Ronchi ruling with the crisp edges is better for a cutoff grid.

A mixed system with a commercial Ronchi ruling as the cutoff grid and a laser cut source grid will provide the sharpest edges and the small line size. Errors in the source grid will be reduced by magnification of the system. An ideal minimum size of lines was not determined, more than 0.5 lines per mm is not possible with this laser cutting system and method. Changing to a rigid and clean cutting material cut with a system like Universal Laser's "High Power Density Focusing Optics" could dramatically increase this resolution and quality of edge.

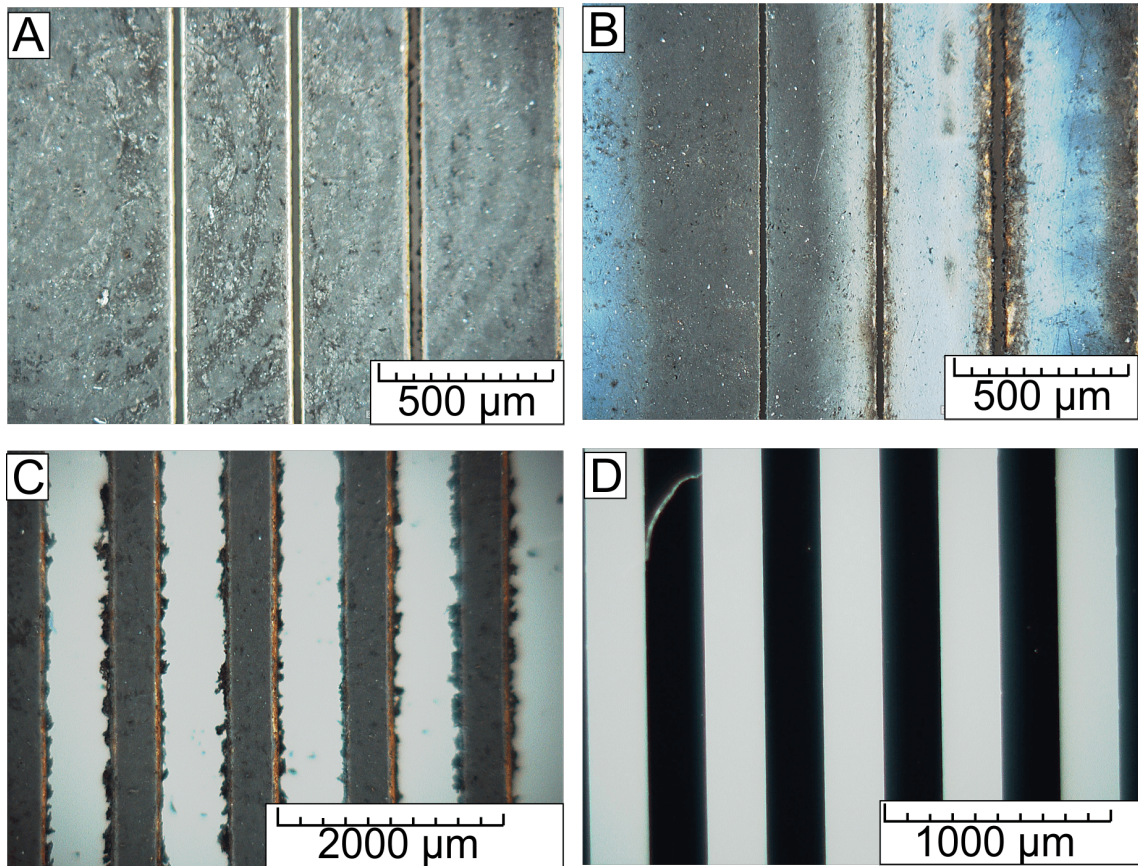


Figure 7.4: A) Front side of single line passes, B) Backside of single line passes, C) 508 micron grid, D) Commercially bought Ronchi ruling

7.4.2 LED illumination

The lens and grid schlieren system requires an extended light source. Traditionally, a point source has been expanded to an extended light source using a Fresnel lens. A light panel of 600 LEDs is used to form the extended light source. A diffuser is used to decrease the spot nature of the LEDs. The brightness of the LEDs can be tuned to match the system requirements. The LED light panel is limited by the power requirements, commercial lights are 1 meter square or less.

7.5 Modified focusing System

A modified system using laser cut grids was tested first. Figure 7.5, image A is the test section of the system. This system used a 0.492 lines per mm and a physical size of 203.4 by 203.4 mm ruling as a source grid and a 0.984 lines per mm, 101.6 by 101.6 mm cut off grid. The receiving optics, schlieren lens, cut off grid, simple lens, and camera are shown in 7.5, image B. The transmitting optics, light panel, diffuser, Fresnel lens and source grid are shown in Figure 7.5 C and D. The light source for this system was a Studio Pro 600 LED light panel. The Fresnel lens was mounted 500 mm in front of this light. The source grid was placed 40 mm in front of the lens. The large format lens was placed at 1250 mm from the source grid. The cutoff grid was placed at 340 mm from the large format lens. The relay lens was adjusted to bring the region of interest into focus.

The results of this system are shown in Figure 7.6. The traditional method of demonstrating depth of focus is shown in Figure 7.6 A. The right helium jet is placed at -10 mm and the left helium jet is placed at +10 mm with the middle of the focus plane at zero. Both jets are in good focus. Turbulent structures can be seen in the far field of the jet shown in Figure 7.6, image B. The staircase focusing target is shown in Figure 7.6, image C. A candle and soap bubble were placed at the zero plane. The bubble edges are strong and some internal features are present. The candle edges are visible, however the lack of sensitivity of this system limits the visibility of internal features of the plume. The individual planes created by the focusing target are compared to determine the approximate location of the focus, exact location and depth is difficult to determine with this target. The glass ruler exactly demonstrates the depth of focus as shown in Figure 7.6 image D. A soap bubble and candle are placed at the zero plane. The -2 mm plane through the +18 mm planes are in good focus. Similar results of the bubble and candle are present when compared to the staircase target.

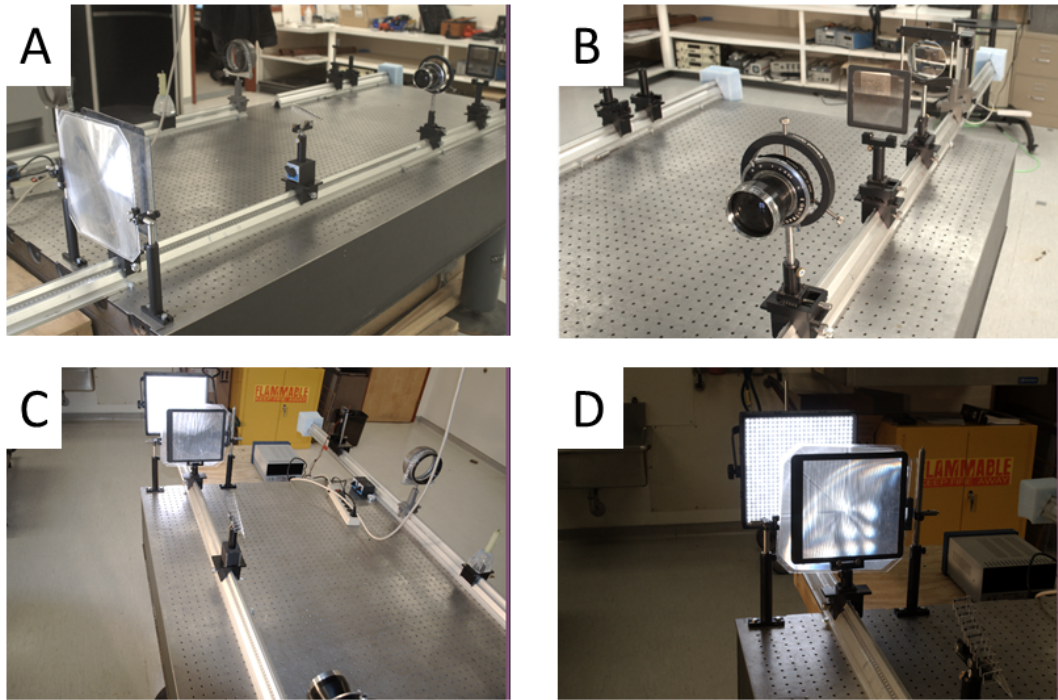


Figure 7.5: A) Test region from transmitting optics, B) Receiving optics, C) Test region from receiving optics, D) Source grid and light panel

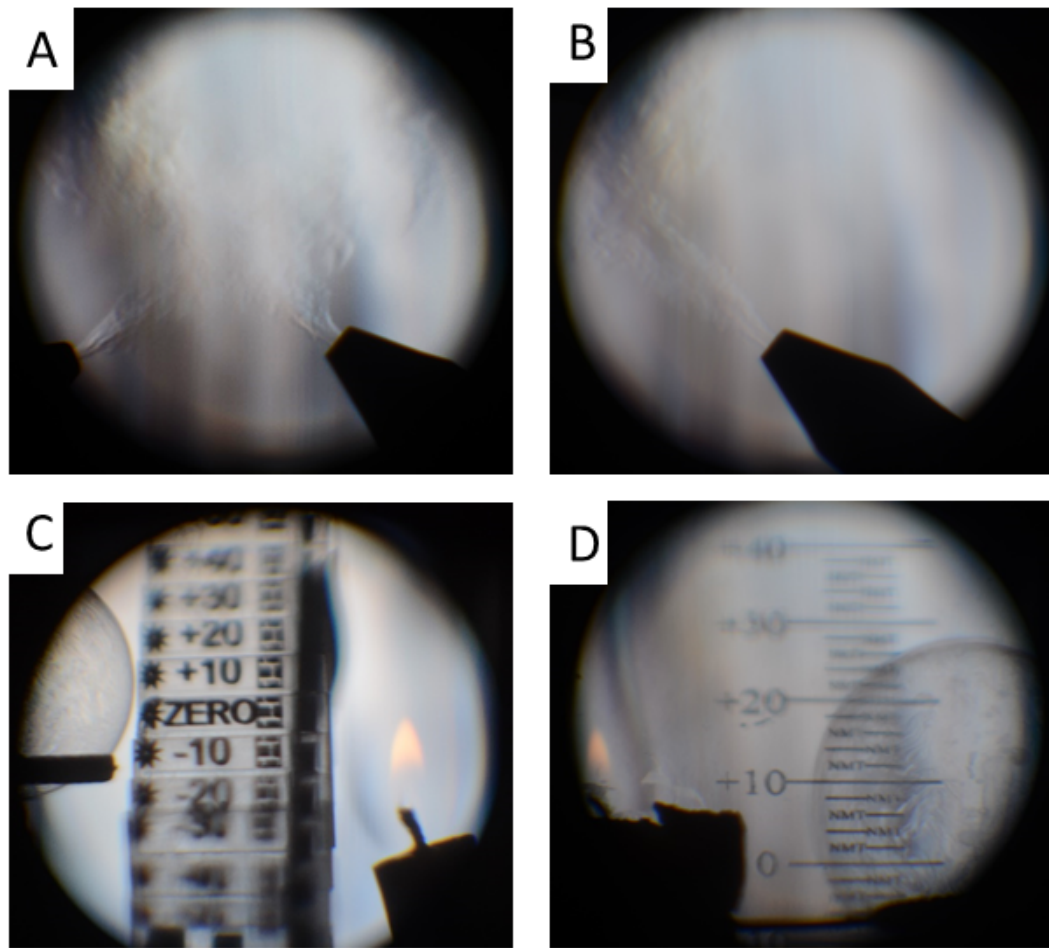


Figure 7.6: A) Crossed helium jets separated by 20 mm axially, B) A single helium jet, C) Staircase target with bubble and candle, D) Glass ruler with bubble and candle

7.6 Plenoptic Camera

A spherical soap bubble imaged with a traditional camera in a focusing system will produce images with slices of the sphere, and all slices can be captured if the focus plane of the camera is moved to sweep the DoF through the sphere. The plenoptic camera can improve this process by taking a single exposure of the test region and then digitally refocus or move the focus plane of the image. Recent advances with three dimensional reconstruction techniques have made plenoptic cameras available for lab-scale experiments[34, 35, 36]. The LYTRO camera is a hand held plenoptic camera which records the full 4D light field of the image[34].

The plenoptic camera is a traditional camera with a micro lens array placed between the camera lens elements and the digital sensor. Each micro lens covers a smaller array of photo sensors thus the micro lenses captures a tiny sharp image of the lens aperture. Through digital image processing the images are combined and a final image is produced with a depth map of objects within the image[34]. Through ray tracing, the details of where the light originated can be determined. The simplest use of this light field is to digitally refocus the image or expand the DOF of the image.

Thurrow, Fahringer, and Lynch have pioneered the use of these cameras with particle image velocimetry[36, 37]. For this work a new plenoptic camera and algorithm had to be developed. The process that Ren Ng developed for LYTRO fails when focusing schlieren adds the complexity of individual image planes within the test section[34]. However, since the LYTRO camera is designed for traditional reflective objects digitally refocusing through a transparent object can not be accomplished in this manner.

The focusing schlieren image of the soap bubble with a plenoptic camera allows will capture a image with a larger DoF that can be reduced digitally and the focus plane can be moved along the optical axis. In addition the plenoptic camera can be used to determine the size of the bubble and a relative location of the bubble.

The LYTRO camera image is shown in Figure 7.7. In image A all planes are in focus. In images B through D the depth of focus has been reduced and then swept through the test region. All four images were made from the same image with no changes to the optical setup of the system. The soap bubble is clear in images A and C and blurry in B and D. The LYTRO camera's limits are clearly seen in these images. The algorithm determines a depth plane based on sharp edges which schlieren features do not have. The camera's resolution of 1 megapixel also limits the resolution of these images.

A similar image sequence using a standard camera was also made. A new image is captured for each plane and optical components are adjusted for each

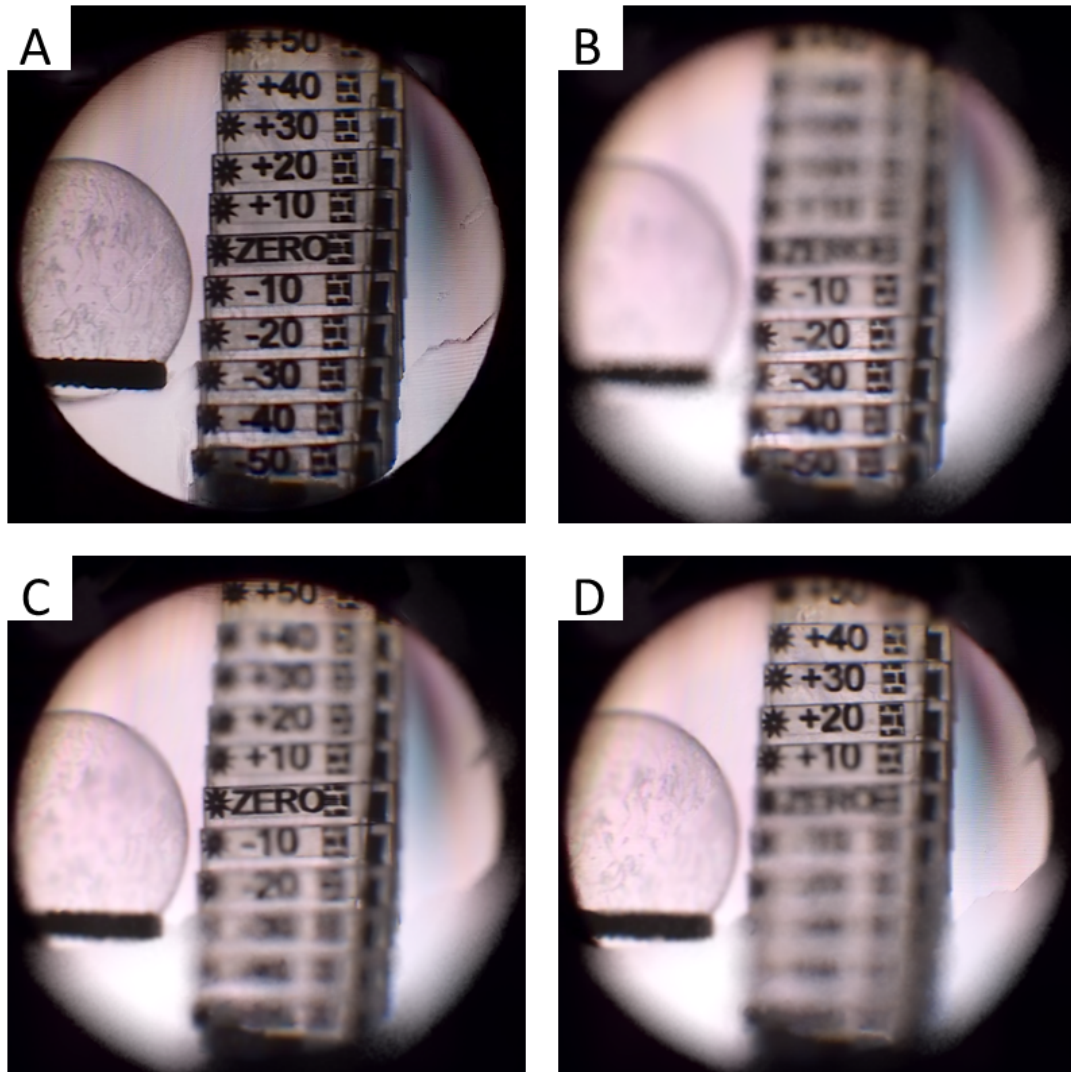


Figure 7.7: A) Original image with full depth of focus, B) Limited depth of focus around -35 mm, C) Limited depth of focus around zero, D) Limited depth of focus around +30 mm

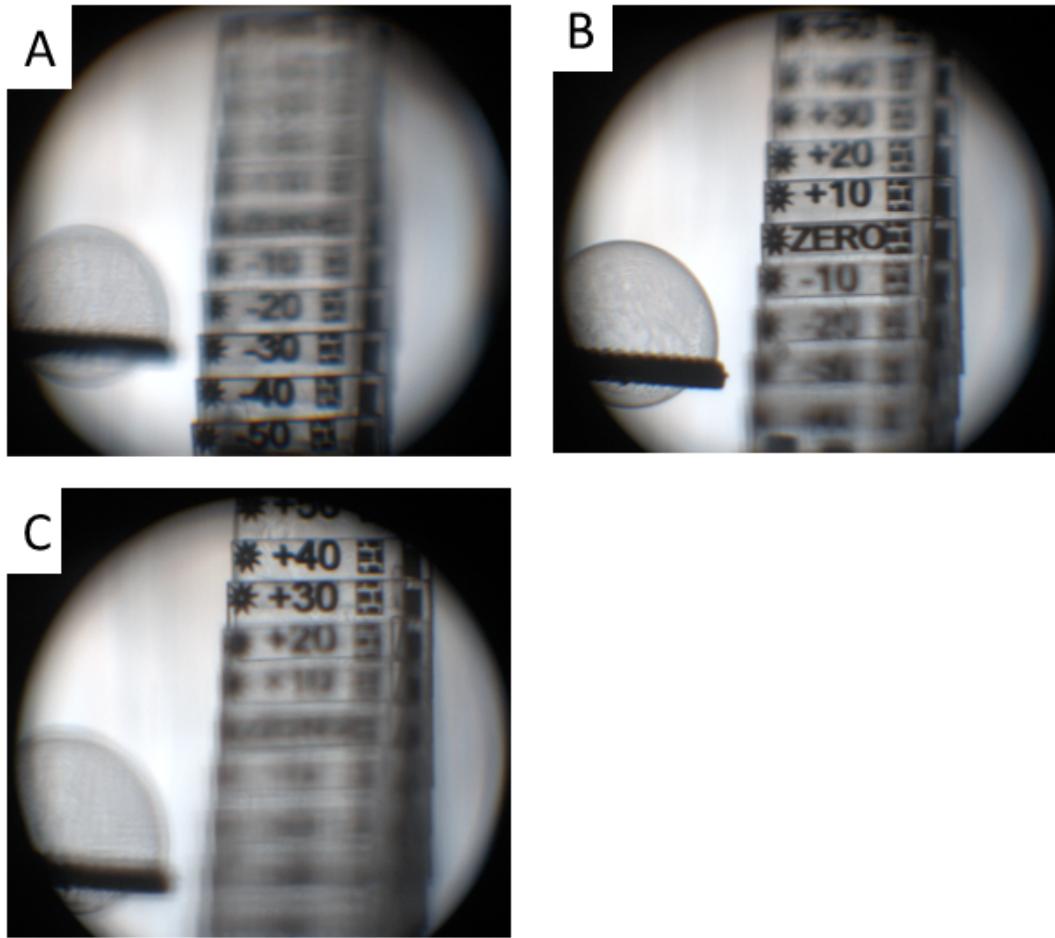


Figure 7.8: A) Nikon focused around -40 mm, C) Nikon focused around +5 mm, D) Nikon focused around +40 mm

plane of focus. Figure 7.8 is a series of images taken with a standard Nikon camera. The focus starts at -40 mm in Figure 7.8 image A. The collector lens is then moved to focus on to the zero plane in Figure 7.8 image B. In this image the bubble is in strong focus and interior details can be observed. The collector lens is then moved again to focus on +40 mm for Figure 7.8 image C.

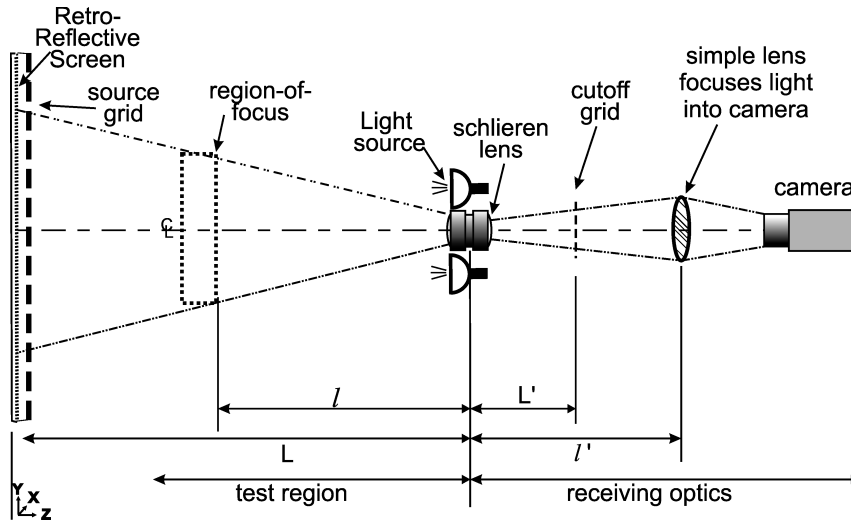


Figure 7.9: Traditional large field focusing schlieren system

7.7 Large Field Schlieren System

7.7.1 Traditional System Theory

For larger field of views a retro-reflective large field system is required. For this system the illumination source is moved such that it is projected, the light source is located next to the large format lens. The two limitations for this system are the illumination of the screen and the mounting of the screen. Figure 7.9 is a basic diagram of this system.

The light projects to the source grid which is attached to a retro-reflective material. The light is then reflected back to the large format lens. The region between the large format lens and the screen is the test region. The receiving optics are the exact same as the inline system. The large format lens collects the light and refocuses it to a plane where the source grid is in sharp focus. The cut off grid is placed at this location and aligned to the source grid. The size of the refocused test area plane is larger than the camera lens frontal area and has to be reduced or clipping of the image will occur. A simple lens or a Fresnel lens is used to collect and condense the light to the size of the camera lens.

7.7.2 System updated Design

Two changes were made to the retro-reflective large field schlieren system. First was on optical axis illumination a technique borrowed from Retro-reflective

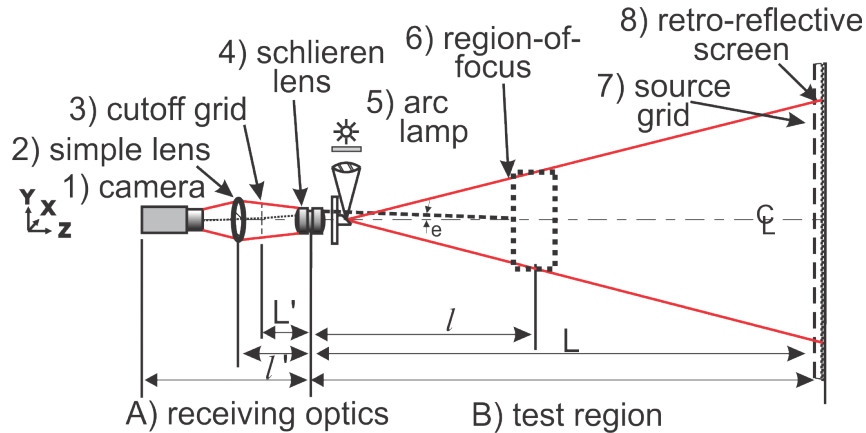


Figure 7.10: Modified large field focusing schlieren system

shadowgraph. Settles describes a technique to focus a 1000 W ozone-free xenon arc lamp on to a “rod mirror” which is glued to a camera filter [38]. This provides the ideal illumination when using a retro- reflective screen. A slight modification of mounting the “rod mirror” to a glass plane was made. This allows for the large format lens to be independent of the light source. Secondly the source and cut-off grid were produced using a laser cutter. The grids were made from common poster board cut to the required size. This simple change is illustrated in Figure 7.10

A single large focusing schlieren system was constructed for laboratory-scale testing, with a total length of 8 m with a 0.88 m wide by 0.66 m tall source grid. Figure 7.11 is a panoramic view of the entire system, the receiving optics are located on the left with the retro-reflective screen on the far right. A 3.937 lines per mm, 50 by 50 mm Ronchi ruling was used as a cut off grid. The system magnification was measured at 17.72. The source grid was made from two panels of 457.2 by 508 mm with a 0.22 grids per mm. The two panels were joined together with double sided tape. All the receiving optics and light source were mounted to an optical breadboard. This allows the whole system of light, large format lens, cutoff grid, collector lens and camera to be moved as one unit. This is ideal for transportation and alignment of the system. A rod mirror is glued to a 150 by 150 mm piece of glass. The arc lamp is mounted perpendicular to the optical axis and focused on to the rod mirror. The rod mirror is in collinear with the optical axis. A 300 mm focal length large format lens is the schlieren lens. A Photron Mini UX100 camera with a 80 to 200 mm focal length lens recorded the testing.

Table 7.1: System design specifications

System	A (mm)	f (mm)	L (mm)	l (mm)	L'(mm)	l (mm)	a (mm)	b (mm)
Modified	53.33	300	1250	625	340	400	0.49	0.98
Large Scale	53.33	300	6920	1120	200	440	0.254	0.51

Table 7.2: System Parameters

System	Field of view (mm)	Sensitivity arcsec	DS (mm)	DU (mm)	w	ϕ
Modified		59.7	4.05	46.88	0.172	6.78
Large Scale	150	31.25	1.17	84.01	0.027	14.31



Figure 7.11: Panoramic view of the NMIMT large scale focusing system

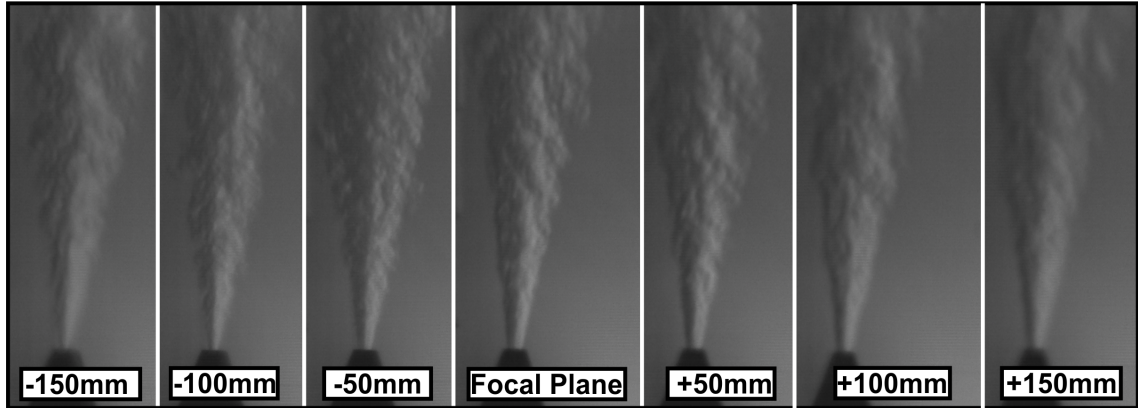


Figure 7.12: Single helium jet moved from -150 mm behind the focal plane to 150 mm in front of the focal plane.

7.7.3 System Results

A single jet was moved along the optical axis from -150 mm to +150 mm from the focal point at 5800 mm from the source grid. This series of images is shown in Figure 7.12. At the focal plan the field of view is 150 mm tall, 175 mm wide. The tip of the jet is 3 mm. At the focal plane flow features are sharp and distinguishable. Moving to 50 and 150 mm the flow features are blurred. At 150 mm features begin to blend into the back ground. A second test with crossed jets was performed to determine depth of focus. The right jet is held stationary at the focal plane. The left jet is moved along the optical axis towards the source grid. The results are shown in Figure 7.13. At 50 mm Figure 7.13 A both jets are visible and flow details are crisp. When the left jet is moved to 300 mm Figure 7.13 B, the left jet structures are weakly defined.

7.8 Conclusions

Shadowgraph and BOS do not offer the resolution and sensitivity needed to for this research. The internal gas dynamics within the detonation event are of key interest. Focusing schlieren excels in this region and offers a method to move to large scale testing with this research. The system is improved with using laser cut grids since setup time and flexibility was expanded. Laser cutting offers a method to create large source grids. However, small source grids made from paper products have too large of a tolerance to be effective cutoff grids. A mixed system such as the large scale system presented here offers the best of grid options currently available. The plenoptic camera process demonstrated with the LYTRO camera makes focusing schlieren even more appropriate for this research. The limitations of the LYTRO camera's software are currently being over come

A) 50 mm separation

B) 300 mm separation



Figure 7.13: A) Crossed helium jets separated by 50 mm on the optical axis, B) Crossed helium jets separated by 300 mm on the optical axis

by Thurow and others. The limited focusing sweep demonstrated here shows promise of allowing post recording manipulation of the schlieren data.

CHAPTER 8

CONCLUSIONS AND FUTURE RESEARCH RECOMMENDATIONS

8.1 Conclusions

Post detonation turbulent mixing was investigated with common path schlieren imaging technique and absorption imaging spectroscopy. The schlieren imaging technique provided insight into the nature of the mixing and absorption imaging spectroscopy was used to identify regions of iodine gas. Absorption imaging spectroscopy was demonstrated to be able to identify regions of iodine gas in the post detonation environment and was correlated to schlieren imaging technique images. These systems were developed through a sequence of testing from system calibrations, iodine reference cell testing, gas plume investigations, and transitioned to $Al-I_2O_5$ thermite driven with an RP-2 detonator.

Helium-iodine gas plume testing demonstrated the ability for the optical systems to be correlated and calibrated to track iodine gas from first injection to fully developed gas plumes. A pure helium gas plume test series was performed which allowed the background spectral signal to be removed with a baseline shift. Once the background signal was identified and removed iodine gas was tracked within the test section. The time of iodine arrival was determined along with the relative concentration of iodine in the test chamber. Iodine gas plumes were perturbed with a simple shock wave to induce mixing. This testing showed a spatial shift of the helium-iodine gas plume and mixing that incorporated iodine gas which had fallen out of the main gas plume.

The testing transitioned to $Al-I_2O_5$ thermite being driven by an RP-2 detonator. The absorption imaging spectrometer and schlieren imaging technique images were processed into streak images. The absorption spectroscopy successfully tracked iodine in the detonation event. The schlieren imaging technique streak image was compared to the spectral image and it was determined that the $Al-I_2O_5$ thermite did not explosively detonate instead burns and creates a slower moving gas cloud. Unexpected results include refractive index spectral signal and the sensitivity of the absorption imaging spectrometer to iodine.

This testing allowed for characterization of the common path system parameters to incorporate a high speed camera absorption imaging spectroscopy

and schlieren imaging technique. The traditional exposure and temporal limits of imaging spectroscopy were expanded to resolve a high speed detonation event with a near continuous temporal resolution. A MATLAB code was developed to process images from the high speed camera to calculate the absorption spectra present within the schlieren imaging technique field of view. This code series was able to successfully correlate the schlieren imaging technique and spectroscopy data sets. This work is one of the first successful attempts at common path schlieren imaging technique and absorption imaging spectroscopy applied to a detonation event.

A large scale method for open air testing was explored and improvements to cost and flexibility were incorporated. Laser cut source grids allowed for a highly adaptable system. The laser cut grids had tolerances acceptable for source grids, smaller cut off grids did not have the tolerance needed. The mixed grid large scale system had a strong sensitivity such that heat from the human hand was seen. This type of focusing schlieren system has expanded capabilities over BOS or shadowgraph and should not become a forgotten optical method. The technique is ideal for medium scale fixed setups. Focusing with the current grid types is not a field portable system. Moving to a more rigid grid material such as a thin wood or plastic material could make focusing a semi portable field system. A plenoptic camera was tested with the system allowing a focusing sweep of the test section after testing. This plenoptic camera trial showed promise if the software was written to handle complicated optical setups. If advances are made in the plenoptic camera field focusing schlieren will become a very useful technique. Adding a spectroscopy component to the focusing system was not explored but a similar common path system is possible.

8.2 Future Research

8.2.1 Short Term

The MATLAB code has several known deficiencies such as non variable calibration. The code has been written through trial and error and several lessons were learned through the process. Spectroscopy calibration procedures need to incorporate non-uniform spatial calibration. The correlation process between schlieren imaging technique and imaging spectrometer needs to be adaptive and active to account for any camera movement during testing. The code set should be split into a master code and several sub codes. The first being a correlation process code. Then a code that processes the spectra data separately and saves the data sets. These two codes then should pass the data to a plotting and figure manipulation process. Correcting these deficiencies and adding automation of the code would be of great benefit.

Several improvements to THOR and sealing are needed. Adding gaskets or sealing compound to the windows would help improve flow conditions within the tunnel. In addition switching to glass windows may reduce residual iodine left on the windows during testing and allow for cleaning the windows.

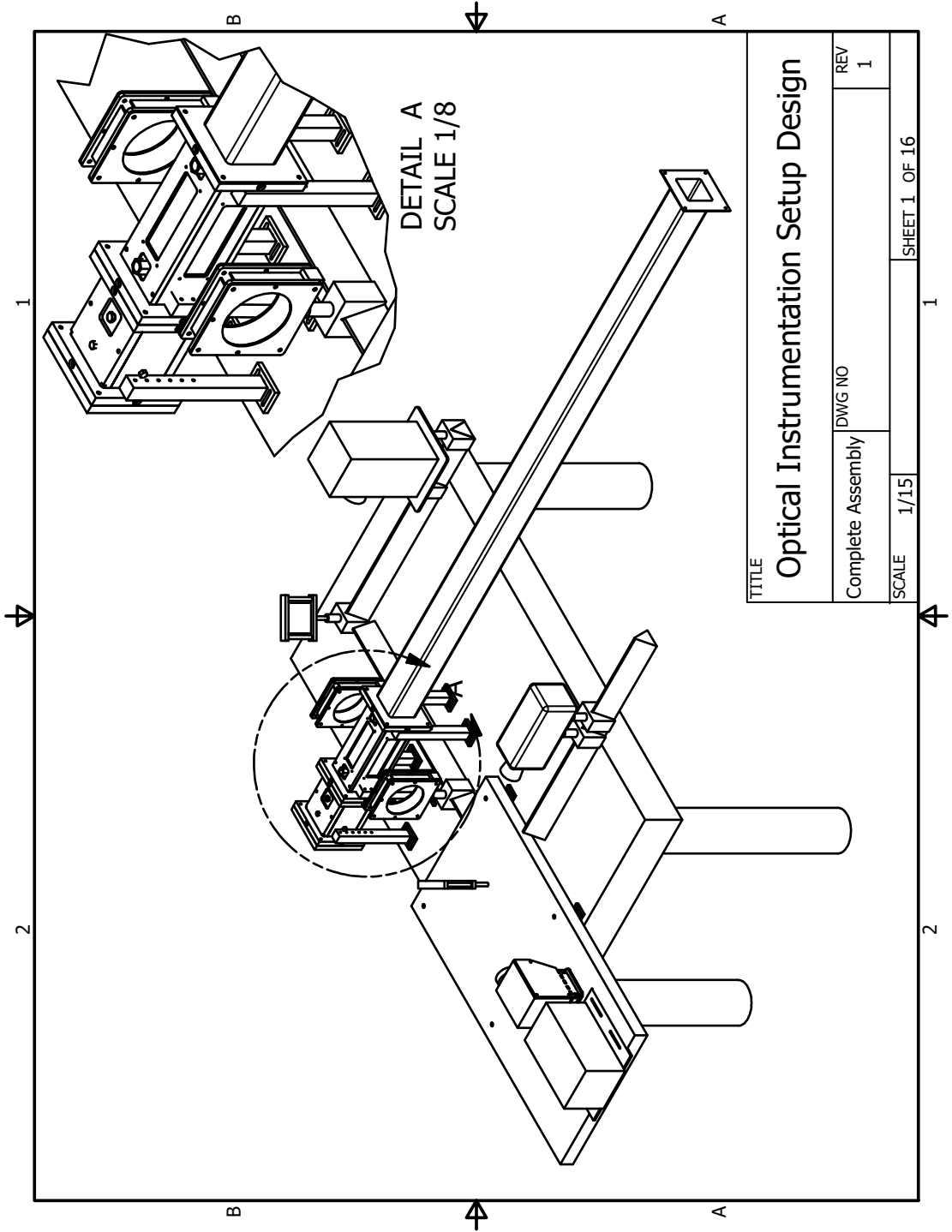
8.2.2 Long term

A more robust system to correct for refractive index shifts and background signal is needed. One possible solution is using the schlieren imaging technique images to calculate a background refractive index shift measurement. Applying this to the spectroscopy data sets would allow for direct corrections of the refractive shifts.

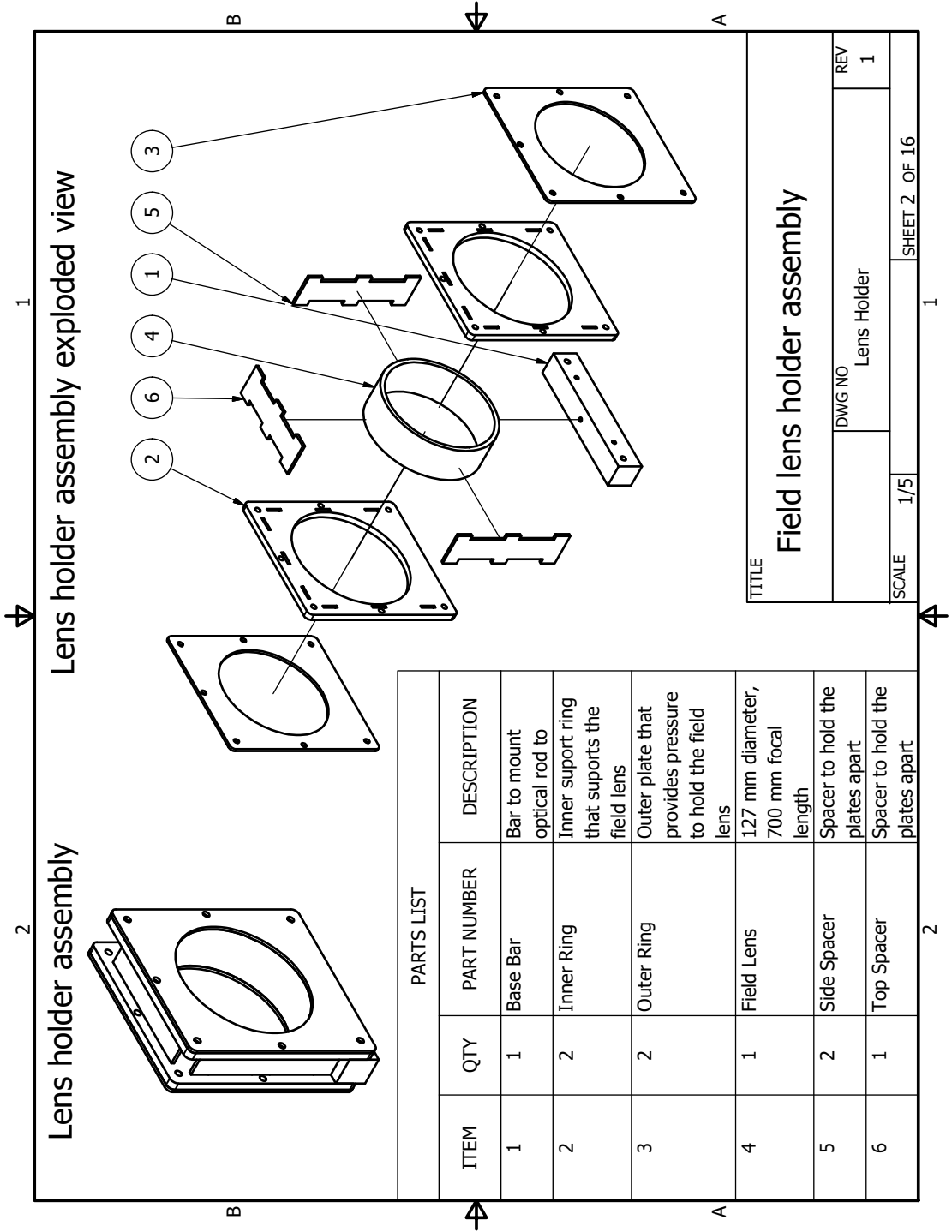
The same technique of a common path measurement of spectrum and schlieren imaging technique could be made using the focusing schlieren technique. This would give a method to move to large scale testing. The spectra would be a path measurement and would not be a direct correlation to the focusing schlieren data.

APPENDIX A

OPTICAL SYSTEM DRAWINGS



TITLE		Optical Instrumentation Setup Design	
Complete Assembly	DWG NO	REV	1
SCALE	1/15	SHEET 1 OF 16	

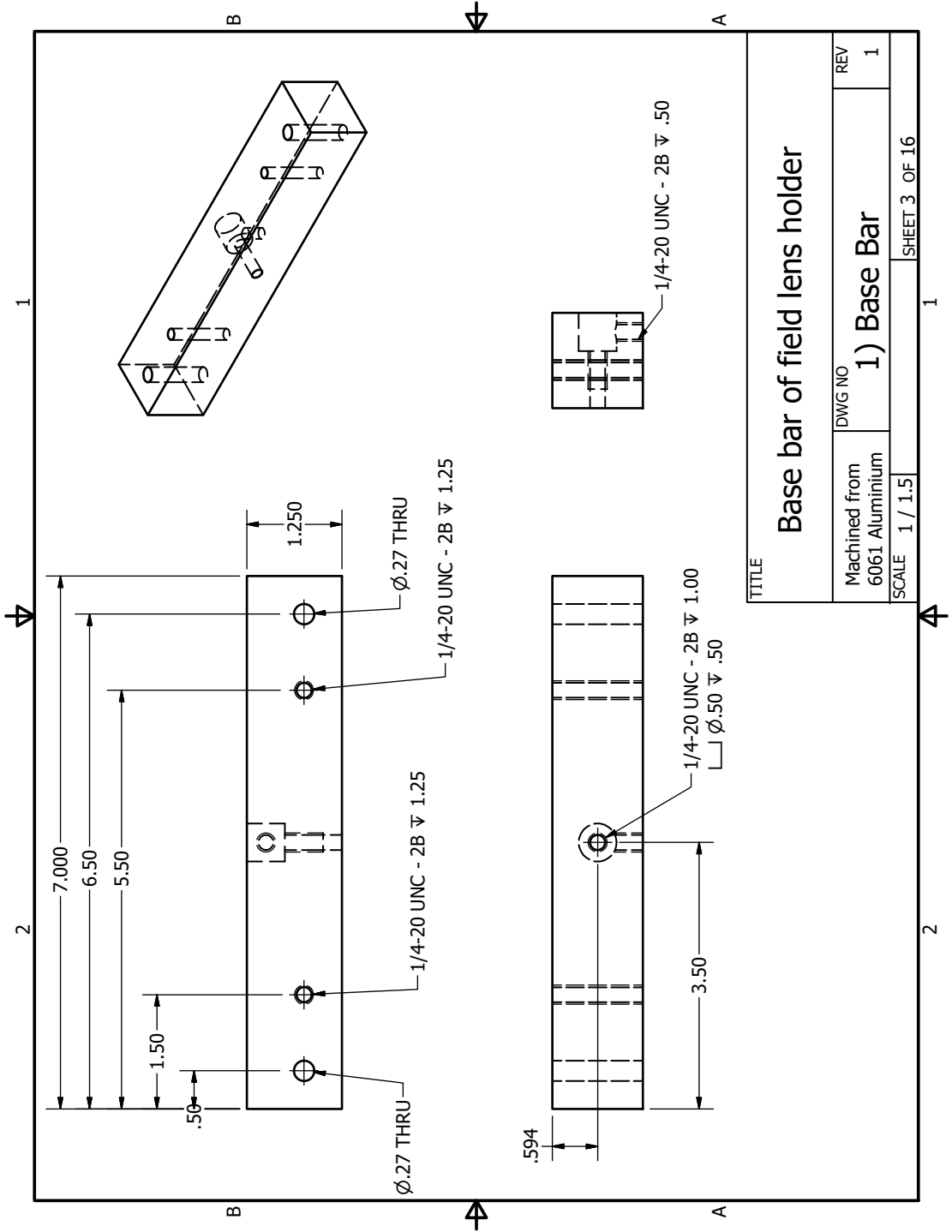


Lens holder assembly exploded view

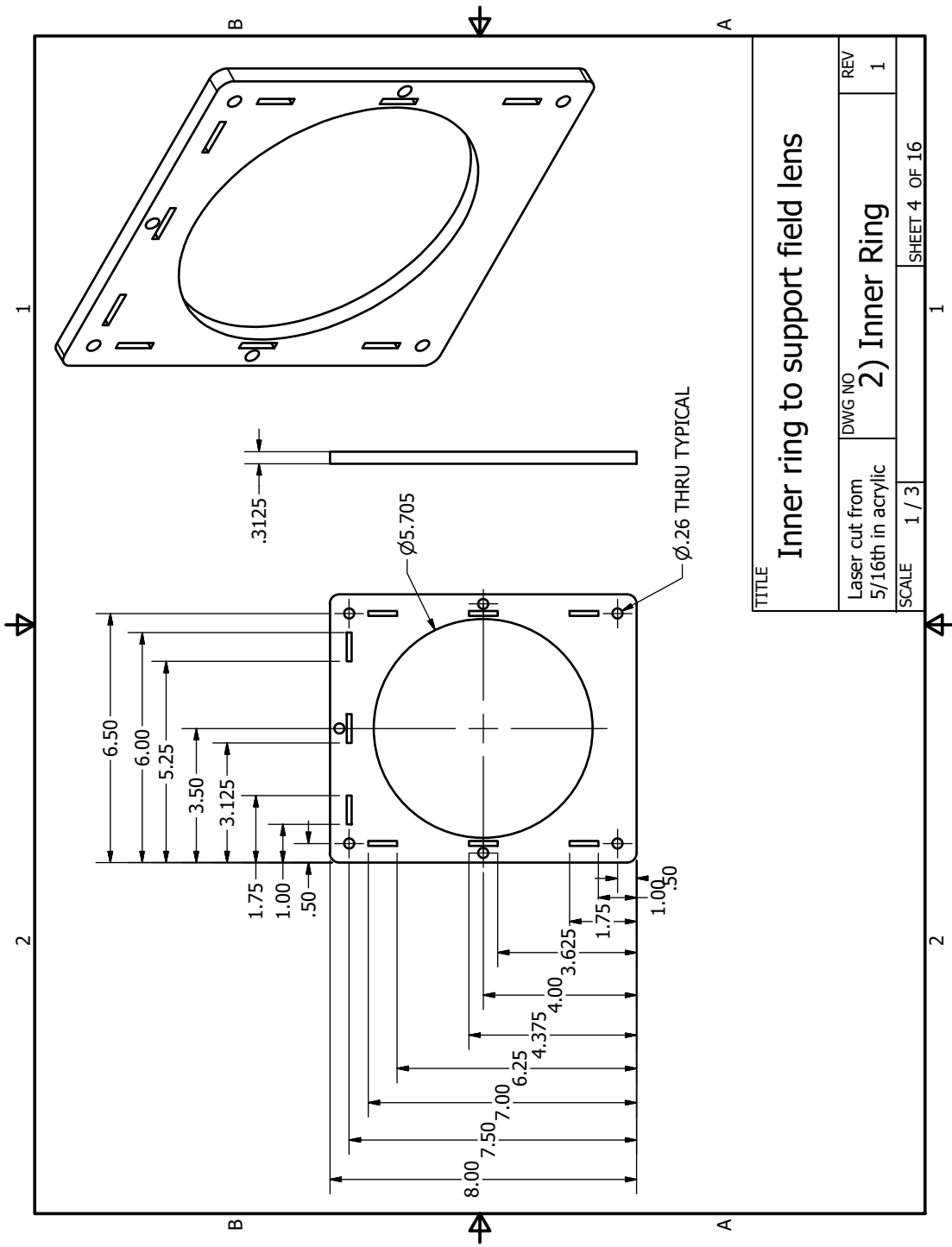
Lens holder assembly

PARTS LIST			
ITEM	QTY	PART NUMBER	DESCRIPTION
1	1	Base Bar	Bar to mount optical rod to
2	2	Inner Ring	Inner support ring that supports the field lens
3	2	Outer Ring	Outer plate that provides pressure to hold the field lens
4	1	Field Lens	127 mm diameter, 700 mm focal length
5	2	Side Spacer	Spacer to hold the plates apart
6	1	Top Spacer	Spacer to hold the plates apart

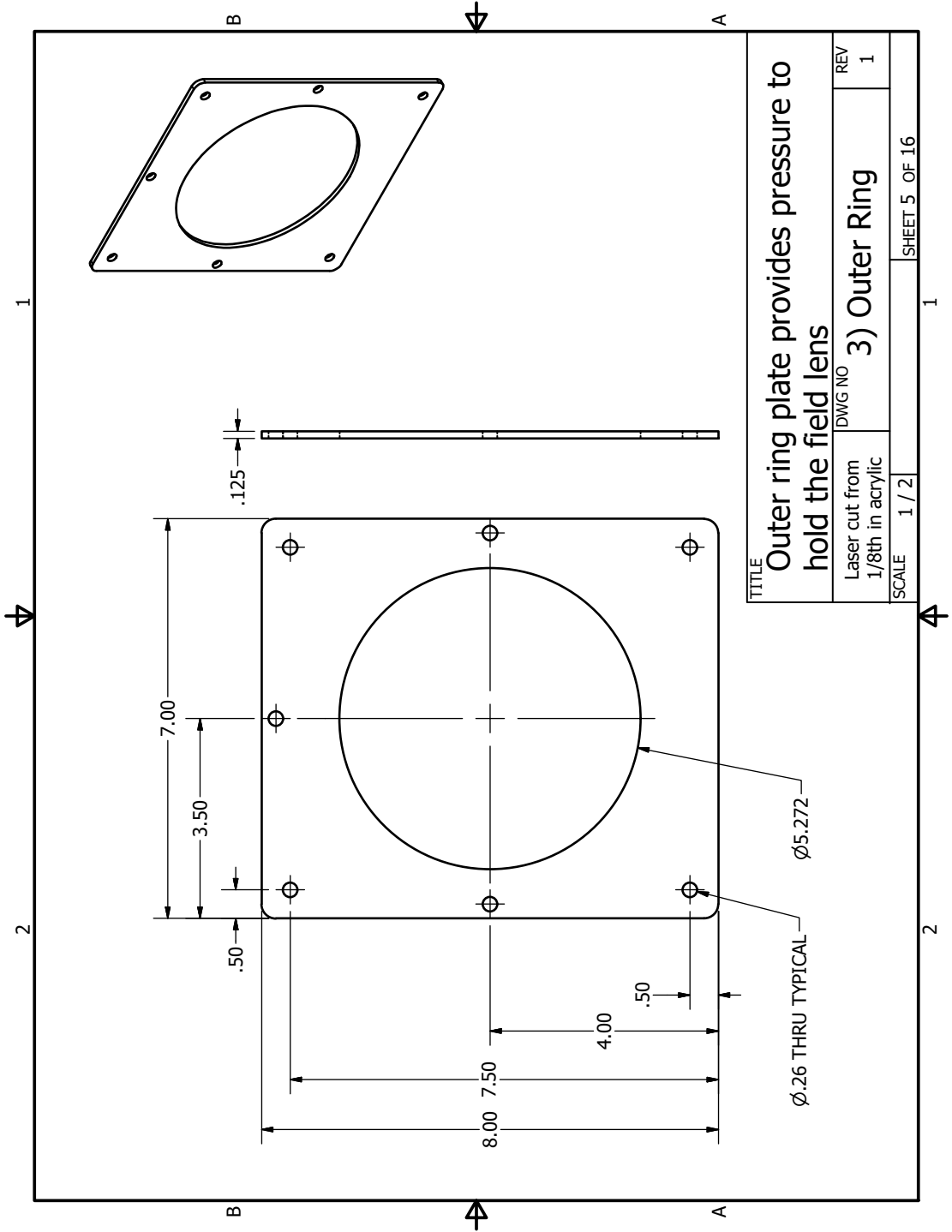
TITLE		Field lens holder assembly	
DWG NO	Lens Holder	REV	1
SCALE	1/5	SHEET 2 OF 16	

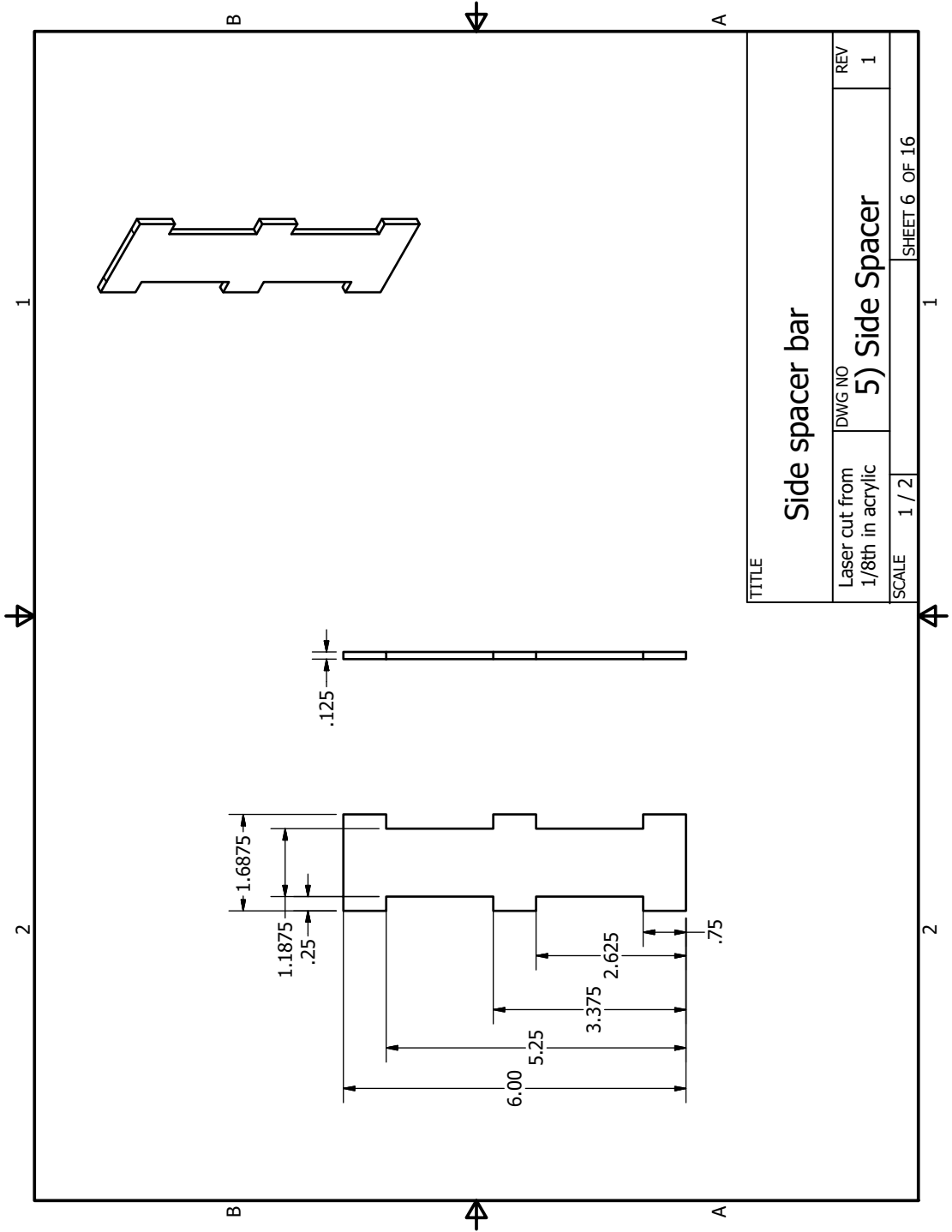


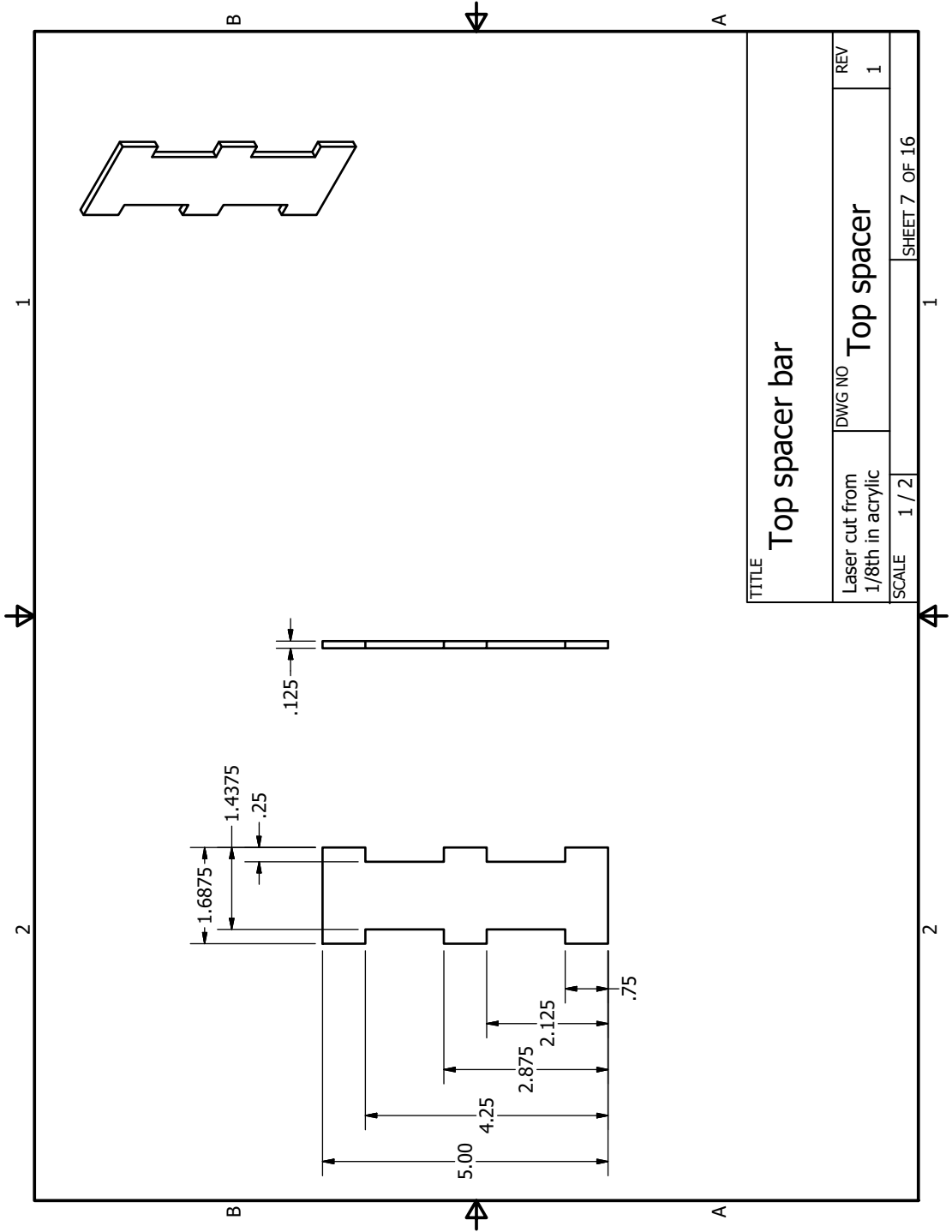
TITLE		Base bar of field lens holder	
Machined from	DWG NO	REV	1
6061 Aluminium	1) Base Bar		
SCALE 1 / 1.5		SHEET 3 OF 16	



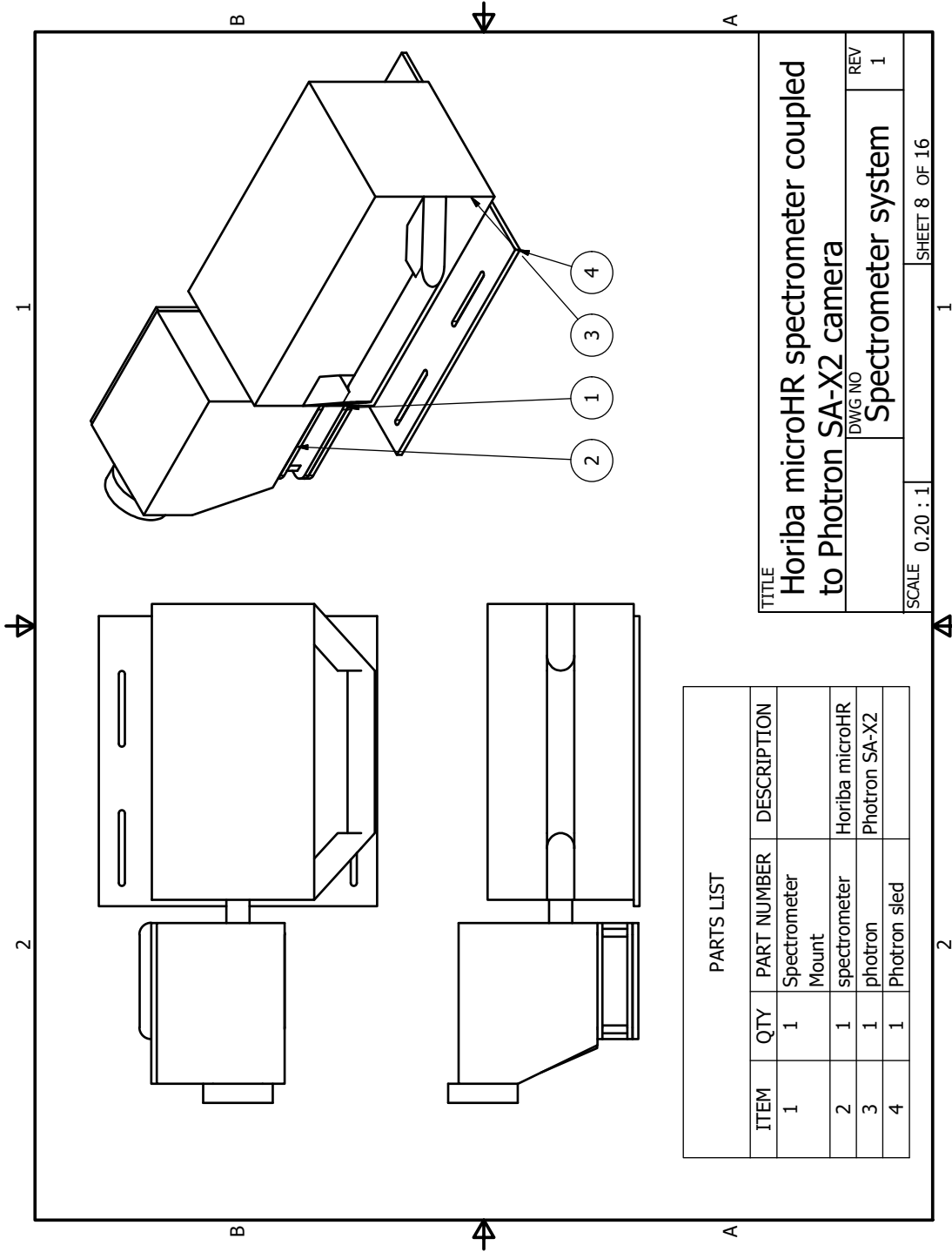
TITLE		Inner ring to support field lens	
Laser cut from 5/16th in acrylic	DWG NO 2) Inner Ring	REV 1	1
SCALE 1 / 3	SHEET 4 OF 16		





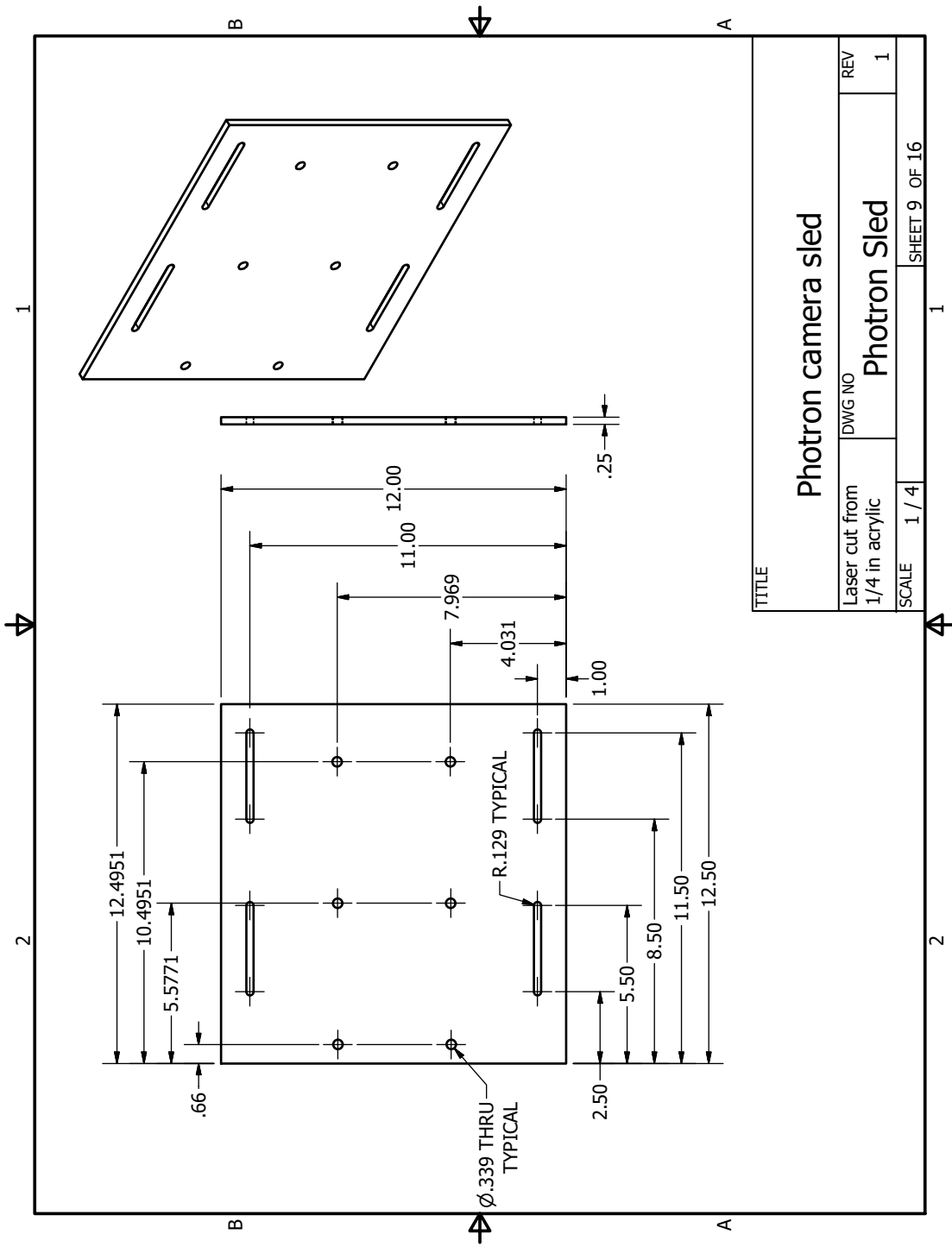


TITLE		Top spacer bar	
Laser cut from 1/8th in acrylic	DWG NO	Top spacer	
SCALE	1 / 2	SHEET 7 OF 16	
		REV 1	

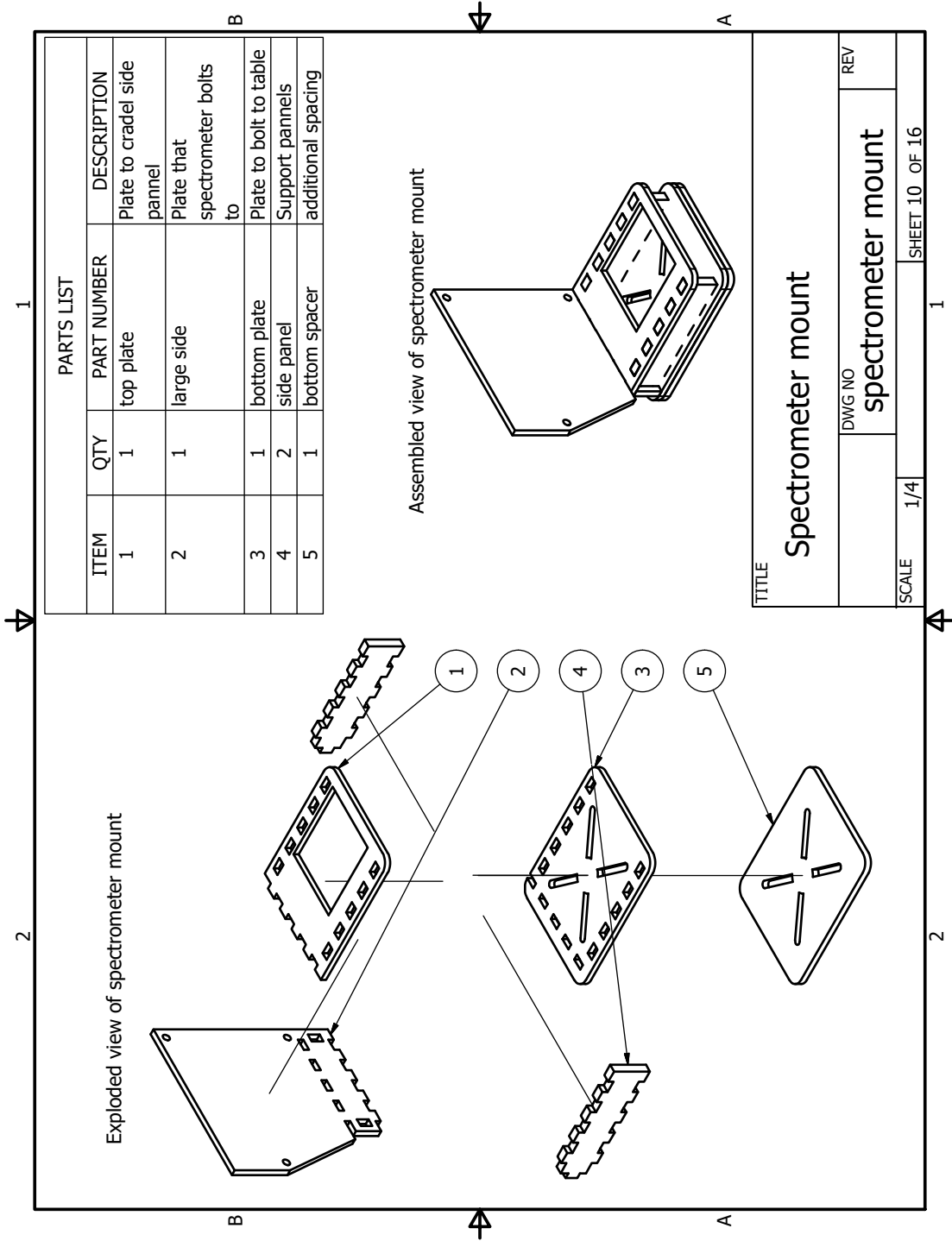


PARTS LIST			
ITEM	QTY	PART NUMBER	DESCRIPTION
1	1	Spectrometer Mount	
2	1	spectrometer	Horiba microHR
3	1	photron	Photron SA-X2
4	1	Photron sled	

TITLE		Horiba microHR spectrometer coupled to Photron SA-X2 camera	
DWG NO		Spectrometer system	
REV		1	
SCALE	0.20 : 1	SHEET 8	OF 16



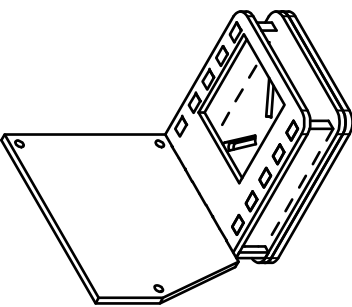
TITLE		Photron camera sled	
Laser cut from 1/4 in acrylic	DWG NO	REV	1
SCALE	1 / 4	SHEET 9 OF 16	



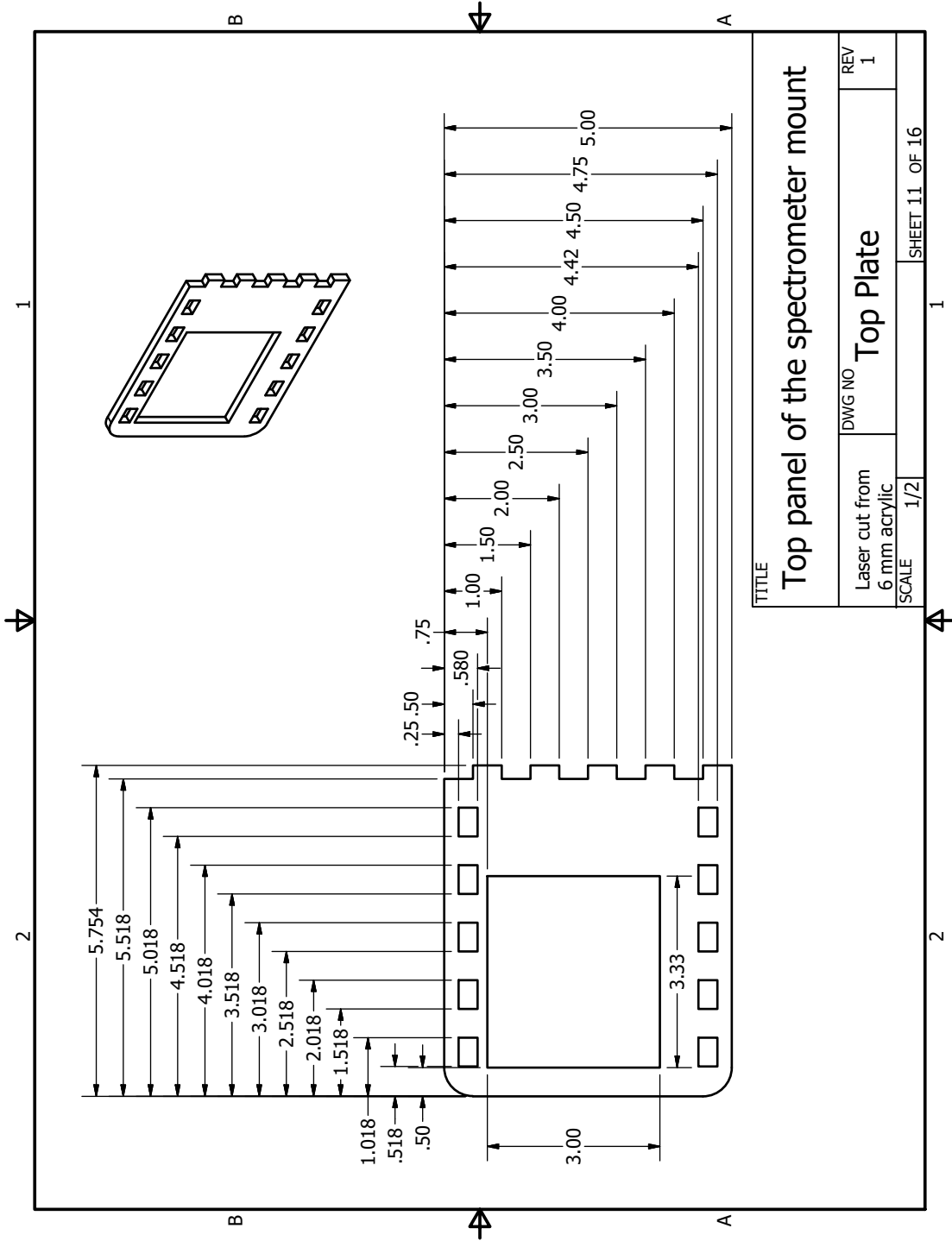
PARTS LIST

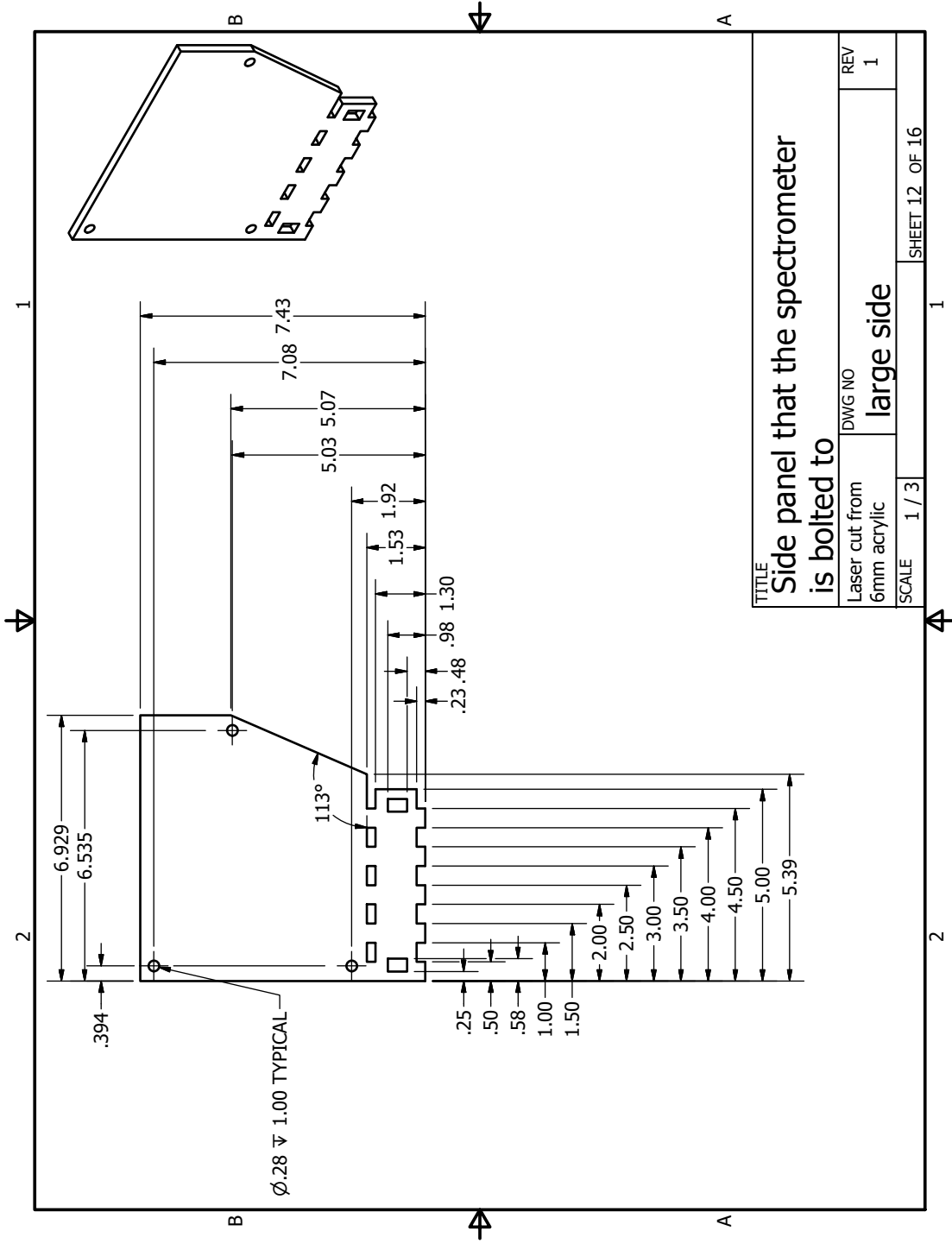
ITEM	QTY	PART NUMBER	DESCRIPTION
1	1	top plate	Plate to cradel side pannel
2	1	large side	Plate that spectrometer bolts to
3	1	bottom plate	Plate to bolt to table
4	2	side panel	Support pannels
5	1	bottom spacer	additional spacing

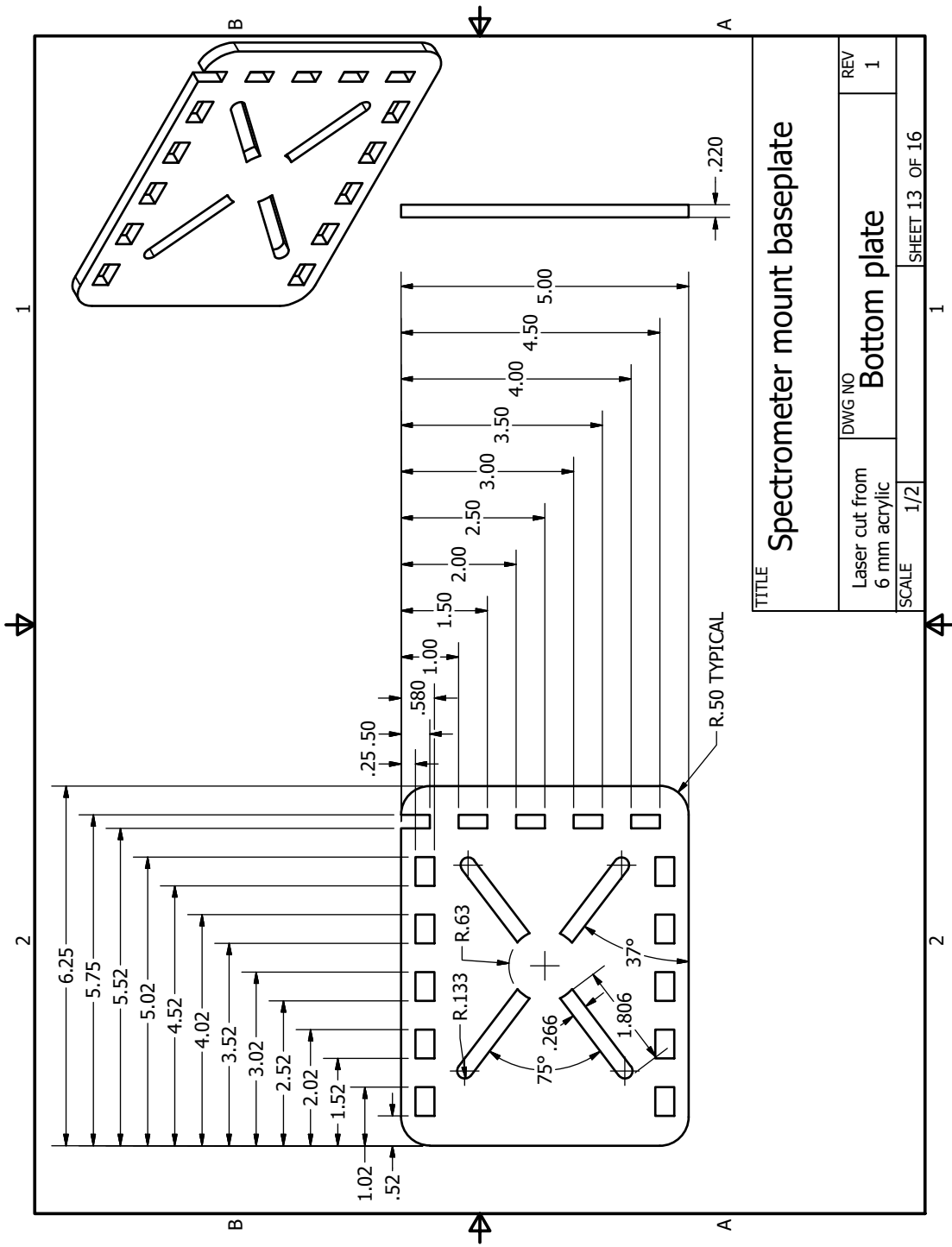
Assembled view of spectrometer mount

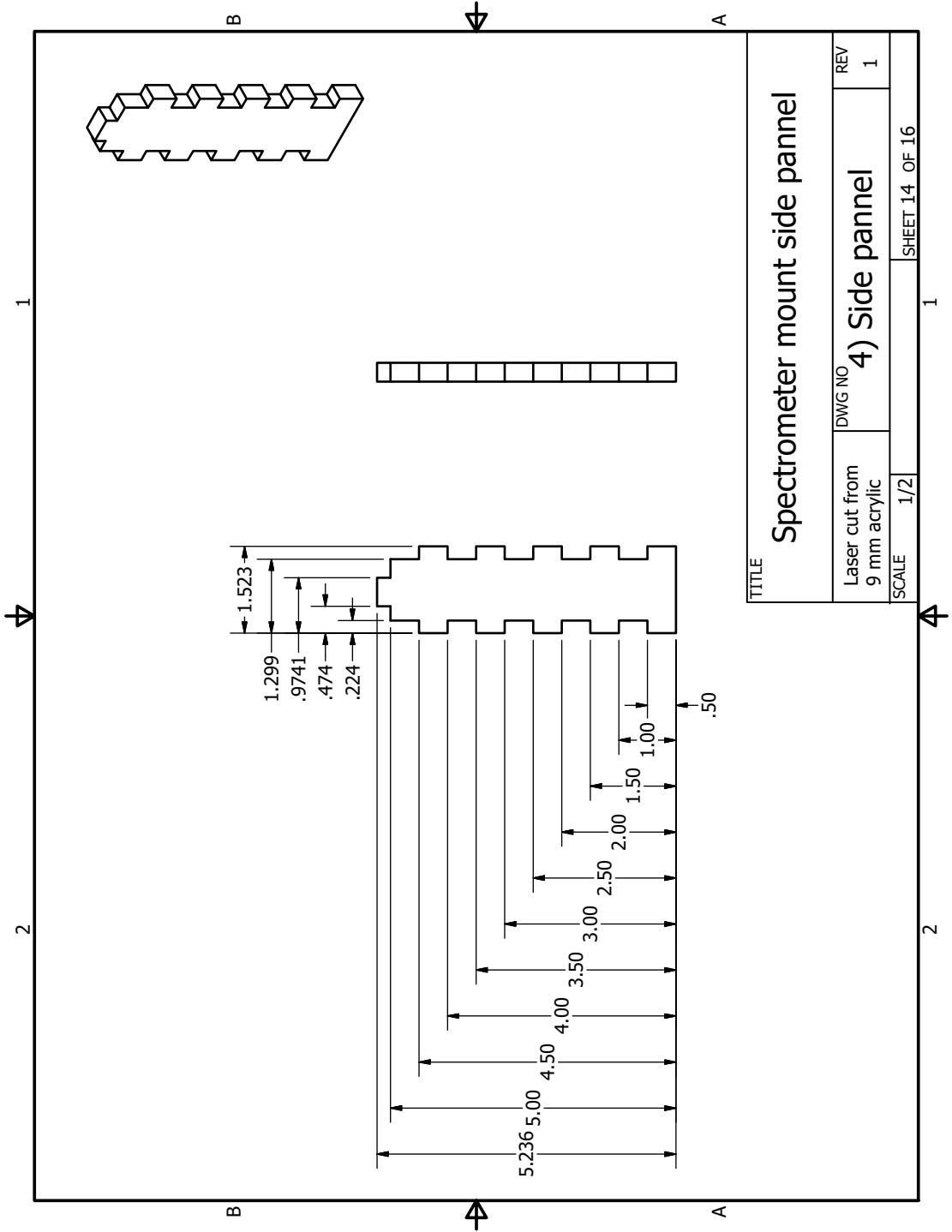


TITLE		Spectrometer mount	
DWG NO	REV	spectrometer mount	
SCALE	1/4	SHEET 10 OF 16	

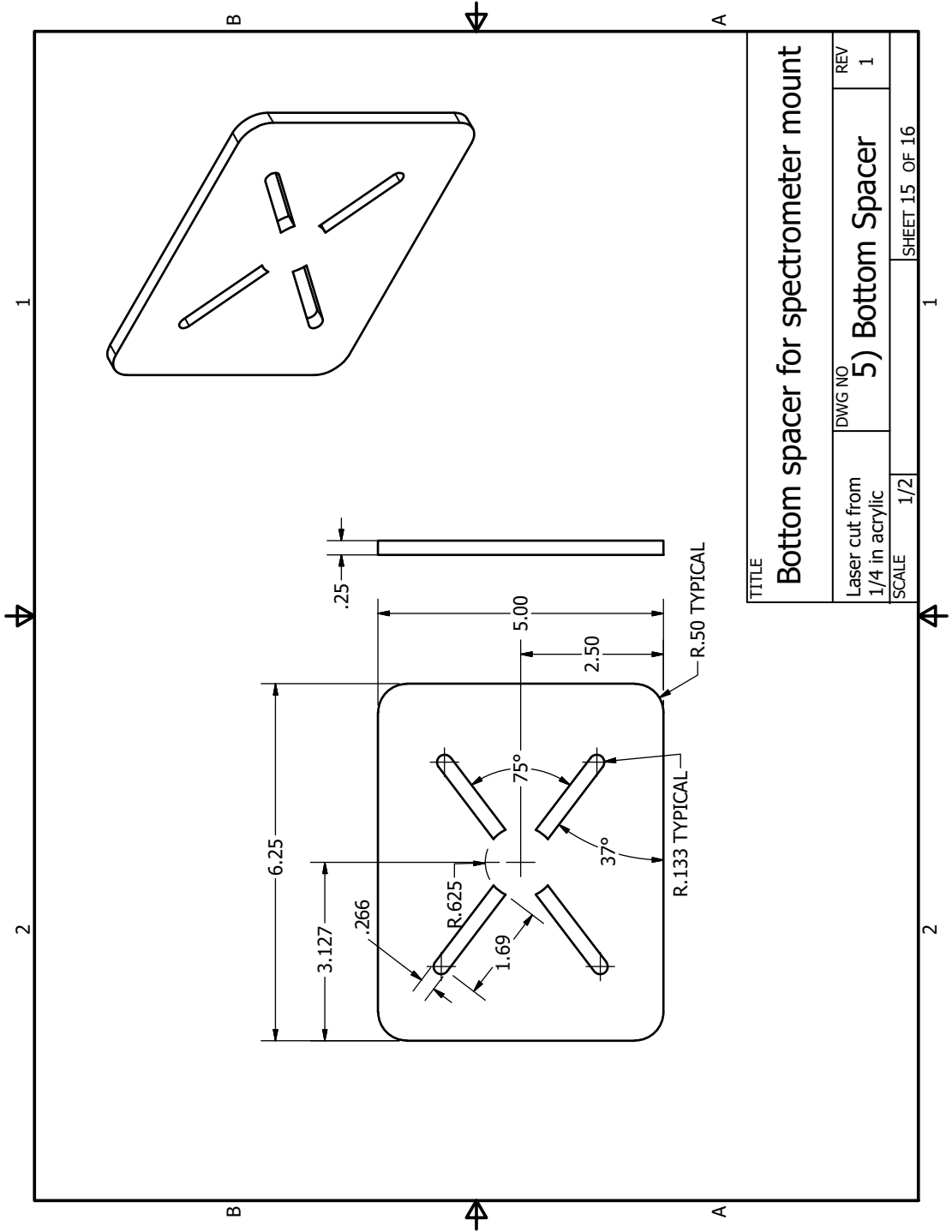




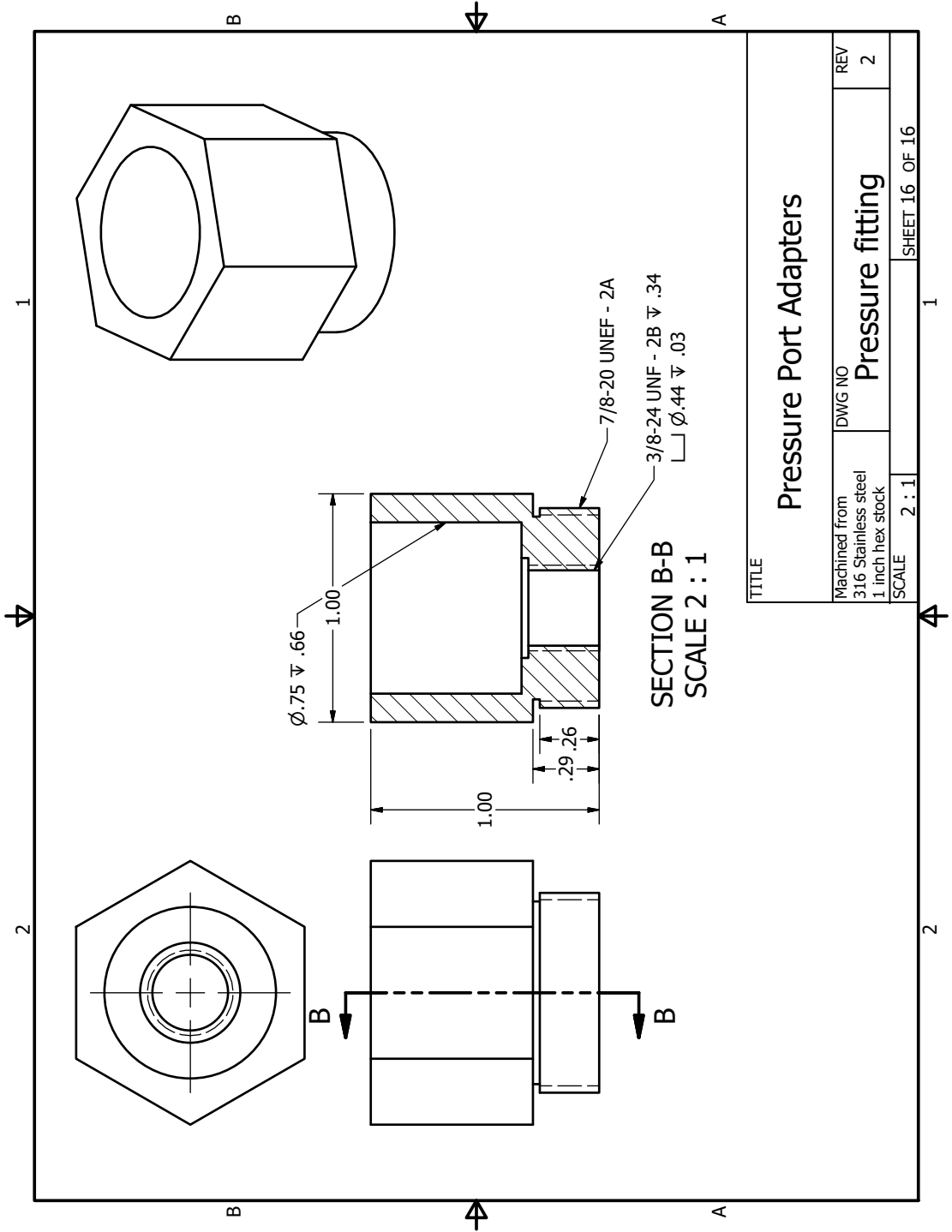




TITLE		Spectrometer mount side panel	
Laser cut from 9 mm acrylic	DWG NO	4) Side panel	REV 1
SCALE	1/2	SHEET 14 OF 16	



TITLE		Bottom spacer for spectrometer mount	
Laser cut from 1/4 in acrylic	DWG NO	5) Bottom Spacer	REV 1
SCALE	1/2	SHEET 15 OF 16	



TITLE		Pressure Port Adapters	
Machined from	DWG NO	REV	
316 Stainless steel		2	
1 inch hex stock	Pressure fitting		
SCALE	2 : 1	SHEET	16 OF 16

REFERENCES

- [1] Martin Brouillette. THE RICHTMYER-MESHKOV INSTABILITY. *Annual review of fluid mechanics*, 34:445–468, 2002.
- [2] Houas L and Chemouni I. Experimental investigation of Richtmyer-Meshkov instability in shock tube. *Physics of Fluids*, 8(2):614, 1996.
- [3] B. D. Collins and J. W. JACOBS. PLIF flow visualization and measurements of the RichtmyerMeshkov instability of an air/SF6 interface. *Journal of Fluid Mechanics*, 464(2002):113–136, 2002.
- [4] Richard L. Holmes, Guy Dimonte, Bruce Fryxell, Michael L. Gittings, John W. Grove, Marilyn Schneider, David H. Sharp, Alexander L. Velikovich, Robert P. Weaver, and Qiang Zhang. RichtmyerMeshkov instability growth: experiment, simulation and theory. *fluid mechanics*, 389(1999):55–79, 1999.
- [5] Oleg Schilling, Marco Latini, and Wai Sun Don. Physics of reshock and mixing in single-mode Richtmyer-Meshkov instability. *Physical Review E - Statistical, Nonlinear, and Soft Matter Physics*, 76(2):1–28, 2007.
- [6] Karnig O. Mikaelian. Richtmyer - Meshkov instability of arbitrary shapes. *Physics of Fluids*, 17(3):1–13, 2005.
- [7] Kaushik Balakrishnan, Franklin Genin, Doug V. Nance, and Suresh Menon. Numerical study of blast characteristics from detonation of homogeneous explosives. *Shock Waves*, 20(2):147–162, 2010.
- [8] G.S. Settles. *Schlieren and Shadowgraph Techniques*. Springer Berlin Heidelberg, 1st edition, 2001.
- [9] H. Kleine. Filming the invisible - time-resolved visualization of compressible flows. *European Physical Journal: Special Topics*, 182(1):3–34, 2010.
- [10] Michael J. Hargather and Gary S. Settles. Optical measurement and scaling of blasts from gram-range explosive charges. *Shock Waves*, 17(4):215–223, 2007.
- [11] Matthew M. Biss and Kevin L. McNesby. Optically measured explosive impulse. *Experiments in Fluids*, 55(6), 2014.
- [12] L Houas, E E Meshkov, and G Jourdan. Overview of diagnostic methods used in shock-tube investigations of mixing induced by Richtmyer-Meshkov instability. *Shock Waves*, 9(4):249–257, 1999.

- [13] Gary S. Settles and Michael Hargather. A review of recent developments in schlieren and shadowgraph techniques This. *Meas. Sci. Technol.*, 042001, 2017.
- [14] Henshall and BD. On some aspects of the use of shock tubes in aerodynamic research. Technical report, University of Bristol, 1955.
- [15] Michael W. Courtney and Amy C. Courtney. Note: A table-top blast driven shock tube. *Review of Scientific Instruments*, 81(12), 2010.
- [16] P. M. Giannuzzi, M. J. Hargather, and G. C. Doig. Explosive-driven shock wave and vortex ring interaction with a propane flame. *Shock Waves*, 26(6):851–857, 2016.
- [17] D. Estruch, N. J. Lawson, D. G. MacManus, K. P. Garry, and J. L. Stollery. Measurement of shock wave unsteadiness using a high-speed schlieren system and digital image processing. *Review of Scientific Instruments*, 79(12):10–13, 2008.
- [18] A F Goetz, G Vane, J E Solomon, and B N Rock. Imaging spectrometry for Earth remote sensing. *Science (New York, N.Y.)*, 228(4704):1147–1153, 1985.
- [19] J.M Lerner and A Thevenon. A TUTORIAL.
- [20] Barun Raychaudhuri. Imaging spectroscopy: Origin and future trends. *Applied Spectroscopy Reviews*, 51(1):23–35, 2016.
- [21] John R Ferraro, Kazuo Nakamoto, and Chris W Brown. *Introductory Raman Spectroscopy Second edition*. Elsevier, 2003.
- [22] Nick Glumac. Absorption spectroscopy measurements in optically dense explosive fireballs using a modeless broadband dye laser. *Applied Spectroscopy*, 63(9):1075–1080, 2009.
- [23] Jon D. Koch, Scott Piecuch, James M. Lightstone, Joel R. Carney, and Joe Hooper. Time-resolved measurements of near infrared emission spectra from explosions: Pure pentaerythritol tetranitrate and its mixtures containing silver and aluminum particles. *Journal of Applied Physics*, 108(3):3–6, 2010.
- [24] Joel Tellinghuisen. Transition strengths in the visibleinfrared absorption spectrum of I2 into three contributing transitions. *The Journal of Chemical Physics*, 58(7):2821–2834, 1973.
- [25] A Saiz-Lopez, R W Saunders, D M Joseph, S H Ashworth, and J M C Plane. Absolute absorption cross-section and photolysis rate of I 2. *Atmos. Chem. Phys. Atmospheric Chemistry and Physics*, 4:1443–1450, 2004.
- [26] M. J. Hargather. Background-oriented schlieren diagnostics for large-scale explosive testing. *Shock Waves*, 23(5):529–536, 2013.

- [27] Leonard M. Weinstein. Large-field high-brightness focusing schlieren system. *AIAA Journal*, 31(7), 1993.
- [28] Daniel Floryan, Jerrod Hofferth, and William Saric. Design , Assembly , and Calibration of a Focusing Schlieren System. Technical report, Cornell University, Ithaca, 2012.
- [29] Colin VanDercreek. *Hypersonic Application of Focused Schlieren and Deflectometry*. PhD thesis, University of Maryland, 2010.
- [30] Joshua Smith. *DESIGN AND CONSTRUCTION OF A FIXTURE TO EXAMINE THE PRODUCT FLOW OF Al / I 2 O 5 USING SCHLIEREN , SPECTROSCOPY , AND PRESSURE* by. PhD thesis, New Mexico Institute of Mining and Technology, 2016.
- [31] P Domens, J Dupuy, A Gibert, R Diaz, B Hutzler, J P Riu, and F Ruhling. Large air-gap discharge and Schlieren techniques. *Journal of Physics D: Applied Physics*, 21(11):1613–1623, 1988.
- [32] Matthew M. Biss and Gary S. Settles. On the use of composite charges to determine insensitive explosive material properties at the laboratory scale. *Propellants, Explosives, Pyrotechnics*, 35(5):452–460, 2010.
- [33] L. M. Weinstein. Review and update of lens and grid schlieren and motion camera schlieren. *European Physical Journal: Special Topics*, 182(1):65–95, 2010.
- [34] Ren Ng. Digital light field photography. *Stanford University*, pages 1–203, 2006.
- [35] Brian S Thurow and Kyle P Lynch. Development of a High-Speed Three-Dimensional Flow Visualization Technique. *AIAA Journal*, 47(12):2857–2865, 2009.
- [36] Timothy W Fahringer, Kyle P Lynch, and Brian S Thurow. Volumetric particle image velocimetry with a single plenoptic camera. *Measurement Science and Technology*, 26(11):115201, 2015.
- [37] Timothy W Fahringer and Brian S Thurow. Filtered refocusing: a volumetric reconstruction algorithm for plenoptic-PIV. *Measurement Science and Technology*, 27:94005, 2016.
- [38] Michael J Hargather and Gary S Settles. Retroreflective shadowgraph technique for large-scale flow visualization. *Applied optics*, 48(22):4449–4457, 2009.

STUDY OF TURBULENT MIXING IN A POST DETONATION
ENVIRONMENT USING SCHLIEREN AND IMAGING SPECTROSCOPY

by

JAMES SCOTT ANDERSON

Permission to make digital or hard copies of all or part of this work for personal or classroom use is granted without fee provided that copies are not made or distributed for profit or commercial advantage and that copies bear this notice and the full citation on the last page. To copy otherwise, to republish, to post on servers or to redistribute to lists, requires prior specific permission and may require a fee.

This thesis is accepted on behalf of the faculty of the Institute by the following committee:

Michael J. Hargather, Advisor

I release this document to the New Mexico Institute of Mining and Technology.

JAMES SCOTT ANDERSON

Date